Phase Diagram and Control of Thermoelectric Properties of Sodium Cobaltate

Thesis submitted in accordance with the requirements of

the University of London for the degree of Doctor of Philosophy by

Manoj Soundhira Pandiyan

Department of Physics

Royal Holloway, University of London

October 2013

Declaration of Authorship

I, **Manoj Soundhira Pandiyan**, hereby declare that this thesis and the work presented in it is entirely my own. Where I have consulted the work of others, this is always clearly stated.

Signed: _____

Date: _____

"எப்பொருள் எத்தன்மைத் தாயினும் அப்பொருள்

மெய்ப்பொருள் காண்பது அறிவு"

--திருவள்ளுவர், திருக்குறள், குறள்: 355;

"Whatever thing, of whatsoever kind it is,

this wisdom's part in each the very thing to see"

--Thiruvalluvar, Thirukkurral, Verse: 355.

"எண்ணிய முடிதல் வேண்டும்
நல்லவே எண்ணல் வேண்டும்;
திண்ணிய நெஞ்சம் வேண்டும்;
தெளிந்தநல் லறிவு வேண்டும்;
பண்ணிய பாவ மெல்லாம்
பரிதிமுன் பனியை போல,
நண்ணிய நின்முன் இங்கு
நசித்திடல் வேண்டும் அன்னாய்"

--மகாகவி சுப்ரமணிய பாரதியார்.

(அன்னையை வேண்டுதல்)

Dedicated to those who have dedicated so much without reclaim.

I owe you a debt of gratitude for what you have done!

Amma, Appa, Deepan and Prakash

Abstract

The temperature-composition phase diagram of sodium cobaltate, Na_xCoO_2, was determined over the range $0.32 < x < 0.85$ and $90 < T < 500K$. Sodium de-intercalation was achieved using Br_2/CH_3CN as an oxidising agent, and the superstructures were determined using X-ray diffraction.

A kaleidoscope of Na^+ ion patterns were found, including both commensurate and incommensurate structures. The sodium ion patterning of some of the superstructures was solved via a model independent approach using Reverse Monte Carlo.

Diffuse scattering was observed above the sodium ordering temperature. For high x, it was possible to reproduce the data using Monte Carlo simulations of short-range ordered arrangements of multi-vacancy clusters. For $x = 0.5$, the ordering consists of small regions of the superstructure confined to a single sodium plane.

Old samples of sodium cobaltate are found to have de-intercalated so that the surface layer has a superstructure corresponding to a lower value of x than the bulk.

The thermoelectric and magnetic properties change dramatically when the superstructures change from di-vacancies to tri-vacancies. In the case of $x = 0.5$ we are able to understand the resonant X-ray scattering from the electronic ordering directly from the superstructure.

Acknowledgements

I have thoroughly enjoyed my PhD years in a great science journey, travelled to a lot of wonderful places, met colourful faces, enjoyed very different weather to my home and strongly believe in the phrase: ***We are Winners!***

First, I would like to express my sincere gratitude to my supervisor, a friend and fantastic tennis player, **Jon Goff**, for his guidance, support and inexhaustible patience. **Jon** enabled me to survive in this doctoral research with his endless persistence, and moreover I thank him for being gifted with a firm enthusiasm and factual charm.

This work could not be done without the samples of sodium cobaltate. These single crystals were grown by **S. Uthayakumar** at Royal Holloway, and also it was great to achieve neutron sized $LiCoO_2$ single crystal for the first time with his incredible effort and endurance. I always saw him as a good support in my research. My thanks to **Michel Roger**, CEA Saclay, France, for his help in solving structures and advice in my research.

In my four years of doctoral research, I'm lucky to have pretty much time to use neutrons and synchrotron X-rays facility in Rutherford Appleton laboratory. My sincere thanks to **Matthias Guttmann**, ISIS facility, for his tireless help, where I performed an enormous amount of neutron diffraction experiments on SXD. My special thanks to the I16 team of **Steve Collins**, **Gareth Nisbet** and **Carlo Vecchini** for their excellent ideas and timely help during our research in delicate diffractometer in the I16 beamline at the Diamond light Source. My gratitude to a cool personality **Raymond Fan** for his energetic ideas that kept our eyes opens during tough times at the I10 beamline and help to access the SQUID/VSM.

Acknowledgements

Yes, it was **Dan Porter**, with where I spent most of my research time in learning new stuff, using his Matlab codes, sharing ideas for my thesis, and also attended his wedding which I never forget in my life. Without continuous help of **Dan**, this thesis would have not end up with beautiful pictures and graphical curves. My thanks to **Ian Murray,** for his help and easy access to chemicals and other laboratory stuffs at Royal Holloway.

I would like to thank those within the condensed matter group and a special thanks to the PhD students in my group: **David Voneshen, Toby Willis, Eron Cemal, David Bowman and Giovanni Pasquino** for their support in my research. My special thanks to **Terence Giles** and **James Poulten** for their help to get stunning results in PPMS at Royal Holloway. I specially thank **David Pavitt** for sharing good times with me in Munro fox annexe office, and all other colleagues who took part in 3 p.m. tea and shared my short breads at common room.

I am forever grateful to my tutor and mentor, **Dr. Amuda Rajamani**, for her continuous inspiration and encouragement, without her I would never have embarked on a research degree in Physics at all.

Many thanks to m**y friends** who played a vital role virtually in this making that I cannot confine all of them in this small part.

Most specially my heartfelt thanks to **Mom, Dad, Deepan and Prakash** who has been tremendously supportive and always been there for me.

You are really great! Thank you so much!!

Contents

Contents

Contents

List of Figures:

List of Figures

List of Figures

List of Figures

List of Figures

List of Figures

List of Tables:

Chapter 1

Background

Global targets to reduce carbon emissions make the reduction of energy consumption one of the most important challenges for science and technology. The new materials under consideration in this thesis have the potential to transmit power with zero losses, store energy, and to convert waste heat into useful electrical power.

In 1997, Terasaki *et al.* discovered the coexistence of a large in-plane thermoelectric power (~100 μV/K) and low resistivity (200 μΩ) at room temperature in Na_xCoO_2, and this value is slightly greater than that of bismuth telluride (Bi_2Te_3) which is usually considered as a reference material for this temperature range [1].

The next breakthrough came in 2003 when Takada *et al.* discovered the superconductivity in Na_xCoO_2 from the two dimensional layers of CoO_2 layers separated by the intercalation layers of the sodium and water molecules. The compound becomes a superconductor at (T_c ~ 5 K) near x = 0.35 with H_2O y = 1.3, a phase diagram between sodium levels and the critical temperature T_c could then be drawn up, showing a phase of superconductivity [2]. Hydrating the compound substantially increases the

spacing between CoO_2 layers and the c-axis length that increased an interest in an investigation of the physical properties of a new layered material to compare with the cuprate superconductors. Doping Na_xCoO_2 with divalent calcium or strontium ions leads to improvements in the power factors [3-6].

The misfit cobaltites, $Ca_3Co_4O_9$, show an excellent chemical stability at 1000K, and they are potentially useful for waste heat recovery at high temperatures. The complexity of the misfit structures comes from aperiodic character of the two monoclinic sublattices where most of the misfit compounds crystallize in the monoclinic C2/m space group. Both the rock salt (RS) and CdI_2-type lattices have a monoclinic symmetry with identical ***a*** and ***c*** but different ***b*** parameters [7].

The family of "114" cobaltites – $LnBaCo_4O_7$ and $CaBaCo_4O_7$ are referred to as Kagome "114" Cobaltites. This layered cobalt oxide family has a triangular geometry of their oxygen framework. They have been extensively investigated for the last few decades, due to their ability to exhibit magnetic frustration. This type of material has been investigated for the magnetic, electronic and thermoelectric properties, and potentially used in the mid-temperature range (500-600K) for power generation [8].

Sodium cobaltate is from the same family of layered intercalation compounds as the lithium-ion battery materials. The abundance of sodium over lithium makes it an attractive alternative for rechargeable portable batteries [9]. This ability to change the sodium composition chemically or electrochemically makes it an attractive compound in order to control the physical properties.

In this thesis, I shall focus on how to improve thermoelectric properties with the sodium concentration. Hence the dramatic improvements on the oxide

materials with high thermopower are considered to be promising for future thermoelectric applications and candidates for devices, which can directly convert heat into electrical energy using the phenomenon called the Seebeck effect. In such a way the layered cobaltates serve as an ideal thermoelectric material class in order to study and improve an in-depth fundamental understanding of this complex material for the conversion of waste heat into electricity.

1.1 Crystal structure of Na_xCoO_2

As for the cuprates, sodium cobaltate is a layered transition metal oxide, but the structure shows an alternating CoO_2 layers between sodium planes instead of CuO_2 layers. For Na_xCoO_2 the trigonal planes of Co consist of octahedra sharing the in-plane direction of the CoO_6 octahedron in the CoO_2 layers, instead of a square lattice in CuO_2 layers. The crystal structure of Na_xCoO_2 is shown in figure 1.1 [3].

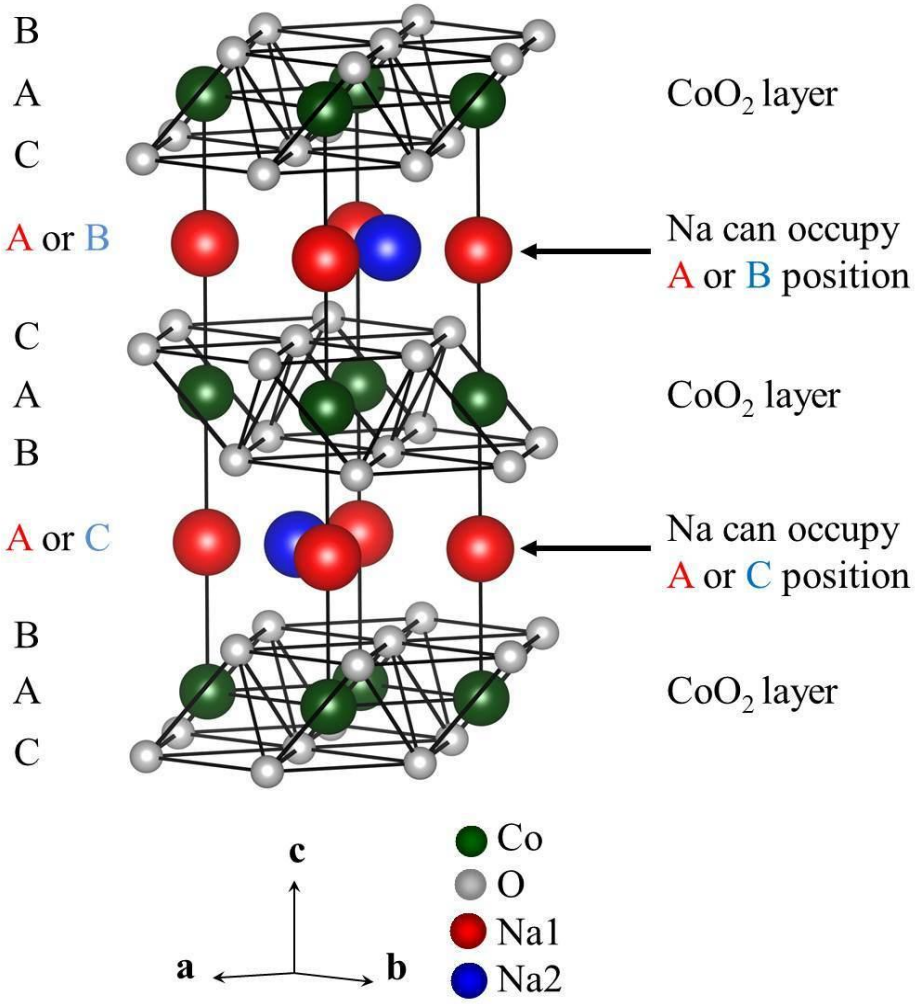

Figure 1.1: Crystal structure of Na_xCoO_2. Ref. :[3].

The unit cell consists of double layer γ- Na_xCoO_2 has a hexagonal structure having a space group symmetry $P6_3/mmc$ (No. 194 in the International Tables of Crystallography*)*. The alternating sheets of cobalt are covered above and below by the layers of oxygen. These cobalt-oxygen atoms are separated by 3.4Å, which allows the layers of sodium having atomic radius 1.9Å to be accommodated between successive layers, and the concentration of sodium can vary between 0 and 1.

The sodium ions are relatively free to move within the planes using thermal vibrations, and quantum mechanical tunnelling since the ions are larger than the space available to them between equilibrium sites [10]. The arrangement of the triangular lattice of cobalt atoms may lead to eventual magnetic frustration that leads to unconventional properties. The oxygen octahedral cage also undergoes trigonal distortion in the *c*-direction, which tends to bring O to Co deformation, which is more pronounced in the low sodium content. This trigonal distortion is due to the Jahn-Teller effect, where the geometrical distortions in the cobalt-oxygen bond lengths were arrange themselves into ordered patterns. The lattice parameter in the plane (distance between two Co nearest neighbours), $a \approx 2.8$ Å is relatively constant. However, the distance between planes varies with $c \approx 10.8{-}11.0$ Å on average, decreasing with Na concentration. The positional co-ordinates for Na_xCoO_2 are given in table 1.1. For high doping, the increase of a large number of Na ions between CoO_2 planes can enhance the electrostatic repulsion between adjacent oxygen layers, thereby reducing the spacing between the planes.

The sodium ions sit between oxygen ions on the same hexagonal sites. For example, in Figure 1.1 the oxygen sitting either side of the top sodium layer are on C sites, so that sodium can sit on either A or B sites. The A (Na1)

sites are immediately above the cobalt site, whereas the B (Na2) sites are at the centre of the triangle of cobalt sites. The short-range repulsion for the Na1 sites is larger and, as a consequence, it is energetically more favourable for the sodium ions to occupy Na2 sites. Hence, the stacking sequence for the sodium cobaltate structure is ABCBACBC, see figure 1.1.

As the concentration of vacancies on the Na2 lattice site increases it becomes energetically favourable to form multi-vacancy clusters, and this leads to the promotion of Na2 to Na1 sites. The concentration of vacancies can readily be controlled through chemical intercalation methods, and this leads to a kaleidoscope of superstructures. These superstructures can then, in principle, be used to control the thermoelectric properties.

Table 1.1: The positional co-ordinates of Na_xCoO_2, given by fractional values along a-, b- and c- directions.

Atom	***x***	***y***	***z***	***Site***
Co	0	0	0	2a
O	1/3	2/3	0.0908	4f
Na1	0	0	1/4	2b
Na2	2/3	1/3	1/4	2d

1.2 Thermoelectricity

Seebeck observed that if two dissimilar materials were joined together and the junctions were held at different temperatures (T and T+ΔT) a voltage

difference (ΔV) was developed that was proportional to the temperature difference (ΔT). The ratio of the voltage developed to the temperature gradient is related to an intrinsic property of the materials (see figure 1.2), which directly converts the temperature differences into electricity and is called the Seebeck coefficient (S) or the thermopower.

$$S = -\frac{\Delta V}{\Delta T} \tag{1.1}$$

Conversely, if an electrical current is passed through a thermoelectric material, heat is either absorbed or rejected (cooling occurs) at one end depending on the direction of the current. This effect is known as the Peltier effect (see figure 1.2). These two effects are entirely related to each other and the Peltier coefficient (π) is given by,

$$\pi = ST \tag{1.2}$$

To get a good performance with a thermoelectric power, 'S' must be high in order to obtain the maximum voltage for a given temperature difference. Similarly, the electrical conductivity 'σ' must be high to minimize the electrical energy dissipated by the Joule effect, which is the case for all types of electricity generator.

It is easier to maintain a large difference in temperature for materials with low thermal conductivity 'κ'. These considerations justify a simple expression of the figure-of-merit ZT for thermoelectric performance

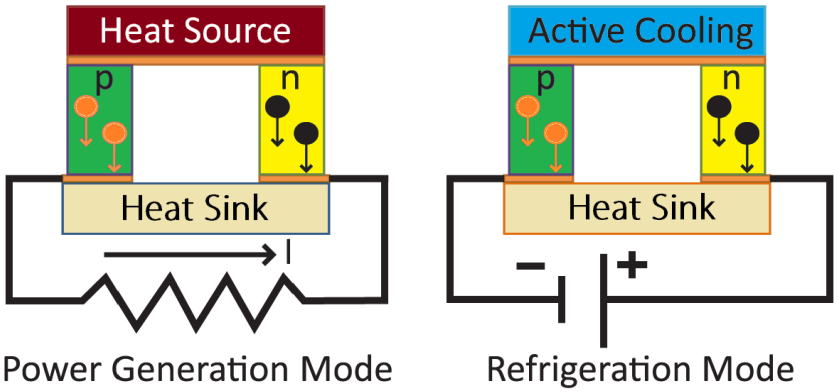

Figure 1.2: Thermoelectric device model in power generation mode (Seebeck effect) and refrigeration mode (Peltier effect)

$$ZT = \frac{S^2\sigma}{\kappa}T \tag{1.3}$$

where, $S^2\sigma$ is also called the Power factor, which has higher values in a narrow gap semiconductors rather than metallic compounds.

The figure-of-merit for a thermoelectric module composed of *p*-type and *n*-type material can be evaluated using,

$$ZT = T \times \frac{\left(S_p - S_n\right)^2}{\left[\left(\sqrt{\frac{\kappa_n}{\sigma_n}} + \sqrt{\frac{\kappa_p}{\sigma_p}}\right)\right]^2} \tag{1.4}$$

The efficiency (η) in power generation and the coefficient of performance (φ) in refrigeration are directly related to the material's figure-of-merit (ZT) [11]. The efficiency in power generation (η) is given by the ratio of the electrical output (W) over the external thermal power applied (Q_H), and the coefficient of performance (φ) is given by the ratio of maximum cooling power or the net pumping rate (Q_C) over the external power supplied (W)[11-13].

For the power generation mode, the maximum efficiency is evaluated by,

$$\eta_c = \frac{W}{Q_H} = \frac{T_H - T_C}{T} \times \frac{\sqrt{1+ZT}-1}{\sqrt{1+ZT}+\frac{T_C}{T_H}} \tag{1.5}$$

For the refrigeration mode, the coefficient of performance is given by,

$$\varphi = \frac{Q_C}{W} = \left(\frac{T}{T_H - T_C} \times \frac{\sqrt{1+ZT}-1}{\sqrt{1+ZT}+1}\right) - \frac{1}{2} \tag{1.6}$$

where, T_C and T_H are the cold and hot junctions with the mean value Tm. $\Delta T = T_H - T_C$, is the maximum temperature difference that can be achieved during the power generation mode in the thermoelectric module.

$T = \frac{T_H + T_C}{2}$ for both the equations. The efficiency consists of two parts; the first one would be the Carnot efficiency ($\frac{T_H + T_C}{T_H}$) and the second one would be the loss term ($\frac{\sqrt{1+ZT}-1}{\sqrt{1+ZT}+\frac{T_C}{T_H}}$). The high figure-of-merit values result in higher efficiency and when ZT reaches infinity, the efficiency reaches the Carnot efficiency [11].

The electrical conductivity increases with increase in carrier concentration, while the Seebeck coefficient decreases, with the electrical power factor maximizing at a carrier concentration of around 10^{25} cm^{-1}. The electronic contribution to the thermal conductivity λ_e, which in thermoelectric materials is generally around 1/3 of the total thermal conductivity, also increases with carrier concentration. Evidently the figure-of-merit optimizes at carrier concentrations which corresponds to semiconductor materials. Consequently, semiconductors are the materials most researched for thermoelectric applications giving higher Seebeck values than metals [12].

The best thermoelectric materials that are currently in devices have a value of ZT≈1. Semiconductors have essentially reached the limit of their development for a materials perspective. Hence, this value, ZT≈1, has been a practical upper limit since the 1970's. However, no theoretical or thermodynamic reason exists for ZT≈1 as an upper barrier [14].

Alloy based materials such as Bi_2Te_3 $[(Bi_{1-x}Sb_x)_2$ $(Te_{1-x}Se_x)_3]$, $Si_{1-x}Ge_x$ are limited to operation near room temperatures to avoid sublimation, oxidation or decomposition. These materials are specifically used in the room temperature applications of refrigeration and waste heat recovery. Peak ZT values of these materials are in the range of 0.8 to 1.1 [15].

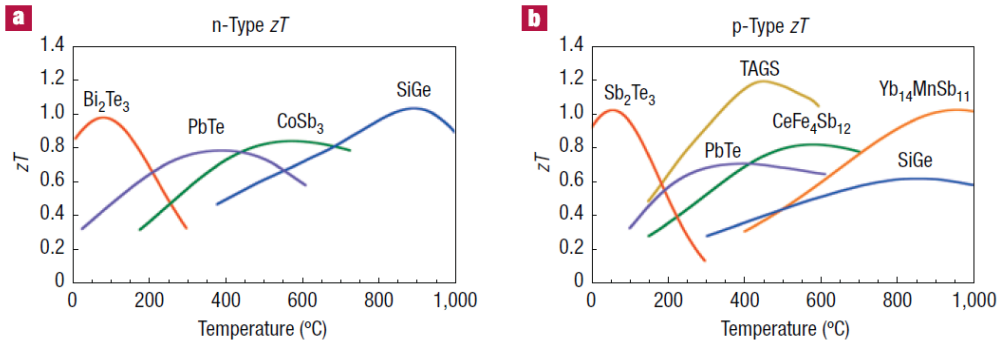

Figure 1.3: Figure-of-merit ZT as a function of temperature of the state-of-the-art thermoelectric materials used for refrigeration and power generation. (a) n-type and (b) p-type thermoelectric materials of complex alloys with dopants [15].

The materials based on group-IV tellurides such as PbTe, GeTe or SnTe are used in the mid-temperature (500-900K) for power generation and their ZT is typically about 0.8 (see Fig 1.3). Alloys such as $AgSbTe_2$ are seen to be a material with high ZT greater than 1 (see Fig 1.3). The p-type alloy $(GeTe)_{0.85}(AgSbTe_2)_{0.15}$, which is generally referred to as TAGS has been successfully used in long-life thermoelectric generators, with a maximum ZT greater than 1.2 [12, 15].

The Zintl phase, $Yb_{14}MnSb_{11}$ has recently emerged as a promising and ideal intermetallic thermoelectric material for very high temperatures. This type of compound belongs to the Zintl family, $A_{14}MPn_{11}$, where A is an alkaline-earth (or) rare-earth metal, M is a transition (or) main-group metal, and Pn is a pnicogen. This material has been extensively studied for their magnetic properties and also it exhibits weakly metallic or semi-metallic behaviour as a function of temperature [15-16].

Skutterudites, $CoSb_3$ with multiple co-fillers ($La_{0.9}Fe_3CoSb_{12}$, $Ce_{0.9}Fe_3CoSb_{12}$, $Yb_xCo_4Sb_{12}$, and $Ce_yFe_xCo_4Sb_{12}$) are widely investigated class of compounds with high thermoelectric figure-of-merit ZT ≈ 1.7 at 850 K [17-18]. The clathrates are generally known to be low-thermal conductivity compounds of Ga, Si, Ge or Sn has emerged as a promising material for high-temperature thermoelectric applications. For the optimized compositions of $Sr_8Ga_{16}Ge_{30}$ and $Ba_8In_{16}Sn_{30}$, thermoelectric figure-of-merit ZT lays around 1.7 at 800 K. In both clathrates and skutterudites, the guest atoms in the compound effectively "rattle" and scatter lattice phonons, suppressing the lattice thermal conductivity resulting improvements in the thermoelectric properties [16, 19-20].

In comparison, the oxide materials generally benefit from being non-toxic, relying on more abundant transition metals, having very good high temperature stability, and exhibit the modest enhancement of figure-of-merit.

In this thesis, I map out the structural phase diagram using de-intercalation and X-ray diffraction techniques. The thermoelectric properties are related to these superstructures, and the electronic structure that leads to this behaviour is investigated. In the next chapter I shall describe the experimental techniques employed in this work.

Chapter 2

Experimental Techniques

2.1 Crystal Lattice

A crystal pattern is made of regularly spaced connected points with pattern repetition of small groups of atoms having translational vectors. In space lattices, in addition to the unit translational distances called lattice vectors with the sides a, b, and c and the angles between these sides α, β, and γ would exist. Using these lattice parameters we are able to label the directions and planes in the lattice by defining the Miller indices, (*h k l)*.

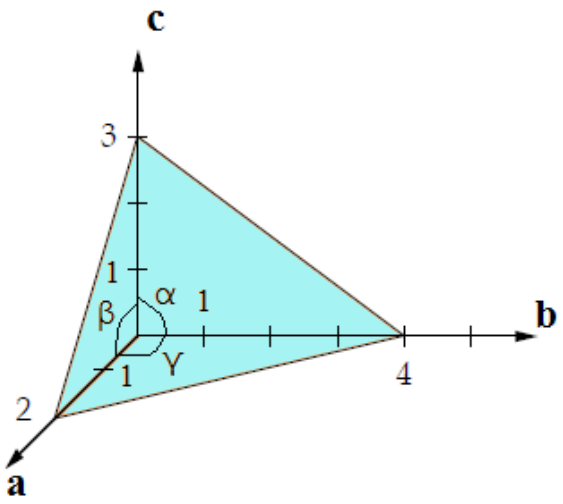

Figure 2.1: Crystal axes with crystallographic parameters

For example, consider the intercept of a plane, with the three crystal axes in terms of primitive vectors (***a, b, c***) at different positions (see figure 2.1). Miller indices can be obtained by taking these points and their corresponding reciprocals (1/2, 1/4, 1/3), and by multiplying all three by the smallest denominator that gives integers.

$$h = 12 \times (1/2) = 6$$

$$k = 12 \times (1/4) = 3$$

$$l = 12 \times (1/3) = 4$$

Hence the Miller indices for this plane are (6 3 4). The set of equivalent planes is referred to as $\{h, k, l\}$. The direction normal to this plane is $[h\ k\ l]$ and the set of normal directions is $<h\ k\ l>$.

2.1.1 Reciprocal Space

In order to understand diffraction data it is convenient to work in reciprocal space, and superstructures can be related to the underlying lattice by comparing the superlattice to the Bragg reflections. The definition of the reciprocal lattice is the set of wave vectors $\boldsymbol{K}$ that yield plane waves with the periodicity of a given Bravais lattice $\boldsymbol{R}$.

$$e^{i\,\boldsymbol{K}.(\boldsymbol{r}+\boldsymbol{R})} = e^{i\,\boldsymbol{k}.\boldsymbol{r}} \tag{2.1}$$

$$e^{i\,\boldsymbol{k}.\boldsymbol{r}} = 1 \tag{2.2}$$

The reciprocal lattice vector, 'τ' is given by,

$$\tau = h\boldsymbol{a}^* + k\boldsymbol{b}^* + l\boldsymbol{c}^* \tag{2.3}$$

The reciprocal lattice vectors of a unit cell (***a*, b**** and ***c****) are related to the real space vectors (***a, b*** and ***c***) by the following equations (2.4):

$$\boldsymbol{a^*} = 2\pi \frac{\boldsymbol{b \times c}}{\boldsymbol{a \cdot (b \times c)}} \quad \boldsymbol{b^*} = 2\pi \frac{\boldsymbol{c \times a}}{\boldsymbol{a \cdot (b \times c)}} \quad \boldsymbol{c^*} = 2\pi \frac{\boldsymbol{a \times b}}{\boldsymbol{a \cdot (b \times c)}} \tag{2.4}$$

where, $\boldsymbol{a \cdot (b \times c)}$ is the volume, V of the unit cell of the direct lattice. The Miller indices notation is used to define the Bragg reflections, so that in reciprocal space it is called the *(hkl)* reflection.

2.1.2 Diffraction

Diffraction is due to the existence of phase relations between two or more waves. The diffraction of X-rays by a crystal builds up a beam of rays scattered by all the atoms of the crystal which lie in the path of the incident beam. The intensity of a diffracted X-ray beam is extremely small compared to that of the incident beam. The diffraction of monochromatic X-rays takes place only at certain angles of incidence that satisfy the Bragg law [21], as shown in figure 2.2. W. L. Bragg gave the first explanation for the actual position of the X-ray diffraction spots from a crystalline material after he successfully analysed Laue's experiments with some necessary conditions of diffraction using a simpler mathematical form in 1913.

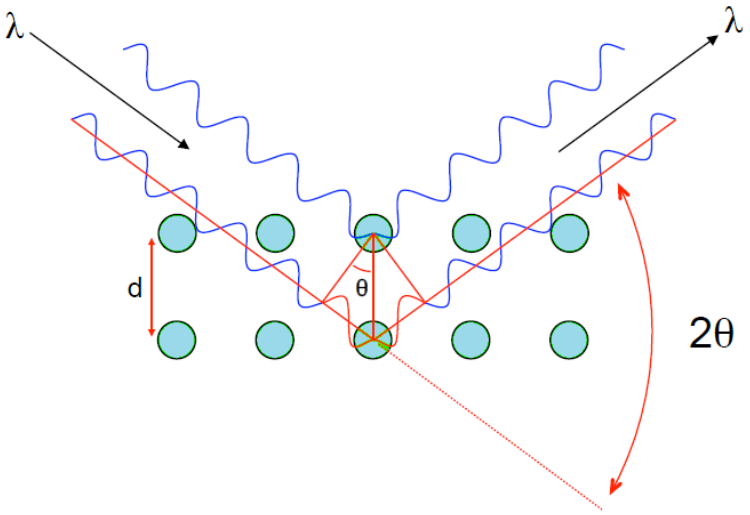

Figure 2.2 Scattering of atoms - Bragg law

By considering the interference condition for waves reflected by successive planes,

$$n\lambda = d_{hkl}\sin\theta_{hkl} + d_{hkl}\sin\theta_{hkl}$$

$$= 2d_{hkl}\sin\theta_{hkl} \qquad (2.5)$$

where, n is an integer signifying the order of atomic planes, λ is the wavelength of the incident radiation, d is the separation of the atomic planes and θ is the angle between the incident radiation and the lattice planes. Thus Bragg's law allows the position of the diffracted spots to be determined in reciprocal space given the size and shape of the unit cell.

The diffraction process is illustrated using the Fourier transform of the real space lattice. Planes of atoms in real space are described by points in reciprocal space at a distance of $2\pi/d$ (see equation 2.4) from the origin in a

direction perpendicular to the original reflecting planes. If the incident beam is plotted in a direction parallel to its real space equivalent, with a sphere of radius of 1/λ through the origin of the reciprocal lattice, the three dimensional locus of vectors with the same length and origin as $\boldsymbol{k_o}$ will indicate all the possible configurations of $\boldsymbol{k}$ for the elastic scattering, which is known to be Ewald sphere or sphere of reflection. Thus, only the reciprocal lattice points intersect with the Ewald sphere will be capable of satisfying the Bragg condition and contributing to the coherent scattering.

With the help of Bragg's law and the Ewald's sphere construction, we can calculate the position of a reflection on the detector, knowing the unit cell dimensions. The position of a diffraction spot is determined only by the metric symmetry of the unit cell.

In order to determine diffraction intensities we consider an incoming plane wave of wave vector $\boldsymbol{k_0}$ ($|\boldsymbol{k_0}| = 2\pi/\lambda$).

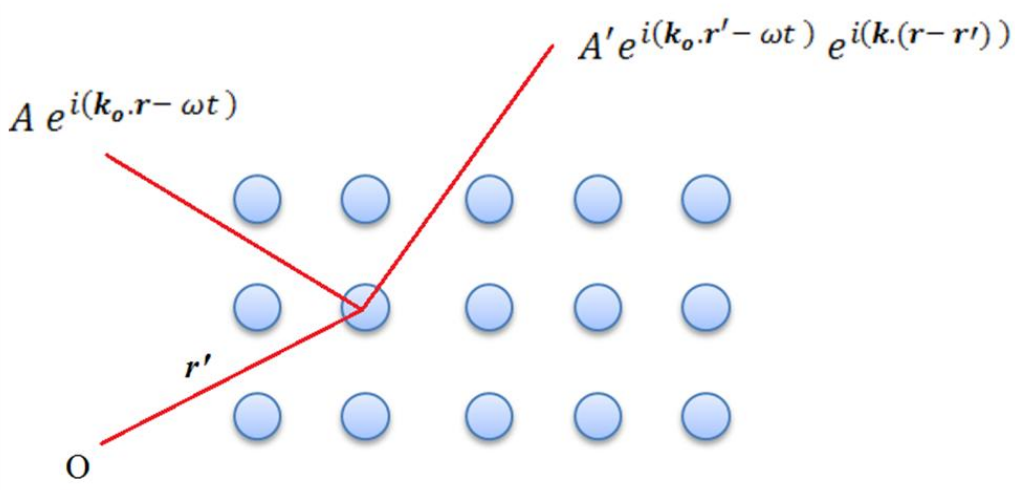

Figure 2.3: Regular array of atoms, with an arbitrary origin O, atom at $\boldsymbol{r'}$ and a detector at $\boldsymbol{r}$.

Each atom reradiates in all directions with an amplitude proportional to

$$e^{i(\boldsymbol{k_o}.\boldsymbol{r}' - \omega t)} \tag{2.6}$$

At the observation point $\boldsymbol{r}$ the amplitude is

$$A' e^{i(\boldsymbol{k_o}.\boldsymbol{r}' - \omega t)} \, e^{i(\boldsymbol{k}.(\boldsymbol{r} - \boldsymbol{r}'))} \tag{2.7}$$

Drop the term in **t** and rearrange as

$$A' e^{i\,\boldsymbol{k}.\boldsymbol{r}} \, e^{i(\boldsymbol{k_o} - \boldsymbol{k}).\boldsymbol{r}'} . \tag{2.8}$$

If the observation point is sufficiently far from the crystal then $\boldsymbol{k}$ is same for all atoms and

$$\text{Amplitude}\,(\boldsymbol{r}, \boldsymbol{k}) = A' e^{i\,\boldsymbol{k}.\boldsymbol{r}} \sum_{\substack{all\ atoms \\ \boldsymbol{r}'}} e^{i(\boldsymbol{k_o} - \boldsymbol{k}).\boldsymbol{r}'} , \tag{2.9}$$

$$\text{Intensity} \propto \left| \sum_{\substack{all\ atoms \\ \boldsymbol{r}'}} e^{i(\boldsymbol{k_o} - \boldsymbol{k}).\boldsymbol{r}'} \right|^2 \tag{2.10}$$

For a Bravais lattice $\boldsymbol{R}$

$$\boldsymbol{r}' = \boldsymbol{R} + \boldsymbol{r} \tag{2.11}$$

$$e^{i(\boldsymbol{k_o} - \boldsymbol{k}) \,.\, (\boldsymbol{R} + \boldsymbol{r})} = e^{i(\boldsymbol{k_o} - \boldsymbol{k}).\boldsymbol{r}} \tag{2.12}$$

Hence we only need to sum over the unit cell

$$\text{Intensity} \propto \left| \sum_{\substack{all\ atoms \\ in \\ unit\ cell}} e^{i(\boldsymbol{k_o} - \boldsymbol{k}).\boldsymbol{r}} \right|^2 \qquad (2.13)$$

In general, atoms have different scattering processes, and this is represented by a form factor that depends on $\boldsymbol{Q = k_0 - k}$. The motion about their equilibrium position leads to the Debye-Waller factor or, more generally, an anisotropic temperature factor.

2.2 Techniques with X-rays

2.2.1 X-Ray Scattering

The main goal of X-ray crystallography is to determine the density of electrons throughout the crystal. From the electron density, the mean positions of the atoms in the crystal can be determined, as well as their chemical bonds, their disorder and various other information. The scattering cross-section is related to the form factor in all the X-ray scattering processes. The atomic form factor is composed of non-resonant and resonant scattering contributions, which arise from the scattering of electrons by the electron clouds of atoms, the scattering of electrons by both spin and orbital magnetic moments (resonant and non-resonant). Let us consider a charge distribution $\rho(r)$, the scattering intensity is proportional to the charge, which in this case is a small element $\rho(r).d$r, located at r and the phase

picked up is $e^{-iQ\cdot r}$. Hence the intensity scattered from this small charge element is $\alpha\rho(r)e^{-iQ\cdot r}d\mathrm{r}$. The atomic form factor describing the scattering power by integrating the electron density profile on a single atom and is given by summing over all *r*, we get *f*(Q):

$$f^0(Q) = \int \rho(r)e^{-iQ\cdot r}d\mathrm{r} \qquad (2.14)$$

Because $\rho(r)$ is a complicated function the determination of f^0 is non-trivial. However, it is clear that for Q = 0, the phase factor is 1 (i.e. all scattering is in-phase), therefore the above equation becomes:

$$f^0(Q=0) = \int \rho(r)d\mathrm{r} = \mathrm{Z} \qquad (2.15)$$

where, Z is the number of electrons. As Q increases the phase factor becomes non-zero and, therefore, phase cancellation will decrease the scattered beam intensity. This usually involves performing some iterative self consistent method on a numerical potential model. The results for various models have been tabulated by using one of the more widely accepted models, based on a relativistic Hartree-Fock interaction, as reported by Cromer *et al.* in 1968 [22]. They summarized their tabulation by fitting the numerical results to the equation

$$f^0(Q) = \sum_{i=1}^{4} a_i e^{-b_i\left(\frac{Q}{4\pi}\right)^2} + c \qquad (2.16)$$

where the parameters $\boldsymbol{a_i}$, $\boldsymbol{b_i}$ and $\boldsymbol{c}$ are given in the International Tables of Crystallography [23]. All of the above equations depend on the assumption

of the scattering centre being a perfect oscillating dipole with no damping, i.e., the charge is allowed to follow the oscillating field exactly. In general the primary interaction is with the electrons in the outer shells, so this is a good approximation. However, if the incident X-ray energy approaches the resonant energy levels of one of the core electrons, then those electrons are excited and take part in the scattering. They are more tightly bound than the outer electrons, and therefore do not obey the free oscillating dipole model. So called anomalous dispersion corrections must be added to take into account the dispersion *(f′)* and dissipation *(f″),* dependent on the incident X-ray energy '$\hbar\omega$', that have to be added to the atomic form factors $f(Q)$. In most cases, anomalous scattering factors f' and f'' are small when compared with *f(Q)*,

$$f(Q,\hbar\omega) = f^0(Q) + f'(\hbar\omega) + if''(\hbar\omega) \qquad (2.17)$$

Most X-ray experiments are performed away from the electron energy levels, as determined by the absorption edges; therefore f^0 is sufficient to describe the atomic form factor. However, there are experiments where scattering near an absorption edge is desirable, and then the anomalous dispersion corrections are necessary.

2.2.2 Resonant X-ray Scattering

Resonant X-ray Scattering (RXS) is an efficient method to investigate crystallographic, magnetic, charge order, orbital structures and excitations with synchrotron light, which complements more traditional and widespread techniques such as non-resonant X-ray scattering and neutron scattering. In RXS, when the X-ray photon energy interacts with the electrons around an atom with energy close to the binding energy of the

electrons, absorption or re-emission can occur, and when the X-ray energy is close to the absorption edge of an atomic species of the sample, the scattering amplitude exhibits a strong dependence on the polarization of the incident and scattered beam [24]. Thus scattering of polarised light can give information on the electron density, and also on the distribution of the magnetic moments present via the polarization dependence.

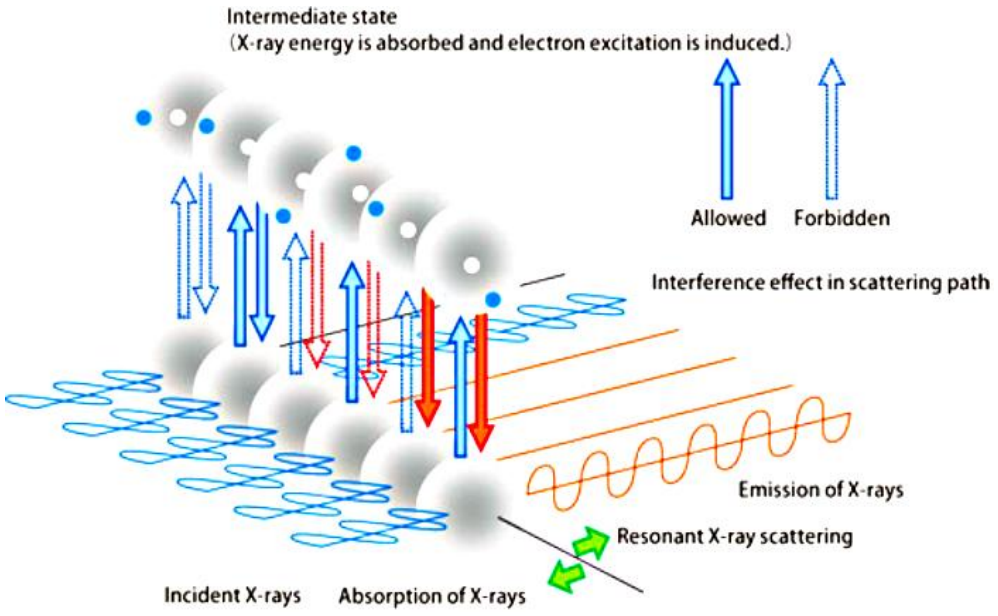

Figure 2.4: Schematic diagram illustrating the principle of resonant X-ray scattering. For the allowed energetic transitions, photons are absorbed by electrons and reemitted [25].

RXS can be used in X-ray diffraction and X-ray spectroscopy. The spectroscopic part presents the sensitivity to the electronic states involved in the ordering, while the diffraction part presents the information about the spatial order. The resonant scattering process provides a qualitative understanding of the strongly enhanced sensitivity to electronic order as illustrated in figure 2.4. Here, the incident photon virtually excites a core

electron into unoccupied states close to the Fermi level, thereby creating an intermediate state of the resonant scattering process.

This virtual transition depends very strongly on the properties of the valence shell and, therefore, results in the tremendously enhanced sensitivity of resonant X-ray scattering to electronic ordering. The decay of the intermediate state again leads to the re-emission of a photon back into the ground state with the same energy as the incident one.

The microscopic interaction of X-rays with matter is commonly described in terms of the scattering amplitude, given by the equation (2.17). The dispersion corrections *f'* and *f"* have to be included, if the photon energy is close to a resonance. The scattering amplitude is related to the differential cross section by the fundamental definition for single scatterers.

$$\frac{d\sigma}{d\Omega} = |f(Q, \hbar\omega)|^2 \qquad (2.18)$$

If the photon energy is tuned close to an absorption edge, $\hbar\omega = E_n - E_i$, where n is an intermediate atomic state. The process can be viewed as absorption of the initial photon exciting an electron to an intermediate state and later it decays by re-emitting the photon.

The polarization analysis in RXS allows an additional tool to investigate the different types of scattering. The polarisation states are relative to the scattering plane, chosen either perpendicular (σ) or parallel (π) to the scattering plane, where the incident and scattered polarisations are denoted as $e_{\sigma,\pi}$ and $e'_{\sigma,\pi}$, which are extended by the wave vectors of the incident and scattered photons. One of the important aspects of the resonant X-ray scattering is given by the polarisation dependence of Δf_n at resonance

scattering. Because of this explicit behaviour, the polarisation of the scattered beam is modified to be different from that of the incident beam. As a result of that, there is a change of the incident polarisation from e_σ to a scattered polarisation e_π, which is called to be σπ- scattering (the rotated channel). The determination of this scattered polarisation can be achieved using a polarisation analyser crystal [26], as shown in figure 2.5.

Using the scattering geometry as shown in figure 2.5, we can perform different types of scanning to investigate the system, such as Energy scan, Azimuthal scan, Radial scan and Transverse scan. In such a way, a variety of polarisation dependencies of resonant scattering can be investigated.

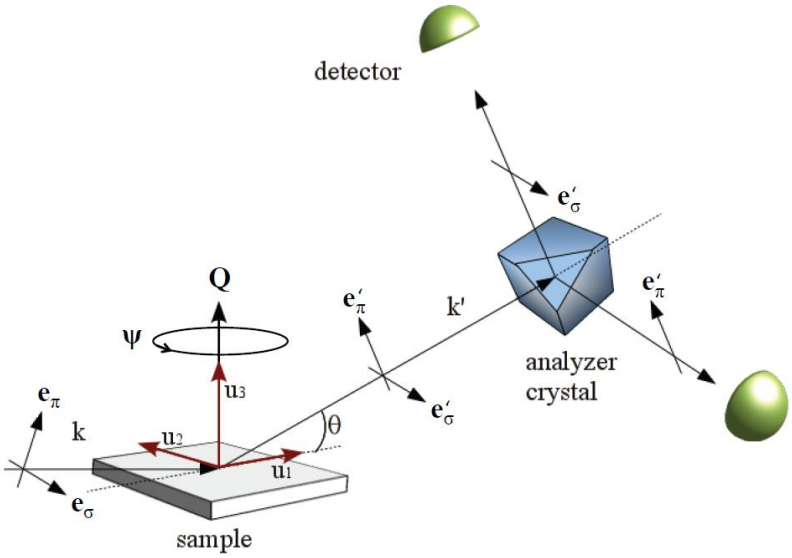

Figure 2.5: The schematic geometry of resonant X-ray scattering. The incident and scattered wave vectors are denoted as k and k'. The incident and scattered polarisations are denoted as $e_{\sigma,\pi}$ and $e'_{\sigma,\pi}$, where σ-refers to a polarisation perpendicular to the scattering plane and π-refers to a polarisation parallel to the scattering plane [26].

This can be done by controlling the incident and scattered X-rays and it is possible to sort out the isotropic and anisotropic electronic scattering. In the azimuthal scan, the incident and resonant scattered intensity is measured while rotating the sample by an angle ψ about the scattering vector Q, which will determine the electronic scattering and help to distinguish the types of scattering. In the energy scan, the photon energy dependence of a given reflection at the scattering vector Q is measured, and it scans the photon energy, while measuring the scattered intensity at Q = (k'-k).

2.2.3 X-Ray Sources

The traditional source of X-rays for typical laboratory experiments is the X-ray tube. Conventional X-ray sources work much the same as the X-ray tube that was invented by Roentgen. A high energy electron beam strikes a metal target such as Cu, Mo, Ag and W, they decelerate rapidly and emit both characteristic radiation (X-ray fluorescence lines) which are concentrated at specific energies and a broad continuous background of bremsstrahlung radiation (breaking radiation) is a continuum from low energies up to a maximum kinetic energy of the electron. A high intensity of X-rays produced at the Kα energy of a target element involves a transition between electron shells. A monochromator can be used to select a particular energy X-ray radiation which passes through the collimator and strikes the crystal.

Unlike the laboratory X-ray source, experiments such as RXS measurements require a broad band of X-ray energies. The intensity of the radiation that can be obtained from the bremsstrahlung radiation is too low for these measurements. Hence, electron storage rings that are used in high-energy physics can serve as an extremely intense X-ray source. When an electron beam is accelerated, for example by using a magnetic field to

cause the beam to follow the curvature of a storage ring, the path of the electrons bends, they accelerate, and therefore they radiate the electron beam as a continuous broad spectrum of synchrotron radiation. The importance of synchrotron radiation can be seen by comparing the X-ray flux available from X-ray tubes with that available from synchrotron sources. The spectral brightness (i.e., the X-ray flux normalized by area that is irradiated and divergence of the beam) of the most powerful sources is more than a billion times greater than that available from X-ray tubes. Another advantage of synchrotron sources is that the synchrotron X-ray beam is polarized and we can select a single wavelength using a series of optics in the hutch to perform required specific experiments.

2.2.4 XRD at Royal Holloway

Xcalibur from *Agilent Technologies* is a lab based X-ray Diffractometer to perform the diffraction experiments especially for the single crystals of smaller size (see figure 2.6). It is a completely automated machine that can be controlled remotely using the *CrysAlis*^{Pro} software. The diffractometer consists of an X-ray tube, a 4-axis goniometer (omega, kappa, phi and theta axis) for sample orientation with a detector arm, which can rotate the sample through almost any angle. The four-axis goniometer is driven by microprocessor-controlled in-built stepping motors. The X-rays are generated by a sealed tube, which is mounted on the goniometer and powered by the high voltage X-ray generator. A molybdenum target material produces X-rays having a single wavelength $\lambda = 0.7093$Å. The X-ray optics contains a high speed shutter located next to the tube shield, the monochromator is used for selecting a single wavelength and collimated through the collimator onto the sample to limit the beam divergence. The

system has a universal charge coupled device (CCD) area detector. The CCD area detector is used to measure the X-rays diffracted from the crystal. The CCD area detector works according to the principle, where the diffracted X-rays enter the detector through a beryllium window in the CCD unit. A scintillation screen absorbs the X-rays and emits visible light, which is conducted via a fibre optic through a CCD chip. The signals are digitised, converting signals to images using an analog-to-digital converter located in the detector head. The image can be visualised in 2D and 3D while analysing the data. The sample can be viewed with the video microscope attached to the stand inside the instrument. The video image is made available through *CrysAlis*^{Pro} software on the PC monitor.

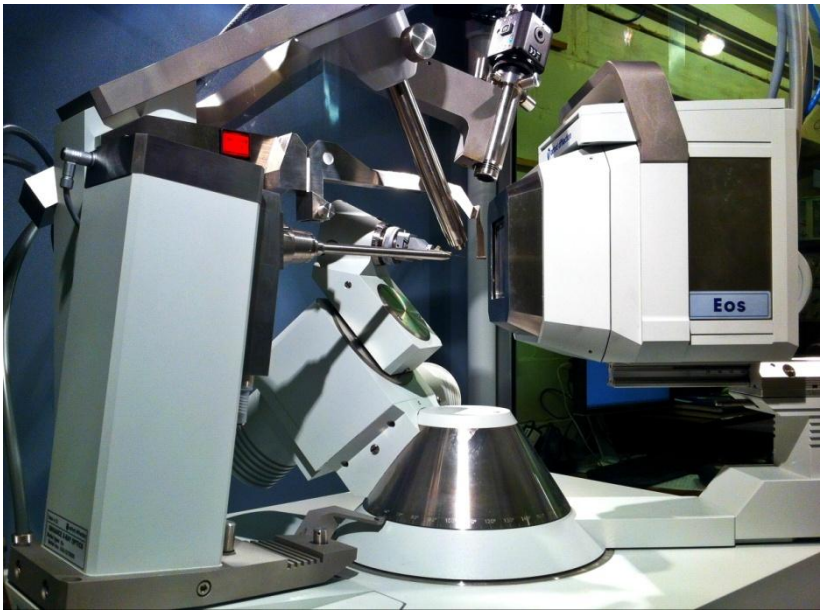

Figure 2.6: Single crystal X-ray diffractometer equipped with cryojet at Royal Holloway.

Oxford Instruments Cryojet5 is a cryojet device that is attached to the XRD to perform temperature dependent X-ray experiments. This device acts as an open flow nitrogen jet specifically designed for cooling and heating the

single crystal samples during X-ray diffraction experiments. The *Cryojet5* can cool and heat the sample within the range of 90K to 500K and the whole device is controlled by the *CrysAlis*^{Pro} software. To run a single complete experiment the XRD would take around 15min to 72 hours to see the full coverage of reciprocal space. Both transmission and reflection type experiments are possible in this diffractometer. A different scan type (sphere, hemisphere and quadrant) can be chosen according to the crystal used for diffraction to view the full reciprocal space. The analysis of the data including the structure determination, integration of peaks can be done using *CrysAlis*^{Pro} software, and the refinement can be done using JANA2006 and SHELX as an additional interface.

2.2.5 I16 at Diamond

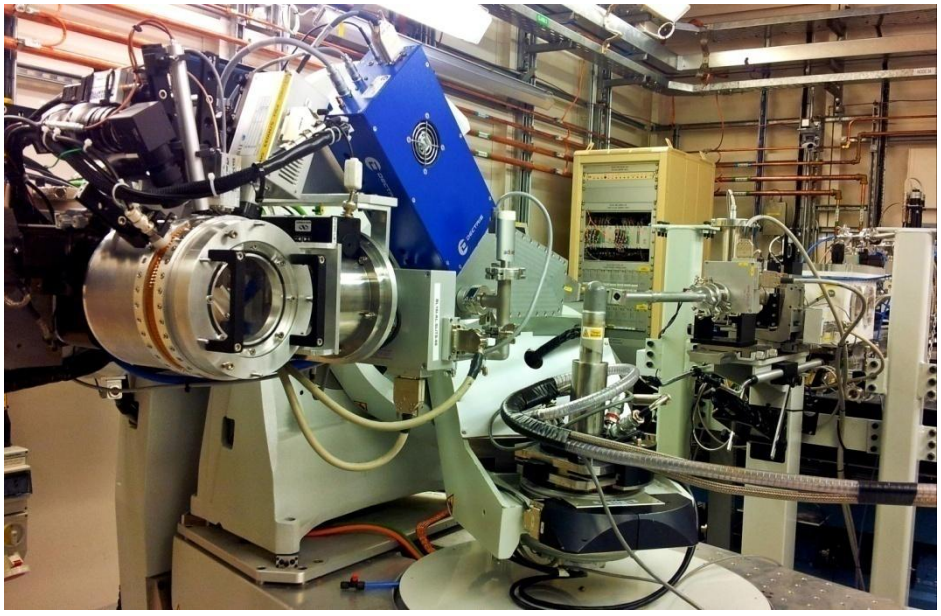

Figure 2.7: I16 beamline at Diamond Lab

I16 is a diffraction beam line at Diamond Light Source, specially designed to perform single crystal X-ray diffraction experiments to study a diverse range of materials and magnetism. This beam line is specifically used for both diffraction and inelastic scattering experiments, and it is fully optimised to combine high flux and high resolution over a continuously tuneable energy range [27].

X-rays are generated via the synchrotron source and focussed into a plane polarised, monochromatic beam in the optics hutch. The single crystal is mounted onto the goniometer and placed in the beam path. During the experiment, the scattered X-rays are measured using the detector arm (Pilatus or point detector and analyser crystal). A variety of scan types can be used by controlling the incident X-ray energy, azimuthal angle, x-ray polarisation and temperature of the sample environment. The I16 instrument is composed of a six axis goniometer used to control the polarisation and azimuthal orientations (see figure 2.7).

2.3 Other Techniques

2.3.1 Crystal Growth

In order to prepare the single crystal samples, a floating zone method was employed. The starting material of nominal composition $Na_{0.8}CoO_2$ was packed into a feed rod and a 4-Xenon lamp floating zone furnace (Crystal System Incorporation, Japan) melts the sample and re-crystallizes it under an oxygen / argon atmosphere (see figure 2.8). The feed rod for the crystal growth process is prepared in the form of cylindrical rod of size 6-9 mm diameter and up to 14 cm length. Some of these feed rods are sintered at the desired temperature between 850°C to 900°C for 6-10 hours under oxygen

atmosphere flow. Oxygen flow during the sintering process reduces the number and period of the sintering cycles relative to air flow [28].

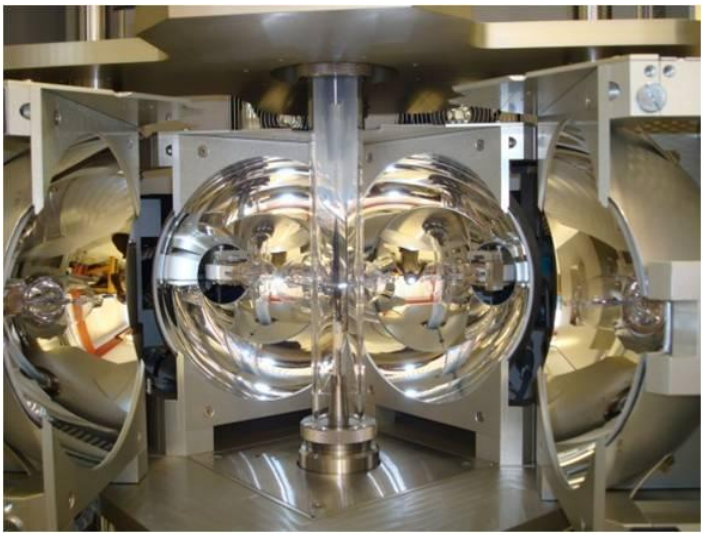

Figure 2.8: Optical floating zone furnace, with four Xenon lamps and the sample in the middle.

Trials were made in which the crystals were grown in different atmospheric conditions. The crystal growth rotational speed also varied between 2 and 10 mm/hr accompanied by a counter-rotation of the feed and seed rods at 35-40 rpm. The grown sample is then cleaved for further characterisation.

2.3.2 PPMS at Royal Holloway

The physical property measurements presented in this thesis were performed using a Quantum Design - Physical Properties Measurement System (PPMS). The PPMS set up is housed within a helium Dewar surrounded by a nitrogen jacket. This system enables the measurement of the electrical resistivity using a resistivity puck, and the thermal properties

using a thermal transport option puck (TTO). The PPMS is used to perform thermo-electric measurements in the range 1.8 K to 400 K. For the thermal conductivity measurements, some heater power is lost at high T (> 300K) to radiative thermal conduction from the hot end of the sample to the surrounding isothermal shield. Hence the highest temperature we used for our system has been constrained to 300K instead of 400K in a high vacuum environment. The accuracy of the reported temperature is ±0.5% [29].

The thermoelectric properties composed of the Seebeck coefficient, the thermal conductivity and the electrical resistivity can be measured at the same time for a single sample to give the thermoelectric figure-of-merit. The Seebeck coefficient describes the thermal diffusion of free charge carriers (electrons or holes), which creates an electric field inside a material when a temperature gradient is sustained. This is the most sensitive electronic transport property of materials and it is very susceptible to variations in the number of carriers which gives direct information of the asymmetry of the density of states. Moreover like the electrical resistivity, this property is very sensitive to subtle changes in the electronic scattering processes and in this regard this technique is considered as a powerful probe to measure the thermopower precisely. The thermal transport system determines the Seebeck coefficient by creating a specified temperature drop between the two thermometer shoes and the voltage is monitored instantaneously.

A measure of the ability of a material to conduct heat is known as thermal conductivity. The measurement of this quantity provides information about scattering of heat carrying phonons and electrons. In the PPMS system, thermal conductivity is measured by applying heat from the heater shoe in order to create a specified temperature of the experiment differential between the two thermometer shoes.

The electrical resistivity is an intrinsic property of the material itself independent of the size and shape of the material, which shows how strongly the material opposes the flow of electric current. In this thesis we used the four point probe method to measure the electrical resistivity for our system.

2.3.2.1 Two point probe:

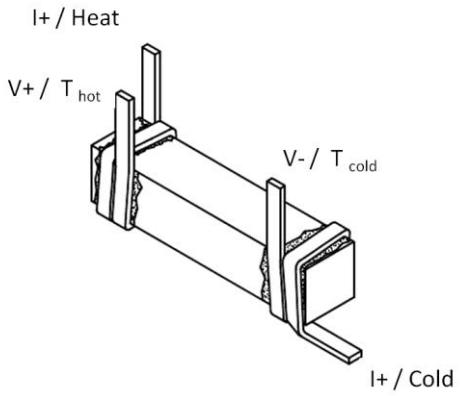

Figure 2.9: Two-probe configuration attached with bar-shaped copper leads [29].

The two-probe lead configuration is the most convenient method to measure the Seebeck coefficient and thermal conductivity, which involves attaching only two leads, where bar-shaped copper leads are used (see figure 2.9). However, the accuracy of the data obtained would be less than for the four point probe method, because heater/I+ and T_{hot}/V+ share one lead while coldfoot/I− and Tcold/V− share the other lead, as shown in figure 2.9. The thermal and electrical contact resistances between the leads and sample contribute to the measured quantities [29].

2.3.2.2 Four point probe:

The four-point probe resistivity measurement is a more successful method to measure the electrical resistivity across the sample. Passing current through the two outer probes, the voltage through the inner probes was measured (see figure 2.10). This allowed the measurement of the sample resistivity. Because a high impedance voltmeter draws little current, the voltage-drop across the probe resistance, the spreading resistance, and the contact resistance are very small [30].

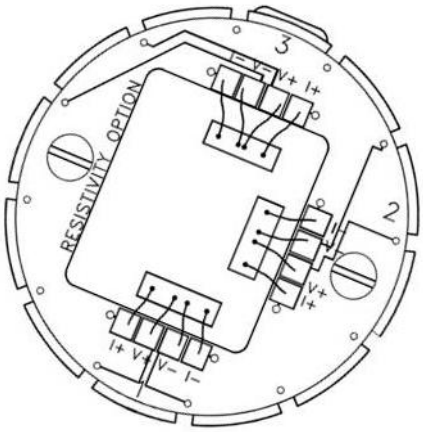

Figure 2.10: Four wire resistivity sample puck with three samples mounted for four-wire resistance measurements [31].

Therefore, this technique uses the electrical impedance in measuring separate current carrying and voltage sensing electrodes, in order to obtain a higher accuracy in the electrical resistance rather than the traditional two probe technique [31]. The resistivity measurement is specifically performed using a four-probe point resistivity puck, their sample preparation and other specifications will be explained in detail in the section 4.3.2.

2.3.3. SQUID/VSM at Diamond

The magnetic property measurements presented in this thesis were all performed using a Quantum Design MPMS SQUID/VSM vibrating sample magnetometer at Diamond Light Source in collaboration with Dr. R. Fan. Single crystal samples of size ~5-6mm were used to measure DC susceptibility in a range of temperatures and field sweeps in different orientations. Highly sensitive magnetic measurements can be performed with superconducting pickup coils, using a superconducting quantum interference device (SQUID) magnetometer [32]. The magnetic moments are measured for the samples in a range of temperatures and external magnetic field applied using one of the two methods. Either the sample is vibrated through the superconducting coils or the varying magnetic response created by an AC field can be measured by the superconducting coils.

Chapter 3

Phase Diagram of Na_xCoO_2

3.1 Abstract

The phase diagram of Na_xCoO_2 was studied using a combination of bromine de-intercalation experiments and X-ray diffraction measurements. A kaleidoscope of Na^+ ion patterns are found as a function of concentration and temperature. A series of commensurate and incommensurate superstructures was found over the range $x = 0.8 - 0.32$. For each phase, the temperature dependence of Na_xCoO_2 over the range $T = 90$ to 500 K was determined. A variety of superlattice phases are mapped out as a function of sodium content and the full temperature dependence is summarised in the phase diagram. The Reverse Monte Carlo method was employed to solve the crystal structures for Na_xCoO_2. At elevated temperatures, distinctive rings of diffuse scattering were observed for Na_xCoO_2 ($x = 0.8$, 0.77 and 0.50) above the sodium order-disorder transition. The short-range ordering for $Na_{0.8}CoO_2$ was modelled using Monte Carlo simulations. A model in which a variety of multi-vacancy clusters ordered short-range was able to reproduce the observed scattering.

3.2 Background

The existence of superlattices from Na_xCoO_2 crystals was first suggested by Dodero and Déportes [33] followed by Jansen and Hoppe [34], but they did not solve the superstructures. The electronic phase diagram of Na_xCoO_2 was proposed as a function of x by Foo et al. in 2004 [35] as shown in Figure 3.1. This is a remarkably rich phase diagram comprising a metal with a spin-density wave (SDW), a Curie-Weiss metal, a charge-ordered insulator, and a paramagnetic metal, which contains a superconductiviting region when water molecules are intercalated between the sodium and cobalt oxide layers.

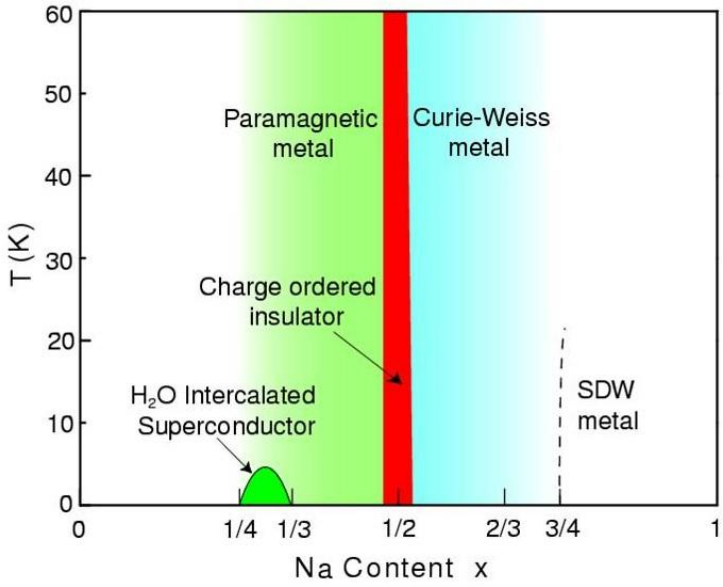

Figure 3.1: Phase diagram of Na_xCoO_2. Ref.: [35].

Zandbergen et al. were the first to systematically map out the superstrutures as a function of x using Br_2 and I_2 de-intercalation methods [36]. Single grains from these powdered samples were studied via single-crystal electron diffraction. The superstructures were found to vary for different grains in the same sample. One problem with this technique is

that it can only see the superstructures in the top few atomic planes. Since Na_xCoO_2 deintercalates/reacts with the atmosphere, the top surface is likely to be different from the bulk, and the stabilised phases at the surface may not be stable in the bulk. The electrons have a relatively high energy and they can sometimes damage the surface of the sample. In some cases the superstrutures were found to change as a function of exposure time to the electron beam. Unlike neutron or X-ray diffraction, it is not possible to model the intensities of the Bragg peaks using electron diffraction. Hence with electron diffraction, it is only usually possible to determine the supercell from the positions of the superlattice peaks. These superstructures were found to be either commensurate with the underlying hexagonal lattice of the Na_xCoO_2 or incommensurate, i.e. the modulation vectors are not related to the underlying lattice by simple fractional values.

The superstructures were first solved using single-crystal neutron Laue diffraction [37]. The first stage in solving these superstructures was to compare the positions of the superlattice peaks with a commensurate hexagonal grid of periodicity $\boldsymbol{a^*}$/N, where N is an integer. This helps to determine the supercell. The positions of the peaks within the supercell were then determined by comparing the intensities of the superlattice reflections with proposed superstructures.

The superstructure models were proposed on the basis of large scale numerical simulations by Roger *et al.* [37]. Monte Carlo simulations were performed using a Coulomb model with short-range repulsion. The ordering principle was found to be the formation of multi-vacancy clusters that order long-range for x corresponding to simple fractional values.

The main elements of the model are shown in Fig 3.2. Na^+ ions can sit on two inequivalent sites shown as red Na1 sites and blue Na2 sites. The energy of the Na1 site is higher due to the short-range repulsion from Co

ions immediately above and below these sites. The occupation of nearest-neighbour Na1 and Na2 sites is ruled out by the large repulsion energy. It is found that, as vacancies approach each other, the energy increases inversely with their separation distance, according to Coulomb repulsion. However, when these two vacancies are next to each other, it is found that the promotion of one Na2 ion to a Na1 site gives a large reduction in energy, since it lowers the energy at the surface of the cluster. This gives the so-called di-vacancy cluster, since it is associated with two vacancies. Similarly, tri-vacancy and quadri-vacancy clusters can also be stabilised.

The ground state energies of all of the simple superstructures based on mono-vacancies, di-vacancies, tri-vacancies and quadri-vacancies are shown in Fig 3.2 (c). It is usually possible to identify only one superstructure at roughly the correct composition with the right supercell. In Ref. [37] excellent agreement was achieved with the neutron intensities in a one-parameter model. It was proposed that the magnetism, superconductivity and thermoelectric properties were controlled by these superstructures.

The aim of this chapter is to significantly extend the range of concentration and temperature, where the sodium ordering is determined using a bulk diffraction technique. Most of the previous work on de-intercalation is on powders and it is not possible to observe superlattice peaks from powder diffraction. However, we are able to solve the superstructures using X-ray diffraction, where we are able to study much smaller crystals [3]. We found that we are now able to control the concentration in single crystals that are large enough for X-ray diffraction measurements. Furthermore, we are able to solve the superstructures in a model-independent manner using Reverse Monte Carlo (RMC). Hence we are able to map out the temperature-composition phase diagram.

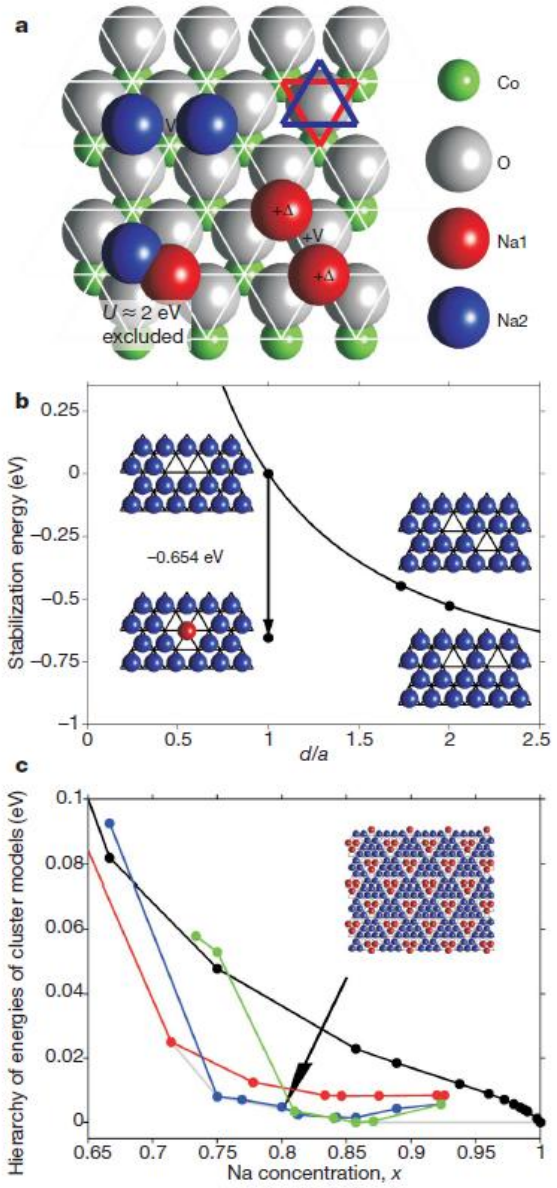

Figure 3.2: (a) The two inequivalent Na sites (Na1: red site, Na2: blue site). (b) Promotion of low energy Na2 to high energy Na1 site leads to the formation of a di-vacancy cluster when two vacancies approach each other. (c) Calculations showing ground-state energies of superstructures for mono-vacancies (black), di-vacancies (red), tri-vacancies (blue) and quadri-vacancies (green); the grey line shows a possible co-existence of phases. The inset shows the trivacancy structure for x=0.8. Ref.: [37].

3.3 Experimental Procedure

3.3.1 Na^+ de-intercalation technique

It is not possible to grow single crystals of Na_xCoO_2, $x < 0.75$ using a floating zone image furnace [28]. Instead various chemical and electro-chemical methods are there to follow that can achieve an efficient Na^+ de-intercalation from $Na_{0.8}CoO_2$. The chemical method of de-intercalating sodium follows chemical reactions which give access to the study of a large portion of the phase diagram. In this method, oxidising agents with CH_3CN (acetonitrile) and H_2O (water), such as I_2/CH_3CN [38], Br_2/CH_3CN [39-40] and $Na_2S_2O_8/H_2O$ [41], $NaClO_3/H_2O$ [35] and $KMnO_4/H_2O$ [42], are employed to oxidise the transition metal redox pair Co^{4+}/Co^{3+}. However, the use of a non-aqueous medium is required to avoid water intercalation between the CoO_2 layers. The de-intercalation by oxidising agent Br_2 in a non-aqueous medium is an efficient method used to reduce the Na^+ content between CoO_6 sheets in layered sodium cobalt oxides. During the de-intercalation process, the oxidation state of cobalt ions changes from Co^{3+} to Co^{4+} [43], and sodium ions move out from the interlayer space to keep the compound electrically neutral. In this thesis I followed this method to achieve ($x = 0.8–0.32$) to study the phase diagram extensively.

Initially, a freshly cleaved single crystal was immersed in a solution of Br_2 with CH_3CN for a particular time. The crystal is measured with XRD before and after the de-intercalation process to study the structural changes in the single crystal. The use of halogens to oxidise metals is a reasonably simple laboratory technique. Yet, the bromine solution is a highly toxic and corrosive element; care must be taken when handling the chemicals by

wearing goggles and anti-corrosive gloves. The de-intercalation process is described by the following chemical equation (3.1):

$$Na_xCoO_2 + \ y\frac{1}{2}Br_2 \longrightarrow Na_{x-y}CoO_2 + \ yNaBr \tag{3.1}$$

A complete de-intercalation to a stoichiometry of $x = 0$ is theoretically possible using a Br_2 concentration of $y = x$. With a knowledge of the starting composition x, the mass of the crystal and the molecular masses of the compounds in the above equation, the amount of Br_2 required to achieve a new sodium concentration of $(x - y)$ would be easily computed. However, in practice a stronger concentration is necessary as the majority of the halogen remains in the acetonitrile solution without reacting with the sodium cobaltate. The addition of acetonitrile is necessary to dissolve the bromine and provide a solution for the deposition of the sodium halide. Adjusting the concentration of the Br_2/CH_3CN mixture solution, phase transformation with different Na concentration, x, will be achieved.

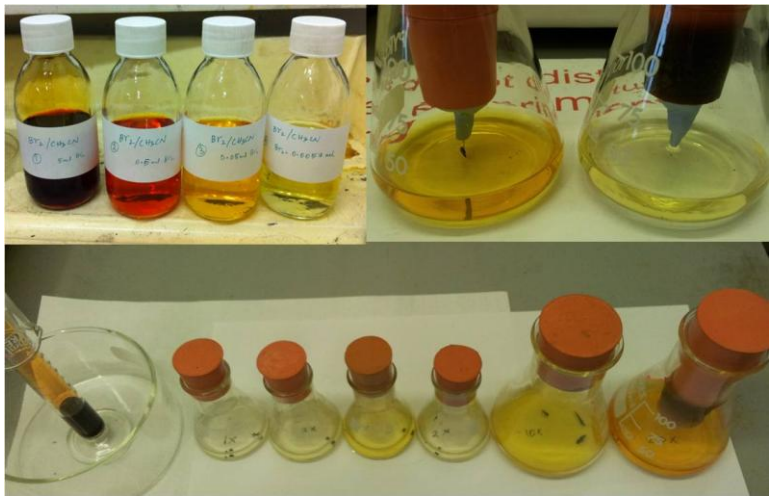

Figure 3.3: De-intercalation solutions using Br_2/CH_3CN in different dilutions of various concentrations of Br_2 in CH_3CN (1X, 2X, 5X, 10X, 30X, 50X, 100X and 1000X.

Table 3.1: Br_2/CH_3CN concentration, time and their corresponding superlattice phases for the bromine de-intercalationn experiments on Na_xCoO_2 single crystal.

% Br_2 in CH_3CN	**Time in Days**	**SL Phases**
0.0057	Pre-Br_2	a*/5, a*/13
0.0057	1	a*/13
0.0057	2-4	a*/7
0.0057	5-7	a*/6
0.0057	8-23	I.C. Phase
0.0057	24-30	a*/2
0.0114	31-45	a*/4
0.0228	46-51	a*/4
0.0570	52-57	a*/4
0.1140	58-59	a*/4
0.1710	60-63	a*/4
0.2850	64-65	a*/4
0.5700	66-70	a*/4
5.7	71	a*/4
20	72	a*/7
20	73	a*/7
30	74	a*/7
30	75	a*/7
40	76	a*/7
40	77-78	a*/7
50	79	a*/10
60	80	a*/10
70	81-83	a*/10
80	84	a*/10
90	85-86	a*/10
100	87-90	a*/10

To achieve x = 0.5, I used a series of steps involving various concentrations of Br_2 in CH_3CN (1X, 2X, 4X, 10X, 30X, 50X, 100X and 1000X) where 1X indicates the theoretical amount of bromine required to remove all of the sodium from the initial concentration 1X=0.0057ml, 2X=0.0114ml, etc., these dilutions are shown in figure 3.3, and their corresponding time with respective superlattice phases are shown in Table 3.1. However, to achieve x from 0.50 to 0.32, I used a series of experiments with stronger oxidising agents than the previous experiments with (20% to 100%) bromine in acetonitrile. The limit of saturation was observed once x~0.32 was reached, and after that no change in structure and c-axis length was observed, even though the sample was kept in pure Br_2 for a long period (~3days).

At the end of each de-intercalation, the single crystal was removed from the solution using filter paper and gently washed several times with generous amounts of dehydrated CH_3CN to remove excess Br_2 and NaBr. All our samples are hygroscopic, i.e. they can easily react with moisture from the air and, therefore, it is necessary to preserve the samples in vacuum controlled desiccators at all times. The de-intercalated Na^+ content precipitates within Br_2/CH_3CN solution itself and that should be collected separately in a bromine waste solution container. The de-intercalation experiment to determine the phase diagram took more than eighty continuous successive de-intercalations to see a clear picture emerge of the change in superlattice peaks with respect to change in concentration of sodium.

3.3.2 X-ray measurements

Measurement using X-ray diffraction (XRD) is one of the most sensitive ways to detect the sodium superstructure peaks. All of the bromine de-intercalated samples have been measured using XRD at Royal Holloway. A single crystal of size 0.3x0.3x0.1mm^3, shown in figure 3.4, was used throughout the de-intercalation experiments at room temperature. The concentration of the sample was determined using the *c*-axis lattice parameter obtained from the diffraction data. The concentrations of the de-intercalation solutions were chosen to give sufficiently mild oxidation to obtain several measurements in each phase in an attempt to avoid missing phases. Other crystals were subjected to the same de-intercalation conditions, and the temperature dependence of the XRD was measured for selected concentrations.

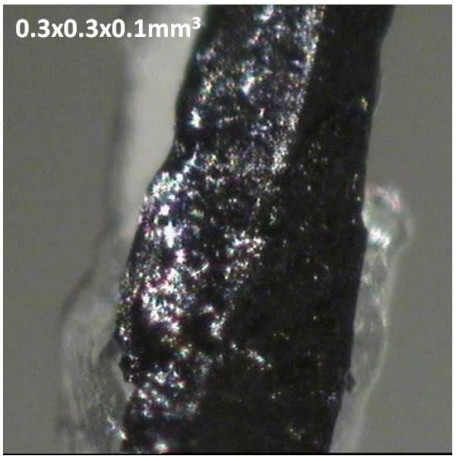

Figure 3.4: The single crystal of Na_xCoO_2 used in the room temperature Br_2 de-intercalation experiments.

The XRD has a 4-circle goniometer where the sample is illuminated by X-rays from a molybdenum Kα1 target having a wavelength 0.7093 Å. It uses

a single area detector placed close to the sample. The sample was measured for several hours with an exposure time of 10sec per orientation, and with the specified scan type to be chosen at the time of run and, in general, several hundred orientations were required to collect a good coverage of reciprocal space. The diffracted X-rays are detected by the powerful area detector based on a popular method of electronic imaging employing a two-dimensional array of small light sensitive elements, known as a charge-coupled device (CCD) where the elements are referred to as pixels. The diffraction pattern was accumulated as an image and the data were analysed using the crystallography software of *Agilent Technologies*. The standard absorption corrections were made to the data before integration. The sample was placed in a stream of nitrogen gas from a *Cryojet5* from *Oxford Instruments*. The nitrogen flow is generated using a heating element in the cryojet. Liquid nitrogen is evaporated by the heater resulting in a temperature stabilised gas flow onto the sample. A second flow of dry nitrogen was used as a shield around the cold jet to prevent ice accumulation. In this way, temperatures were obtained over the range 90K < T < 500K, and the sample was protected from reaction with moisture in the atmosphere. Each data set was analysed using *CrysAlis*^{Pro}, a commercial program especially developed for this diffractometer. This program enables peak searching, peak integration, the determination of orientation matrices, data visualisation and the refinement of diffraction data using JANA2006 as an additional interface.

3.3.3 Reverse Monte Carlo simulations

The standard crystallographic procedure is to refine the parameters of a proposed structure against the integrated diffraction peak intensities using a commercial program. However, sodium cobaltate adopts superstructures and the complexity of the supercell means that reliable refinements cannot

be obtained using standard programs. For that reason, a computer code was written by Dr. D. G. Porter to determine the superstructures of Na_xCoO_2 using Reverse Monte Carlo (RMC) [3]. The prior assumptions are the dimensions of the supercell determined by the positions of superlattice reflections, the approximate concentration and the possibilities of sodium occupying the Na1 and Na2 sites shown in figure 3.2 (a). There are no other assumptions about the occupation of sites within the supercell. In that sense, the results are model independent.

RMC is a variation of the standard Metropolis Monte Carlo (MMC) method where, instead of minimising the energy of the system, the goodness-of-fit parameter χ^2 is optimised. All changes to the structure that decrease χ^2 are accepted, and those that increase χ^2 are also accepted according to the Metropolis algorithm in order to avoid false minima. The process starts at high temperature, where most changes are allowed and a large number of configurations are explored. The temperature is then decreased in a process of simulated annealing and, hopefully, the best fit arrangement of ions is frozen in place at low temperatures. RMC techniques have been successfully applied to a wide range of system including liquids, glasses, powders, polymers, single crystals and magnetic material [44-46].

RMC has now been used to solve the superstructures of Na_xCoO_2 [3, 10]. The RMC code used to solve the superstructures of Na_xCoO_2 in this thesis was written by Dr. D. G. Porter.

To build a supercell, a basic model of the system is generated by building a lattice with N atoms placed in enough unit cells to fill the supercell. This will generate a supercell with two layers of cobalt-oxygen and two layers of sodium. These sodium sites are filled randomly according to the concentrations of sodium. Each of these layers will be filled by the same number of sodium atoms, but their arrangement within the layer will be different, as shown in figure 3.5.

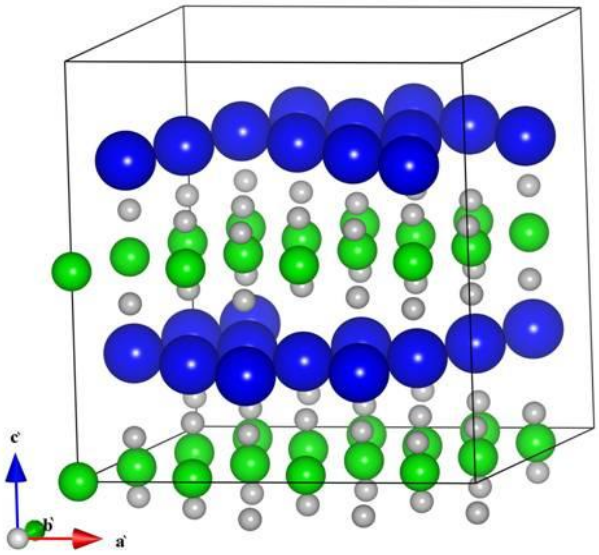

Figure 3.5: Supercell of $Na_{0.8}CoO_2$, filled with 15 Sodium Cobaltate unit cells, with randomly placed sodium ions. Green balls are cobalt, grey are oxygen and blue are sodium. Ref.: [3].

Various changes to the structure were considered, such as sodium hopping and atomic displacements. Sodium ions within the sodium layer, can hop between different vacancy sites and they can hop to both Na1 and Na2 sites. This type of hopping is allowed only within the layer and is restricted between the layers to keep the fixed concentration throughout the process. Each ion in the supercell is able to make small movements from their initial

positions with a small step in a random direction. It is important to keep the centre of mass constant by balancing the movement in each layer equally. After each movement is performed, the calculated intensity changes are determined and compared with experimental values using the χ^2 distribution function in equation (3.2):

$$\chi^2 = \sum_{hkl} \frac{\left(I_{exp} - I_{calc}\right)^2}{\Delta I_{exp}^2} \tag{3.2}$$

where I_{exp} and I_{calc} are the integrated intensities from experimental data, calculation respectively. ΔI^2_{exp} is the error on each value of the integrated intensities obtained from the experimental data [3]. According to the Metropolis method, moves that improve the χ^2 fit are accepted, and a random atomic movement that degrades χ^2 has a certain probability of being accepted. The probability that a bad move will be kept obeys a Boltzmann distribution: (3.3)

$$P = e^{\frac{\chi^2_{old} - \chi^2_{new}}{k_B T}}$$

where, k_B is the Boltzmann constant and T is the (fictitious) temperature. After scores of random moves, χ^2 will no longer improve, and the resulting data are consistent with all the constraints within experimental errors. During each calculation, the process takes 200 temperature steps and the atoms in the unit cell can make 20,000 random movements from their starting positions with various restraints. In simulated annealing, by controlling the fictitious temperature, T, the probability of accepting a poor move can be controlled. At the start of the calculation, the temperature is high, so all the movements within the layer are possible and after a large number of iterations, χ^2 is minimised and the temperature is decreased. Over many temperature steps, the model anneals into a best fit to the

experimental data. The final model is used to calculate two-dimensional cuts through reciprocal space and compared to the experiment. However, the resulting model is not unique and is only one of a vast number of possible agreements that fit the experimental data. Therefore, RMC results must be interpreted as a consistent statistical model rather than the solved structure.

3.4 Results and Discussion

3.4.1 Room temperature concentration dependence

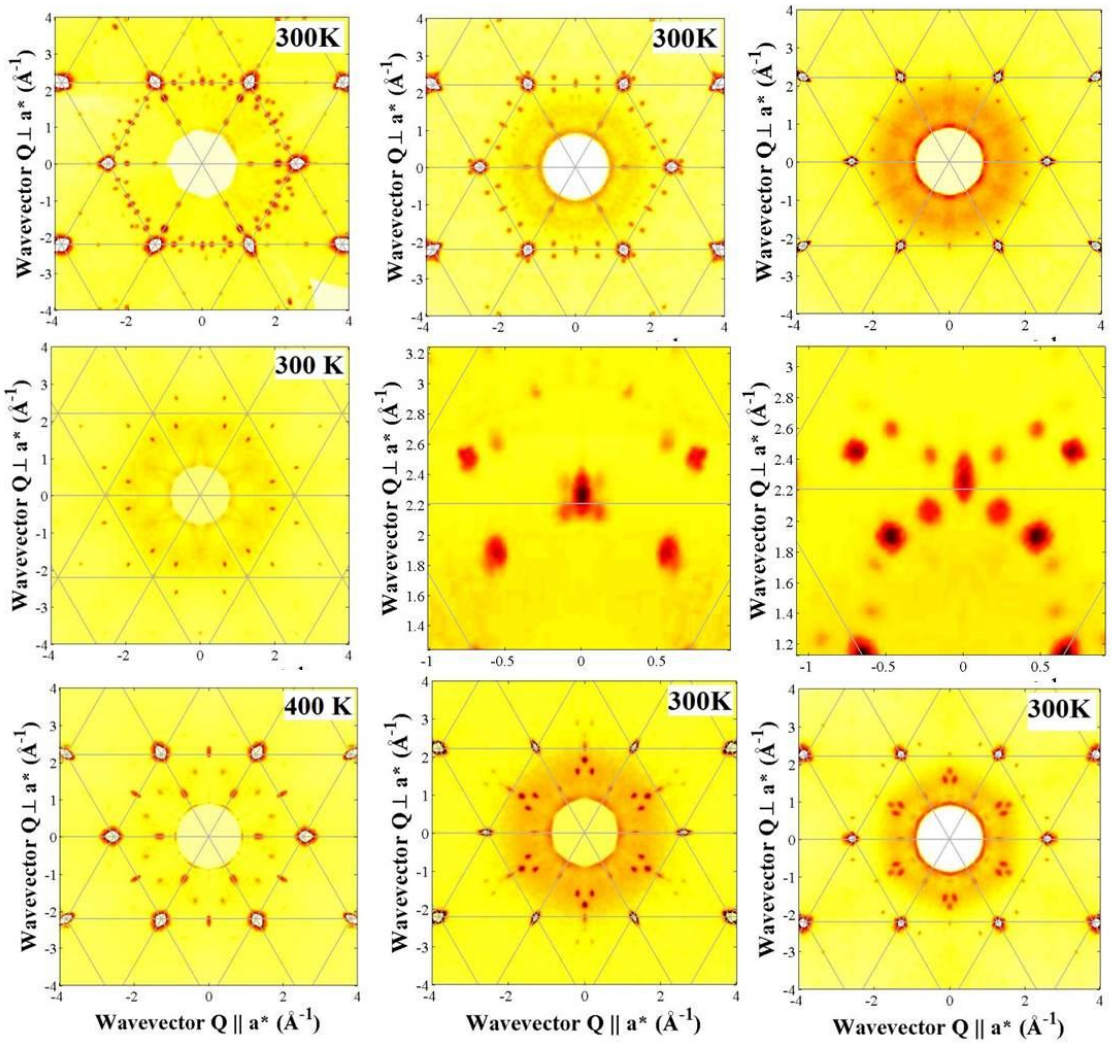

Figure 3.6: X-ray diffraction patterns for the room temperature measurements of Na_xCoO_2 shows a 2D cut through reciprocal space in the (*h, k*, 0) plane at ($x \approx 0.8$, 0.77, 0.71, 0.61, 0.54, 0.5, 0.36 and 0.32) and (*h, k, 2/3*) plane at ($x = 0.67$).

A wide range of the room temperature phases of Na_xCoO_2 were determined by measuring the superlattice reflections using X-rays, which show a variety of patterns corresponding to the x content of the sample that change with

bromine exposure time. The entire XRD pattern for different x is shown in figure 3.6. A wide range of phase diagram de-intercalation experiments has taken about 90 consecutive days to achieve x content from 0.8 to 0.32 showing a variety of superlattice peaks for the same sample undergoing different exposure time in bromine solution. The ratio of the superlattice intensity to the Bragg intensity as a function of exposure to bromine ($\sum_i$ *concentration*$_i$ *x time*$_i$) for all of the deintercalation experiments at room temperature, are shown in figure 3.7. The plot shows a variety of superlattice phases that are separated in segments. Integrating the experimental data gives an accurate estimation of the diffracted intensity at the peak positions in reciprocal space. To integrate the hexagonal Bragg peaks, diffuse peaks and L scans, 3D profile integrations were performed throughout the thesis. This type of integration can calculate an expected spot shape form the strong diffracted spots, scale the shape at the calculated spot position to the pixel value (1 Pixel = 0.0078 $Å^{-1}$, same for both high intense sharp and diffuse weak spots), and then subtract the average background per counted pixel.

The initial sample without any bromine exposure, $x = 0.8$ shows strong $1/5^{th}$ superlattice peaks along with a leakage of $1/13^{th}$ phase at L = 0. The crystal was then dipped in bromine diluted by a factor of 1000 in acetonitrile for 24 hours. The superlattice reflections were measured for three hours that detected $1/13^{th}$ peaks, and were indexed and compared with the main hexagonal Bragg peaks. After 3 days the superstructure changed and the peaks lay on an $\boldsymbol{a^*}/7$ grid, and after another 3 days the superstructure changed again to lay on an $\boldsymbol{a^*}/6$ grid. After a further 4 more days an in-commensurate superstructure formed and the peak positions changed continuously for the next 16 days. Then for four days, no superlattice peaks were detected.

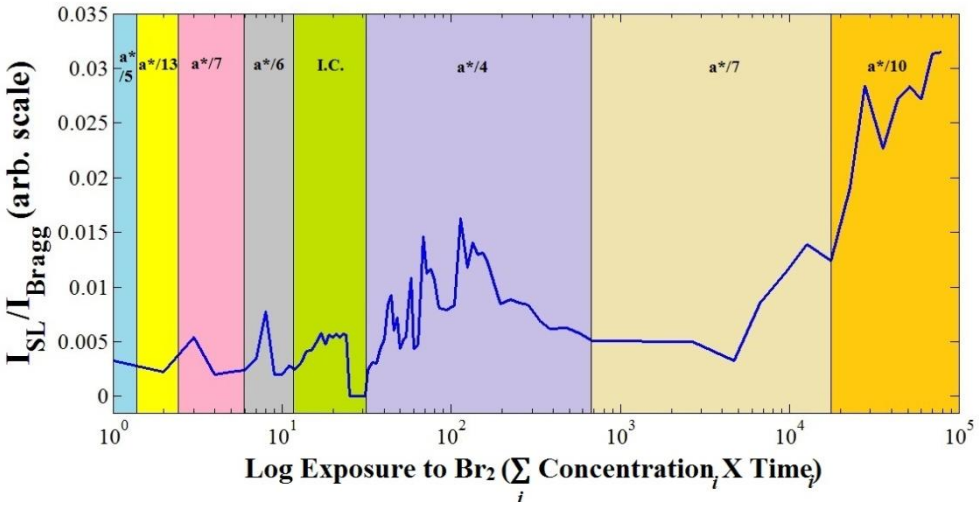

Figure 3.7: Intensity ratio of superstructure phases to Bragg peaks at room temperature as a function of bromine exposure time ($\sum_i$ concentration$_i$ x time$_i$).

Finally, the superlattice reappeared and was found to lie on a ***a****/4 grid on the 32nd day of the bromine experiment with 2X concentration of Br_2 in CH_3CN. As we discussed earlier in this chapter, a stronger oxidising agent is required to remove the sodium content below x=0.5, which continued with a series of steps involved in increasing concentration of bromine solution from 4X to 1000X. Eventually, after an increase in the concentration of oxidising agent, the sodium content was further reduced to x~0.36, which shows a superlattice phase that lie on ***a****/7 grid. The same structure continued for a long time as a stable phase at this concentration. Further increasing the concentration of Br_2 in CH_3CN gradually to 100% of bromine without any addition of acetonitrile. The c and a axis changes gradually as a function of x, where the sodium is removed by bromine vigorously. Furthermore, the deintercalation experiments show that the superlattice phase changed to a new superlattice phase and the peaks lie on ***a****/10 grid. Eventually, the de-intercalation saturation limit of bromine which removes the sodium content from Na_xCoO_2 was observed. At this stage, there are no any superlattice phase changes and also no change in c-axis length was

observed. To verify that, the sample was dipped in 100% pure bromine without any addition of acetonitrile for three days continuously, then the final sodium content was estimated to be $x = 0.319$.

Although there are numerous methods available to determine the x content in Na_xCoO_2, the c-axis length is the most capable way to determine the sodium content [47]. This is because, the c-axis length increases as the sodium concentration decreases. Thus simple data from X-ray diffraction itself might be used to estimate the Na_x concentration [48]. The length of c-axis increases monotonically with bromine experimental time within experimental uncertainty. This is because the inter layer spacing along c-axis increases with decrease in x due to higher electrostatic repulsion forces between the charged CoO_2 layers. We observed a gradual increase from the initial distance along c-axis as a function of bromine exposure time, as shown in figure 3.8, where the distance of a- (or) b-direction decreases at the same time as x decreases.

The removal of Na^+ from Na_xCoO_2 introduces Na^+ vacancy sites on to the Na layers which oxidises partially the Co ions and consequently the ionic radius of Co ions decreases. Here the bonding between the cobalt and oxygen increases due to the removal of electrons form the Na^+ by the de-intercalation process. The reduction in the unit cell in the *ab*- direction is appreciable due to the restriction of Co-O bond distance in CoO_6 octahedra and a similar effect was observed for Li_xCoO_2 [49].

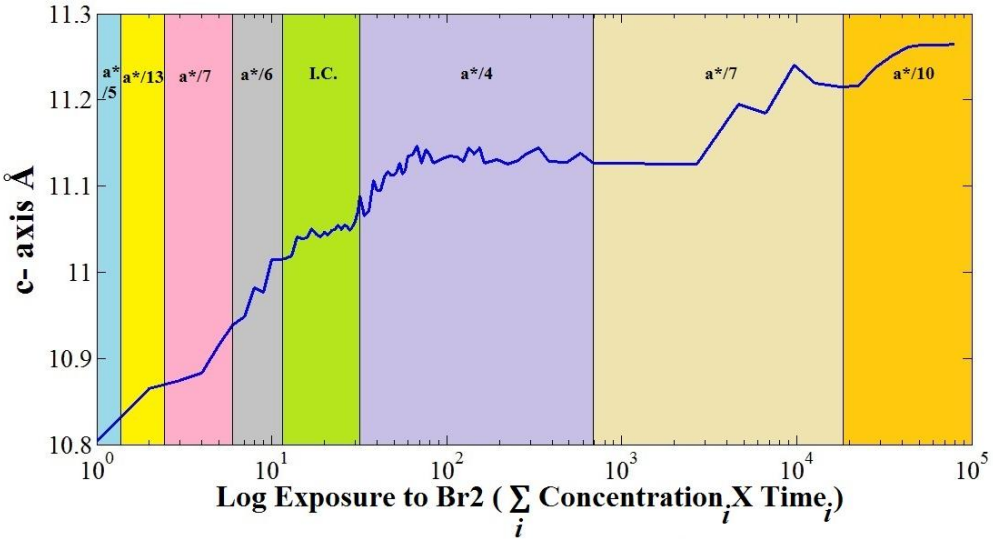

Figure 3.8: c-axis length increases monotonically as a function of bromine exposure time ($\sum_i$ concentration$_i$ x time$_i$) showing a variety of superlattice phase separated in segments.

Using fixed points for the commensurate superstructures I estimated through the variations of concentration on c-axis by least square fit [47].

The equation is given by:

$$c \approx 11.574 - 0.9699 \cdot x \tag{3.3}$$

The c-axis as a function of x is plotted for the known commensurate structures [50-54], as shown in figure 3.9. In figure 3.10, equation (3.3) is shown to be consistent with the published literature. The lattice parameter values for different x are listed in Table 3.2.

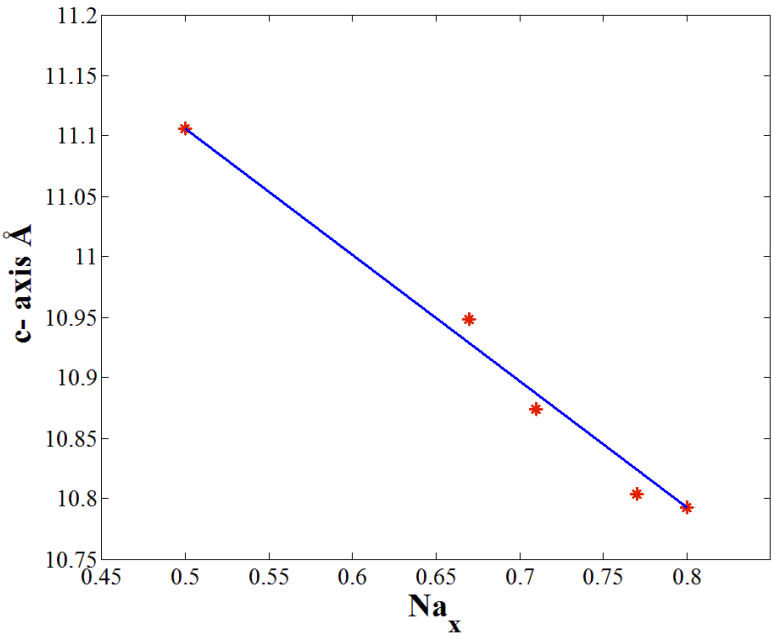

Figure 3.9: c-axis as a function of x for the known commensurate structures.

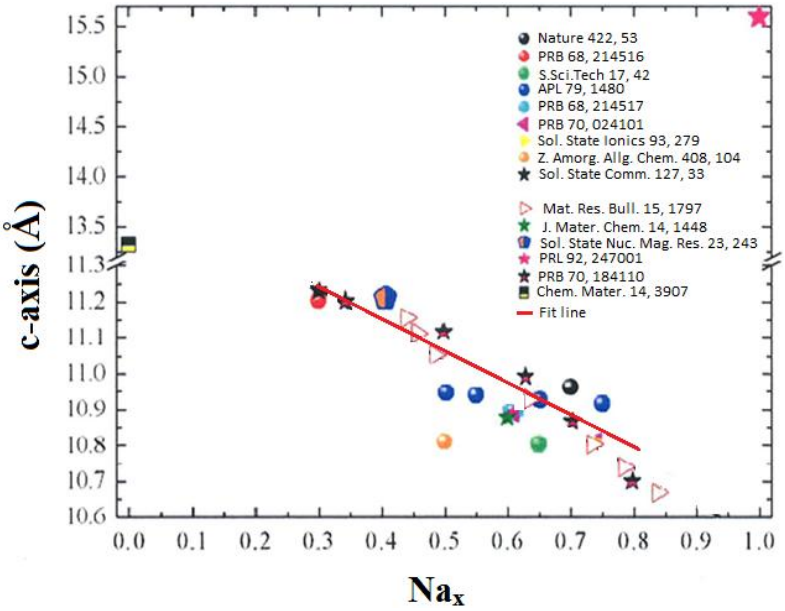

Figure 3.10: c-axis length comparison to other works, Ref.: [47]. The red line in the figure shows an increase in c-axis length over the range $0.32<x<0.8$.

Table 3.2: Lattice parameters for Na_xCoO_2 as a function of x.

Na_x (%)	**c (Å)**	**a=b (Å)**
0.8	10.793(6)	2.853(4)
0.77	10.804(5)	2.840(3)
0.71	10.874(7)	2.831(3)
0.67	10.948(5)	2.827(3)
0.5	11.116(5)	2.819(2)

3.4.2 Structure determination

In order to determine the supercell, the procedure is as follows. Superlattice peaks are identified by taking (*h, k*) cuts for successive values of L in order to identify the plane with the maximum superlattice intensity. The in-plane supercell is obtained in two stages. Firstly, hexagonal grids of a*/n are plotted over the data in order to narrow down the range of supercells. Secondly, bearing this information in mind, the supercell is determined by trial-and-error. Previous diffraction studies and DFT calculations are good starting points. In cases where the superstructure is not known, it is necessary to test all of the arrange of di-vacancy and tri-vacancy cluster that have approximately the right size. Finally, the reciprocal superlattice is plotted over the data and all of the superlattice peaks must lie on this reciprocal lattice. Cuts through the data with one component along the ***c**** direction allow the size of the supercell along the ***c***-direction to be determined. Ultimately, the type of multi-vacancy cluster and the positions of the multi-vacancy clusters with the supercell determine intensities and locate systematic absences.

3.4.2.1 $Na_{0.8}CoO_2$

The crystal structure of a $Na_{0.8}CoO_2$ single crystal was studied using XRD and a cryojet was used to change temperature during the experiment to observe different diffraction patterns. A full coverage of reciprocal space was mapped using the exposure time of t = 10 sec/per point. At room temperature, there are 6 fold rings of ***a****/5 superlattice peaks around the main hexagonal Bragg reflections, where the separation between hexagonal reflection and superlattice peak is $1/5^{th}$ of the distance between hexagonal positions. Along with the ***a****/5 reflections, an extra phase was present between the principal Bragg reflections that indexed on a commensurate grid with lattice size $1/13^{th}$ of the reciprocal lattice. Figure 3.11 illustrates

how these superlattice peaks can be indexed and the supercell vector of this phase is given by:

$$\boldsymbol{a}' = 3\boldsymbol{a} - \boldsymbol{b}$$

$$\boldsymbol{b}' = 4\boldsymbol{a} + 3\boldsymbol{b}$$

$$\boldsymbol{c}' = 4\boldsymbol{c}$$

Additionally, intense peaks lay half way between the principal Bragg reflections due to contamination from the X-ray source with wavelength λ/2, as shown in figure 3.12. The cut through reciprocal space in L-direction shows that 1/13th reflections are peaked at the 1/4th and 3/4th positions in L-direction. The 1/13th superlattice peaks are from a minority phase for x = 0.8. They are described in detail in the next section on x = 0.77.

The sample was rapidly quenched to 100K, by placing the sample in the cryojet flow at 100K for long time and the X-ray measurements at T = 100K show a set of superlattice reflections that lie on a commensurate grid with lattice size 1/15th of the hexagonal reciprocal lattice unit length, as shown in figure 3.13. This phase has been observed previously and it is comprised of fully ordered stripes of tri-vacancy clusters [3]. The superlattice reflections were indexed on a commensurate grid by the following supercell vectors:

$$\boldsymbol{a}' = 3\boldsymbol{a}$$

$$\boldsymbol{b}' = 4\boldsymbol{a} + 5\boldsymbol{b}$$

$$\boldsymbol{c}' = \boldsymbol{c}$$

For the measurements at 200K shown in Fig 3.12, a fast cooling method was employed, where the sample was cooled to 200K in 50 K/min steps and this shows 1/15th superlattice reflections identical to the peaks at 100K.

However, for slow cooling, the sample was cooled down to 200K from room temperature in 5K/min steps, the superlattice phase shows 12-fold rings of superlattice reflections instead of 6-fold rings where the sodium ions were arranged in the square lattice of tri vacancy cluster, and they were indexed on a commensurate grid with lattice size $1/15^{th}$ of the reciprocal unit length using a supercell vectors:

$$\boldsymbol{a}' = -\boldsymbol{a} + 3\boldsymbol{b}$$

$$\boldsymbol{b}' = 4\boldsymbol{a} + 3\boldsymbol{b}$$

$$\boldsymbol{c}' = \boldsymbol{c}$$

This phase was first observed using neutron diffraction [37] and it consists of a square array of tri-vacancy clusters. Figure 3.15 and 3.16 show the L dependence of the scattering for the striped and square phases, respectively. The scattering is peaked at integer L, confirming that these superstructures have the same periodicity as the parent compound along the *c*-direction, i.e. two planes of sodium ions per supercell.

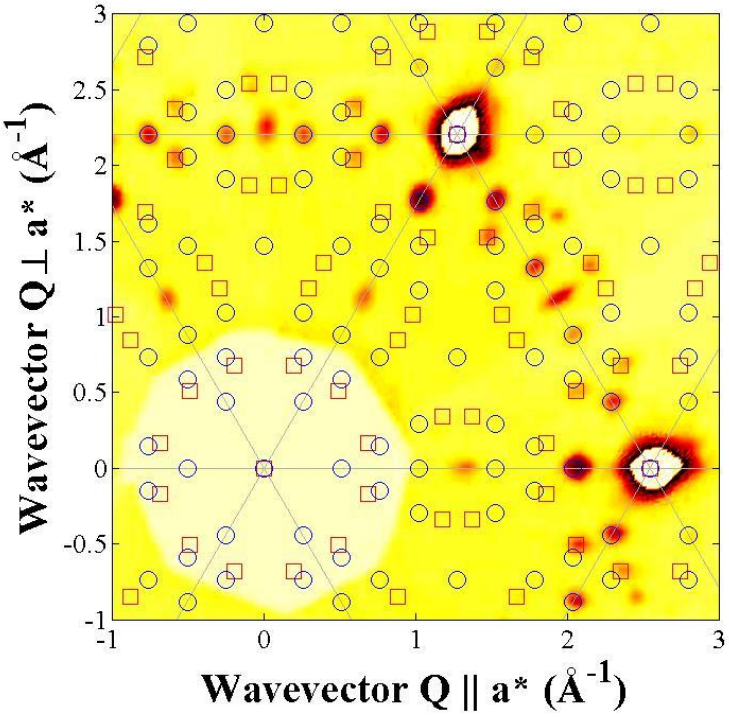

Figure 3.11: X-ray diffraction pattern of $Na_{0.8}CoO_2$ at (h, k, 0) plane at room temperature. Different coloured shapes show difference in the superlattice phases observed for this concentration. Blue circles indicate the peaks at the $1/5^{th}$ positions, red squares the weak $1/13^{th}$ positions.

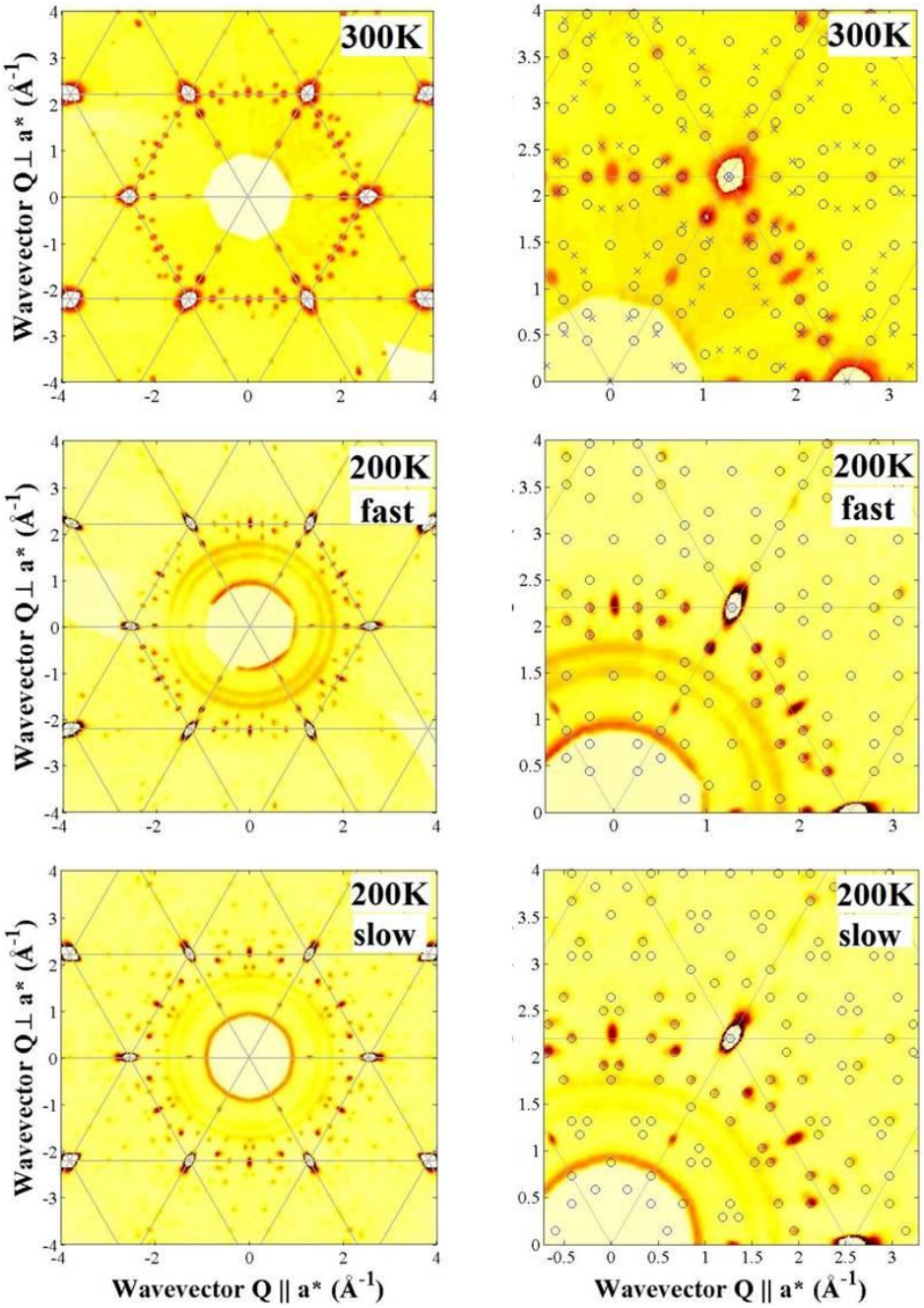

Figure 3.12: $Na_{0.8}CoO_2$ X-ray diffraction pattern for different temperatures. Each pattern shows a 2D cut through reciprocal space in the (*h*, *k*, 0) plane. At 300K XRD patterns show 1/5th and 1/13th peaks indicated by circles and crosses respectively. At 200K fast cooling shows 1/15th peaks for the ordered stripe phase and 200K slow cooling shows 1/15th peaks for the square phase indicated by circles.

In the case of the ordered stripe phase at 100K and square phases at T = 200 K, the XRD data were modelled using RMC. The models and calculated intensities obtained after simulated annealing are shown in Fig 3.14. The agreement with the experimental data in Fig 3.12 and 3.13 are excellent.

In order to reproduce the observed scattering at room temperature, it is necessary to introduce disorder of the positions of tri-vacancy clusters within stripes. This so-called disordered stripe phase accurately reproduces the experimental data.

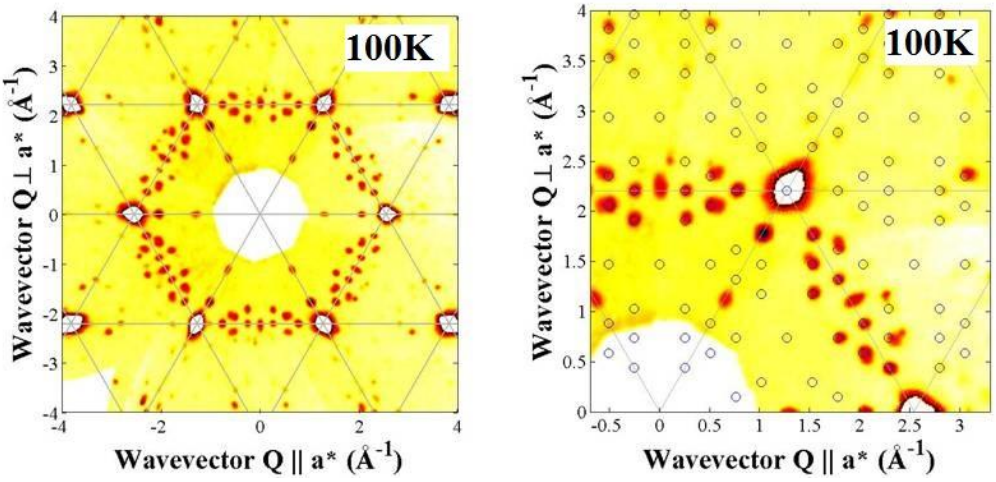

Figure 3.13: $Na_{0.8}CoO_2$ X-ray diffraction pattern for T=100K. Each pattern shows a 2D cut through reciprocal space in (*h, k,* 0) plane.

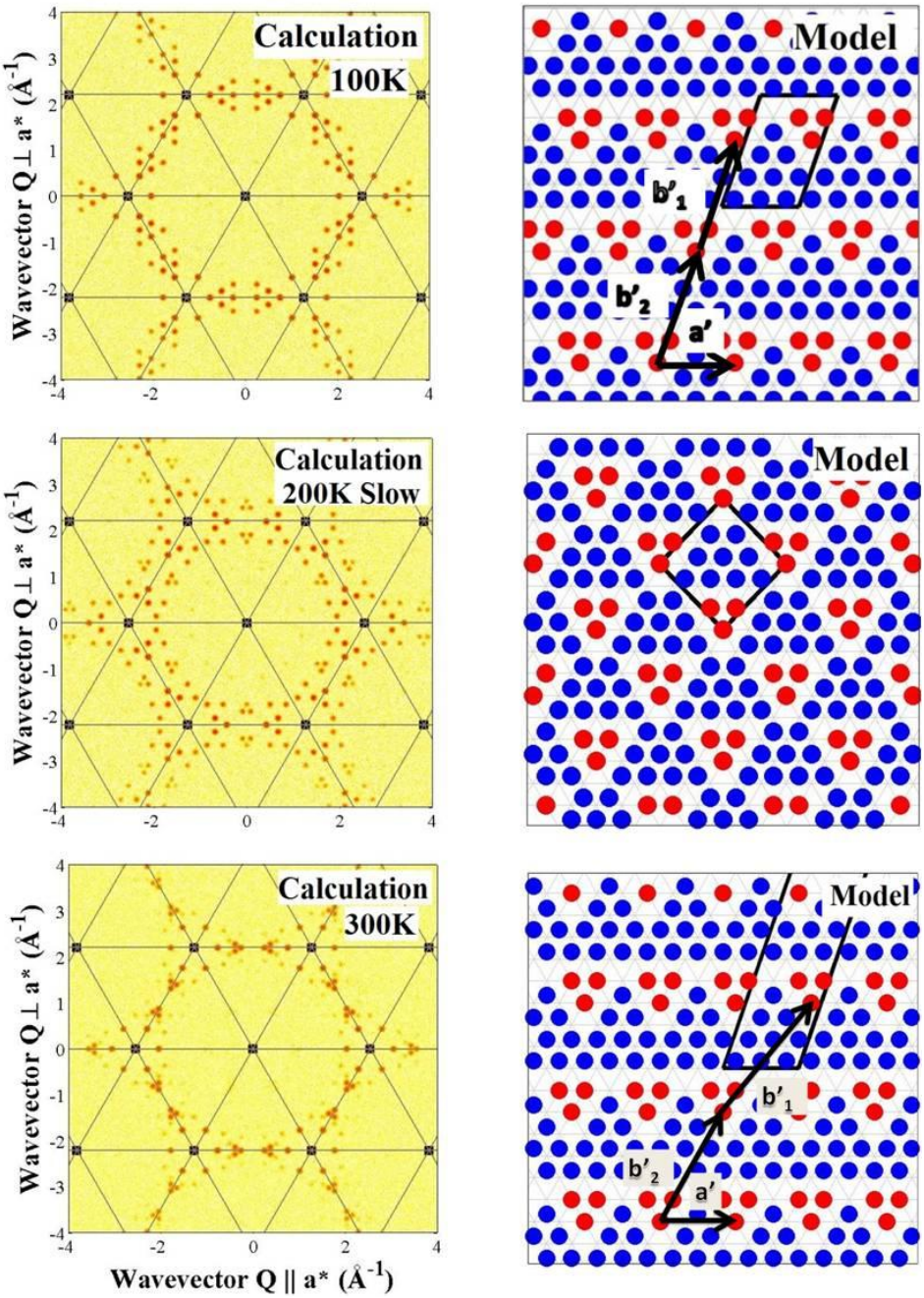

Figure 3.14: At 100K, RMC calculation show 1/15th peaks and the structure model shows an ordered striped phase. At 200K slow cooling method, RMC calculation show 1/15th peaks at (*h, k, 0*) and the structure model shows a square phase. At 300K the calculated intensity shows 1/5th peaks at (*h, k, 0*) and a model showing a random stripe phase. Red spheres are Na1 atoms of tri-vacancy clusters and blue are the Na2.

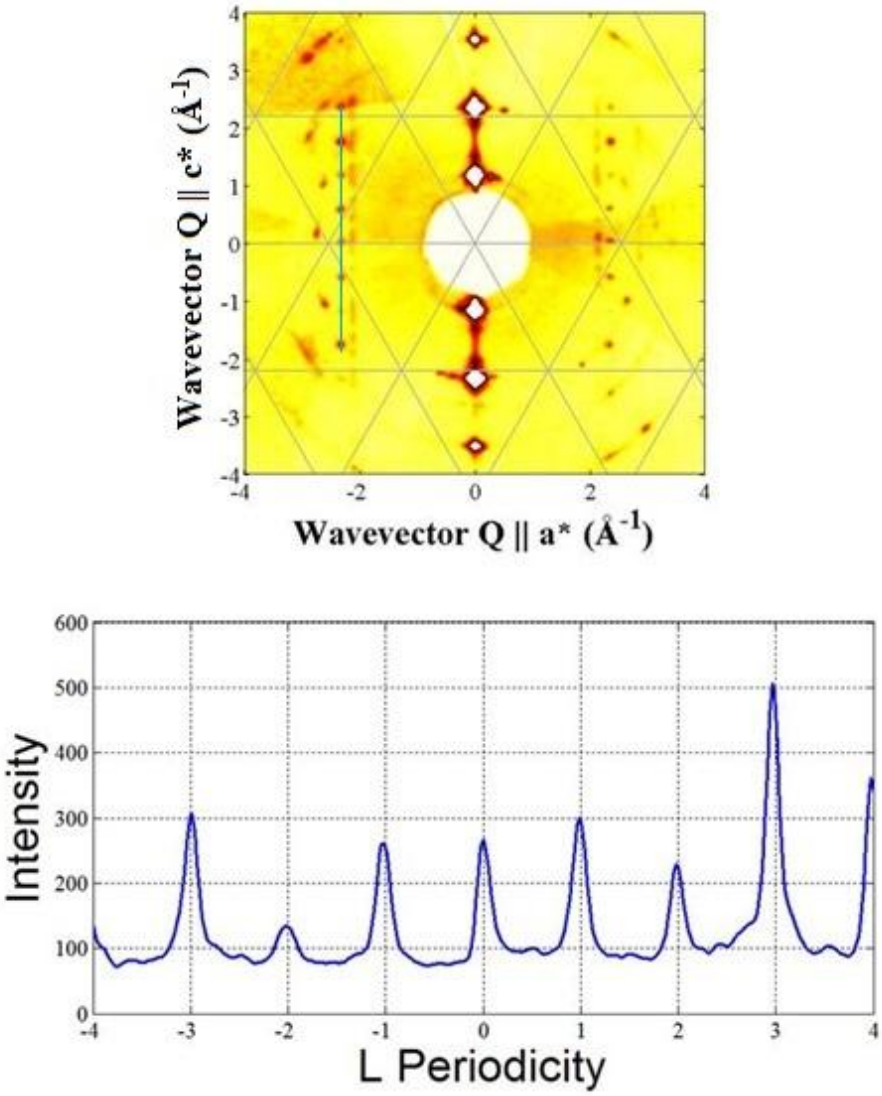

Figure 3.15: X-ray pattern for $Na_{0.8}CoO_2$ at T=100K showing 1/15th peaks indciated in green line in L-direction corresponding to the striped phase. The 1/15th peaks were arranged in the integer positions in L-dependence of the reciprocal space.

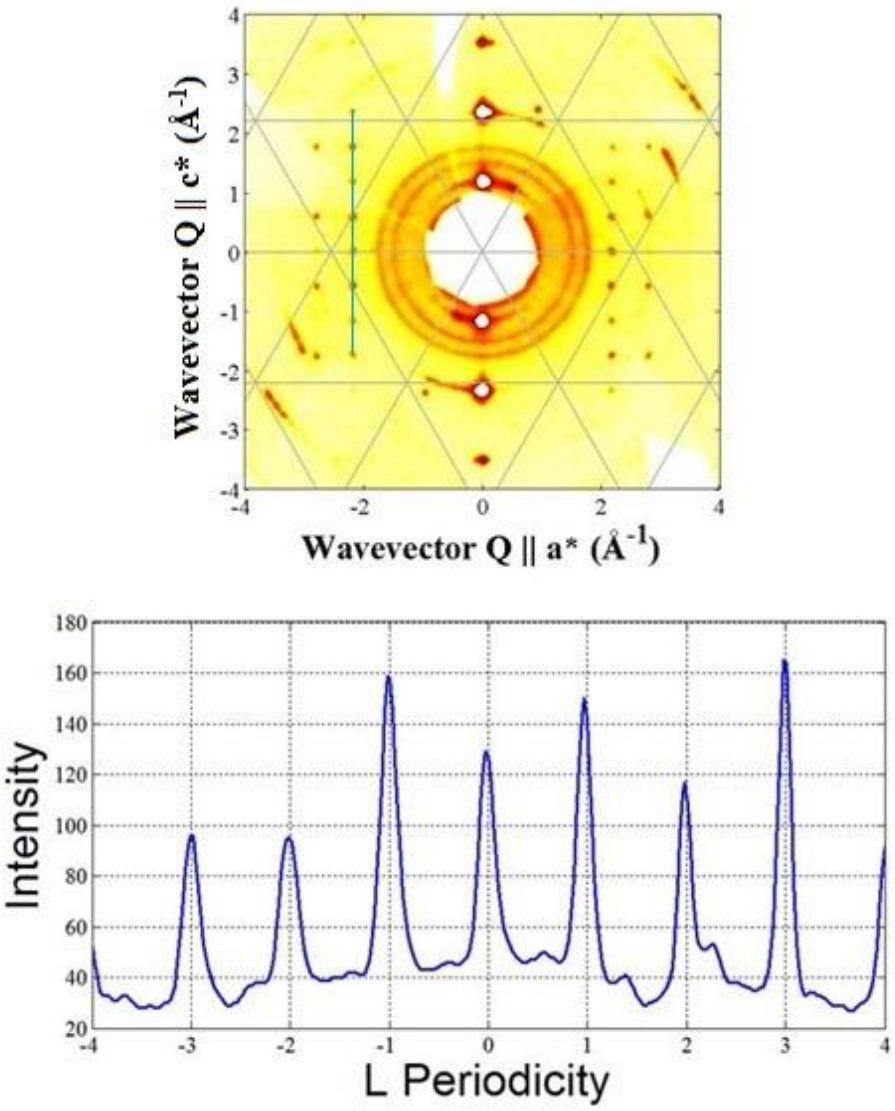

Figure 3.16: X-ray pattern for $Na_{0.8}CoO_2$ at T=200K showing 1/15th peaks indicated in a green line in the L-direction corresponding to the square phase. The 1/15th peaks were arranged in the integer positions in L-dependence of the reciprocal space.

3.4.2.2 $Na_{0.77}CoO_2$

The XRD pattern for $Na_{0.77}CoO_2$ at room temperature shows superlattice reflections that correspond to $\boldsymbol{a}^*/13$, see figure 3.17, where the peak intensity lies on a hexagonal grid and the elements are indexed on a commensurate grid with lattice size $1/13^{th}$ of the hexagonal lattice unit length. The cut through reciprocal space in the L-dependence plots show that the $1/13^{th}$ peaks appeared at $1/4^{th}$ and $3/4^{th}$ order in the L-direction (see figure 3.20), and are considered as a dominant phase at $x \sim 0.77$ rather than as a minority phase at $x \sim 0.8$.

The supercell vectors are

$$\boldsymbol{a}' = 3\boldsymbol{a} - \boldsymbol{b}$$

$$\boldsymbol{b}' = \boldsymbol{a} + 4\boldsymbol{b}$$

$$\boldsymbol{c}' = 4\boldsymbol{c}$$

Figure 3.17, shows the $1/13^{th}$ superlattice reflections along with the main Bragg reflections were observed at L = 0, 0.25, 0.5 and 0.75. It is not yet possible to perform RMC simulations for the composition, since the 8-plane sodium layer periodicity makes the supercell too large. The superstructure model shown in Fig 3.19 determined by David Voneshen, [Private Communication] gives the scattering intensity on Fig 3.18, and these calculations are in excellent agreement with the experimental data in Fig 3.17. The in-plane pattern of tri-vacancy droplets agrees perfectly with the predictions of density-functional theory (DFT) using the generalized-gradient approximation (GGA) for $x = 0.77$ [53]. We find that this superstructure has a rather complicated stacking sequence with c periodicity of eight sodium layers. The previously proposed superstructure

for $Na_{0.77}CoO_2$ comprising mixed di-vacancy and tri-vacancy clusters has the wrong periodicity along the *c*-direction [52].

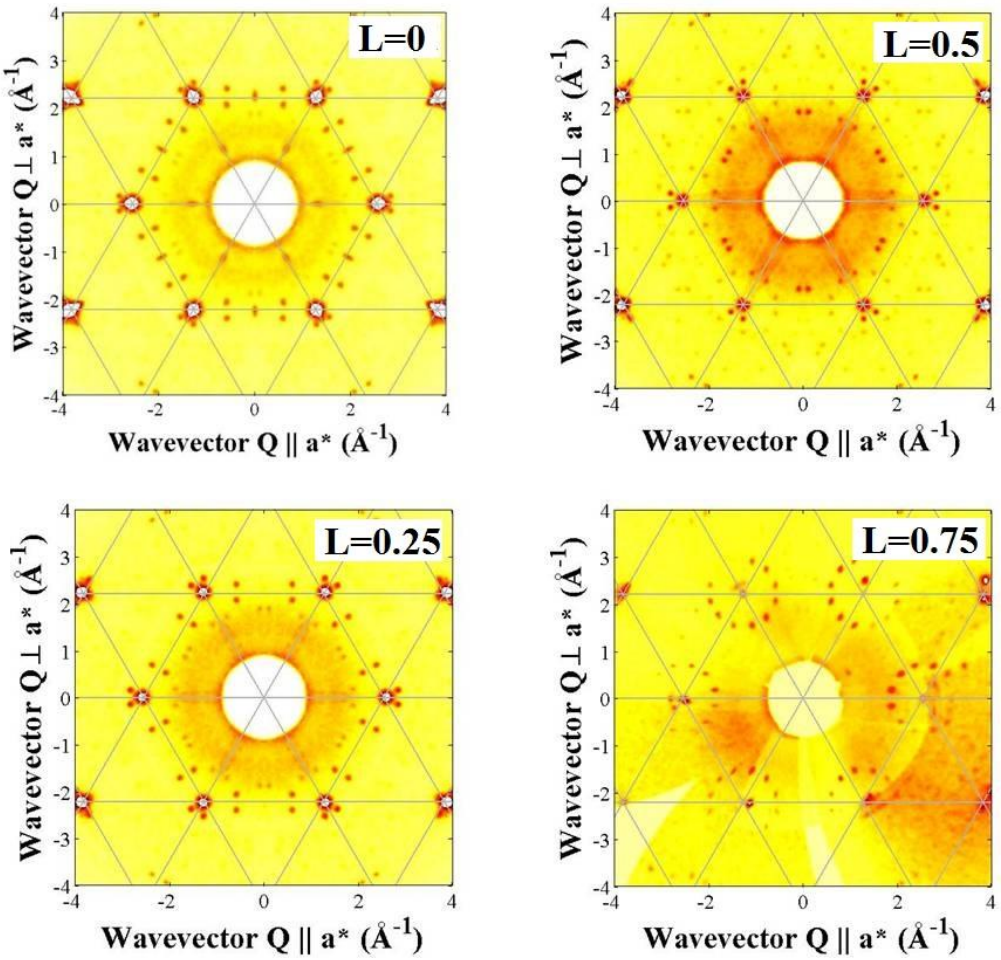

Figure 3.17: X-ray patterns of $Na_{0.77}CoO_2$ at (*h, k, 0*) at T=300K, where each pattern is a 2D cut through reciprocal space in L=0, 0.25, 0.5 and 0.75 planes showing 12-fold rings of ***a****/13 superlattice peaks. [Ref: David Voneshen, Private Communication].

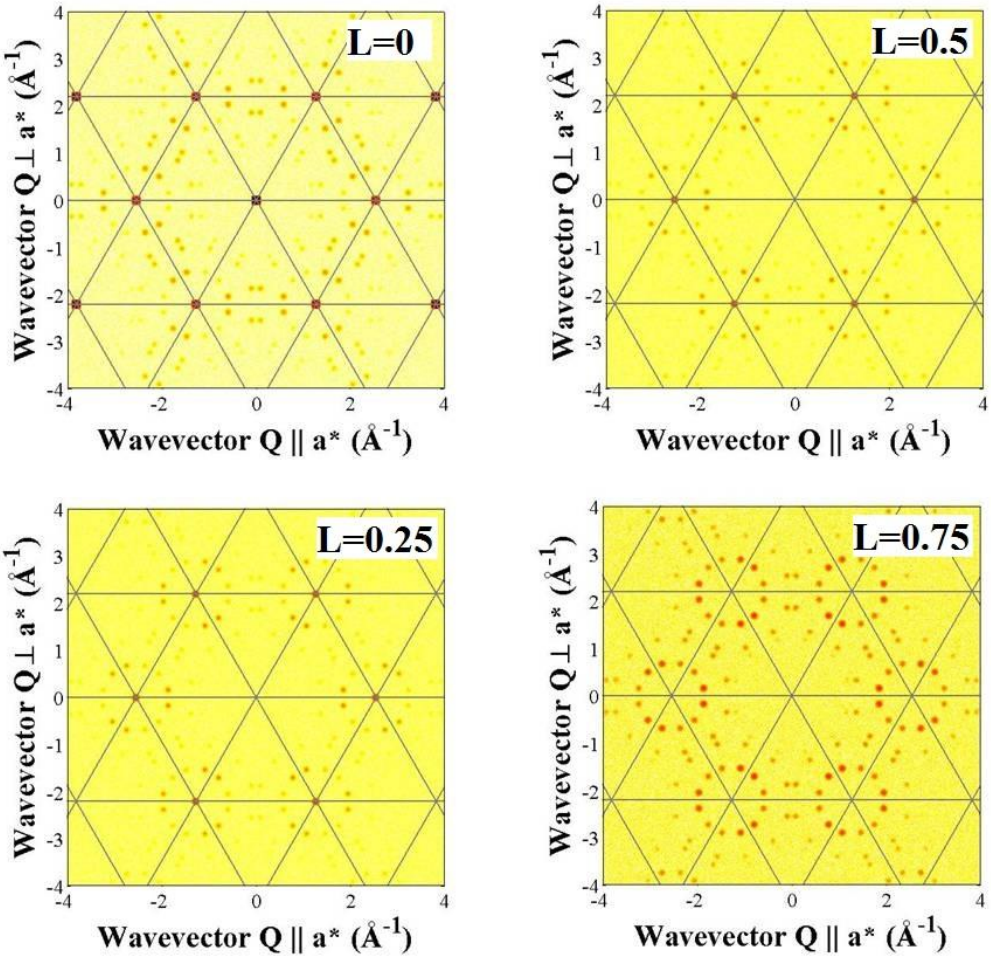

Figure 3.18: RMC Calculated intensity plot showing 1/13th superlattice phase for $Na_{0.77}CoO_2$ at L=0, 0.25, 0.5 and 0.75 planes. [Ref: David Voneshen, Private Communication].

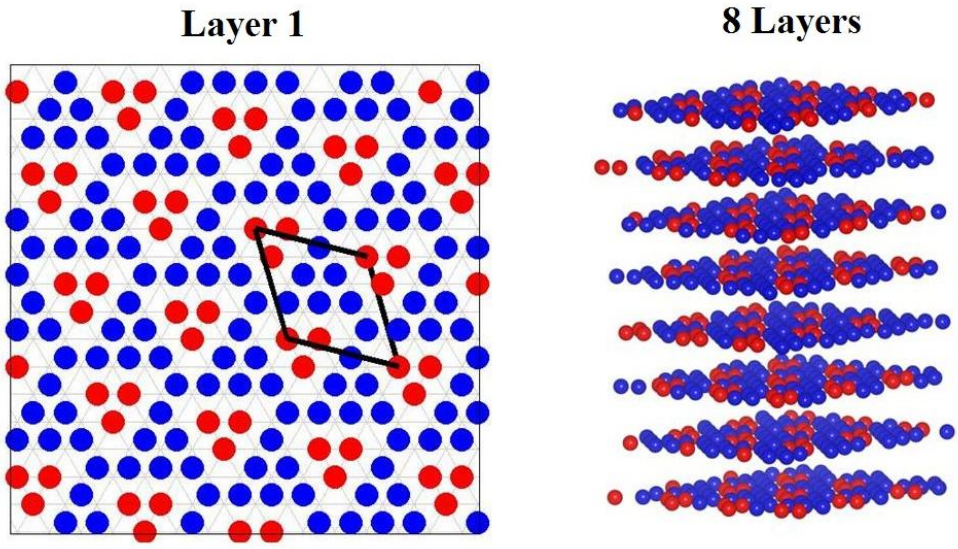

Figure 3.19: The structural model showing tri-vacancy clusters of Na1 atoms (red circles) in the in-plane on first layer and out-of-plane showing 8 layers in c-axis. Red spheres are Na1 atoms of tri-vacancy clusters and blue are the Na. [Ref: David Voneshen, Private Communication].

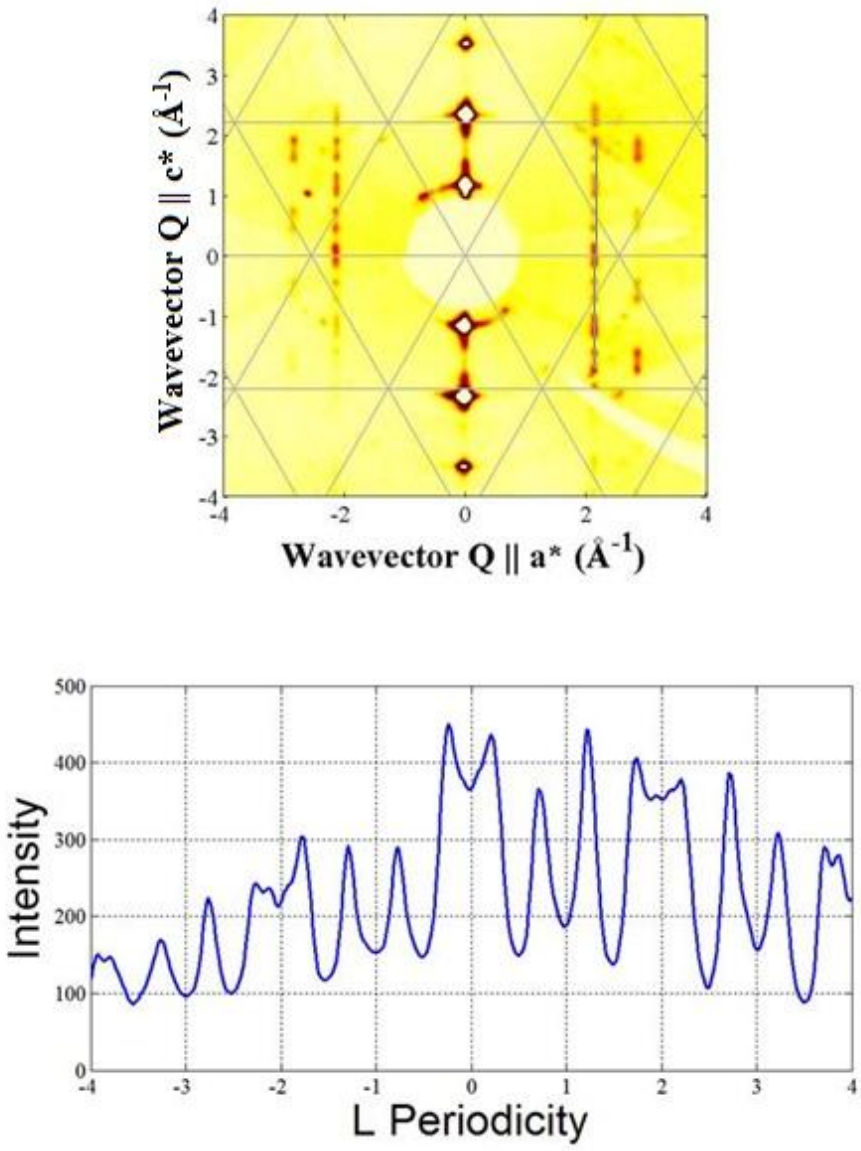

Figure 3.20: X-ray pattern for $Na_{0.77}CoO_2$ at T=300K showing 1/13th peaks in the L-direction indicated in the green line, where the peaks are arranged in 1/4th and 3/4th position in the L-dependence of the reciprocal space.

3.4.2.3 $Na_{0.71}CoO_2$

The superlattice reflections lie on a grid 1/7th the size of the hexagonal reciprocal lattice, see Fig 3.21. The L dependence of the scattering at room temperature is shown in Fig 3.23. There are strong peaks at L = integer values and much weaker scattering at L = 0.2 and 0.8. Assuming a superstructure based on the dominant reflections at integer L, the supercell is

$$\boldsymbol{a}' = 4\boldsymbol{a} + \boldsymbol{b}$$

$$\boldsymbol{b}' = 2\boldsymbol{a} + 4\boldsymbol{b}$$

$$\boldsymbol{c}' = \boldsymbol{c}$$

RMC calculations using the room-temperature data at integer L were performed for this cell, and the results are shown in Fig 3.22. The agreement with the experimental data in Fig 3.21 is good. The in-plane superstructure agrees with the prediction of DFT for x = 0.71 [53]. This superstructure is based on a zig-zag arrangement of di-vacancy clusters.

At lower temperatures the peaks still lie on the same in-plane superlattice, but the distribution of scattering along L changes. Fig 3.24 shows the L dependence at T = 150K. The peaks at integer L have disappeared and instead the scattering is mainly located at positions such as L = 0.2 and 0.8. Thus the stacking sequence of sodium planes has changed as a function of temperature.

At low temperatures the periodicity is ten sodium layers, and it is not yet possible to solve the superstructure for this layers supercell using RMC:

$$\boldsymbol{a}' = 4\boldsymbol{a} + \boldsymbol{b}$$

$$\boldsymbol{b}' = 2\boldsymbol{a} + 4\boldsymbol{b}$$

$$\boldsymbol{c}' = 5\boldsymbol{c}$$

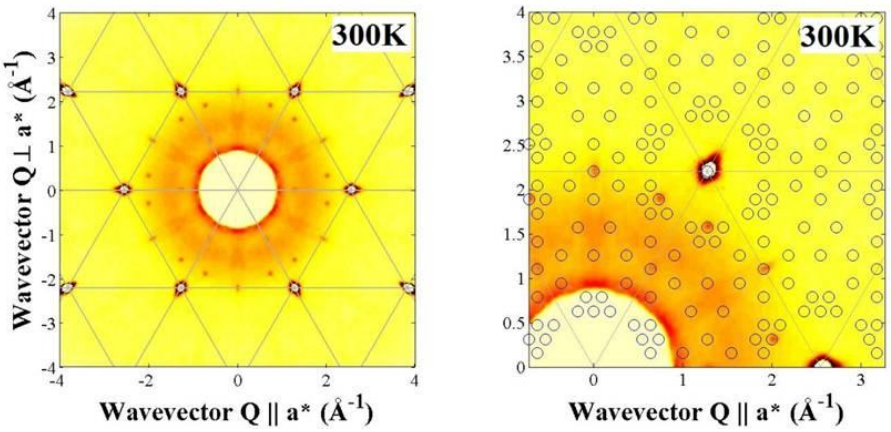

Figure 3.21: X-ray diffraction pattern of $Na_{0.71}CoO_2$ showing 2D cut through reciprocal space in (*h, k, 0*) plane at 300K. Circles indicate the peaks at 1/7th positions.

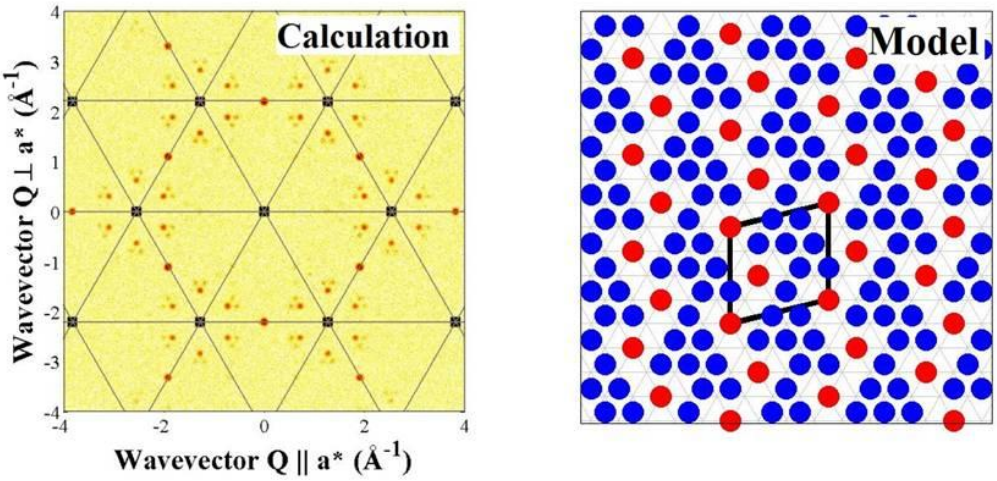

Figure 3.22: Calculated intensity from RMC show consistent result with the X-ray pattern showing 1/7th peaks at (*h, k, 0*). The structure model showing di-vacancy clusters of Na1 atoms (red circles) in the in-plane on layer 1. Red spheres are Na1 atoms of tri-vacancy clusters and blue are the Na2.

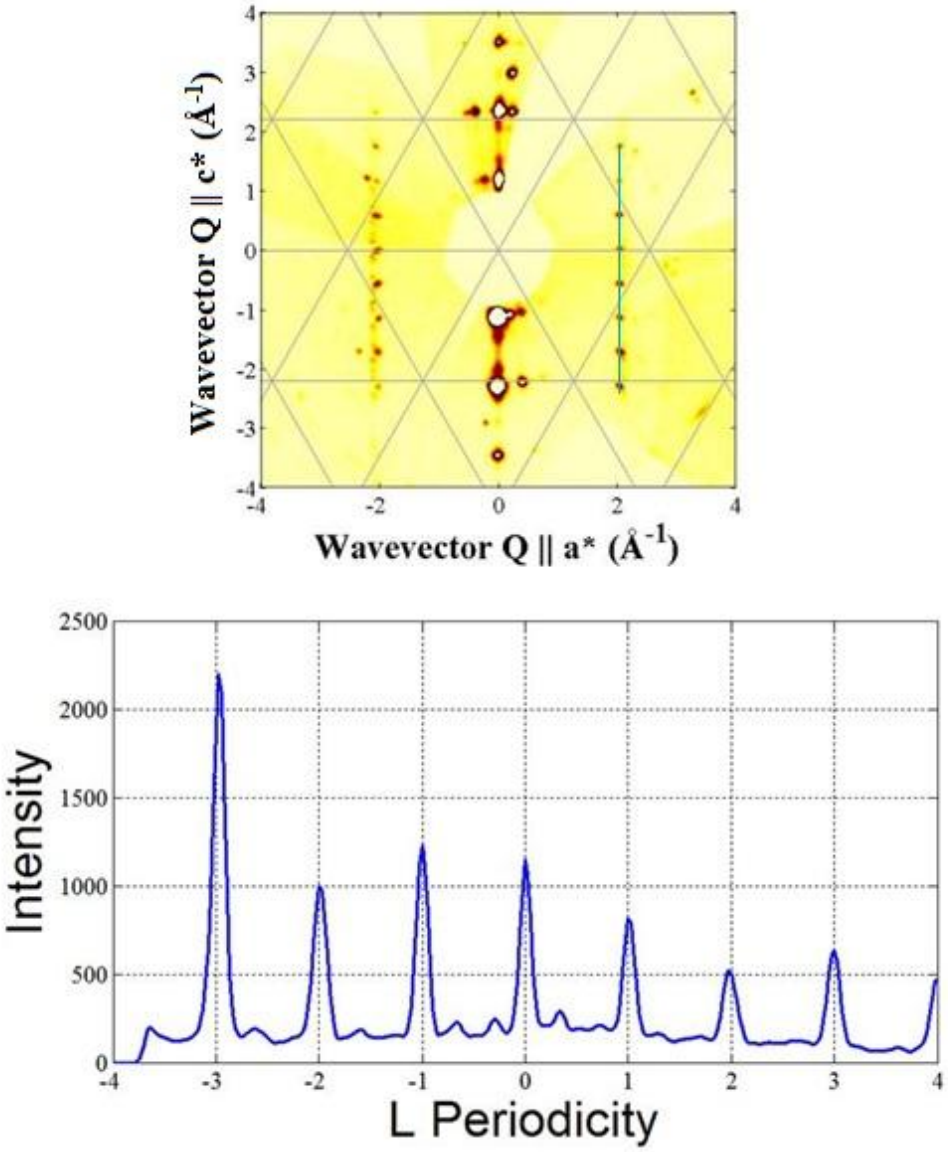

Figure 3.23: X-ray pattern for $Na_{0.71}CoO_2$ at T=300K showing 1/7th peaks in L-direction indicated in the green line. The 1/7th peaks arranged in integer of L-direction of the reciprocal space.

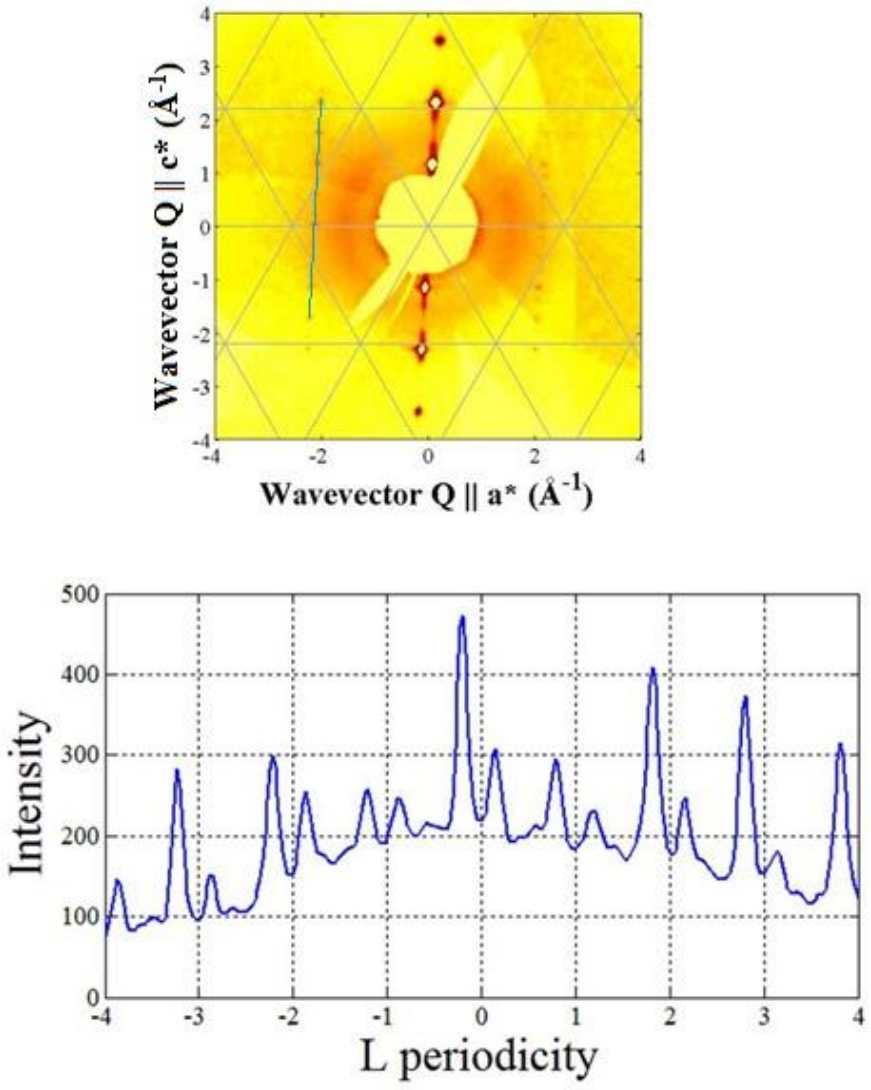

Figure 3.24: X-ray pattern for $Na_{0.71}CoO_2$ at T=150K showing 1/7th peaks in L-direction indicated in the green line. The 1/7th peaks arranged in L=0.2 and 0.8 in L-dependence in the reciprocal space.

3.4.2.4 $Na_{0.67}CoO_2$

The superlattice reflections for $Na_{0.67}CoO_2$ lie on a grid $1/6^{th}$ the size of the hexagonal reciprocal lattice, see Fig 3.25. the L dependence of the scattering presented in Fig 3.27 shows weak peaks at integer L and stronger peaks at L = 1/3, 2/3, etc. the superstructure comprises six layers of sodium, and the supercell is given by:

$$\boldsymbol{a}' = 4\boldsymbol{a} + 2\boldsymbol{b}$$

$$\boldsymbol{b}' = 2\boldsymbol{a} + 4\boldsymbol{b}$$

$$\boldsymbol{c}' = 3\boldsymbol{c}$$

A large zig-zag pattern of di-vacancy clusters is predicted by DFT [53], and a six sodium layer periodicity is predicted on the basis of ^{23}Na and ^{59}Co NMR and nuclear quadrupole resonance (NQR) studies [51], for this composition. This superstructure is shown in Fig 3.26, and the calculated scattering in Fig 3.25 is in good agreement with the experimental data.

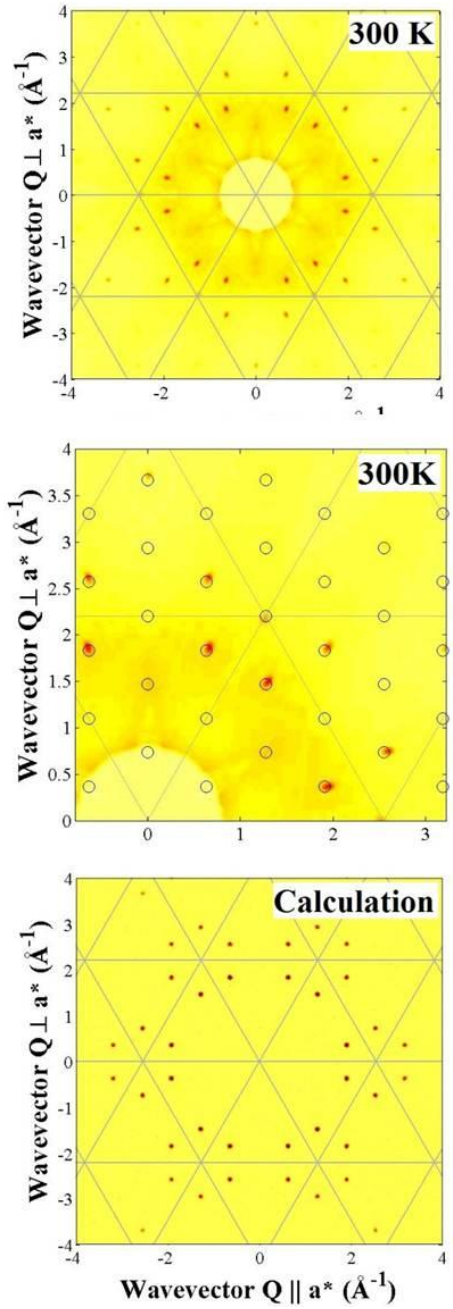

Figure 3.25: X-ray diffraction pattern of $Na_{0.67}CoO_2$ showing 2D cut through reciprocal space in (*h, k, 2/3*) plane at 100K. The circles on the peaks indicates the $1/6^{th}$ superlattice reflections and the calculated intensity is exactly positioned at L= 2/3.

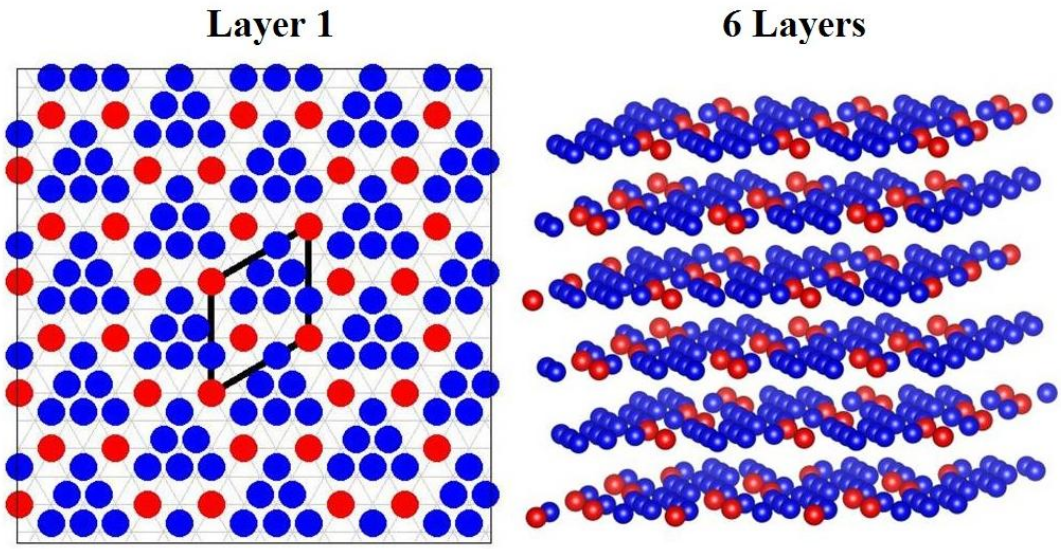

Figure 3.26: The structural model showing di-vacancy clusters of Na1 atoms (red circles) in the in-plane on first layer and out-of-plane showing 6 layers in c-axis. The Na1 atoms are indicated by red spheres of di-vacancy clusters and blue are the Na2.

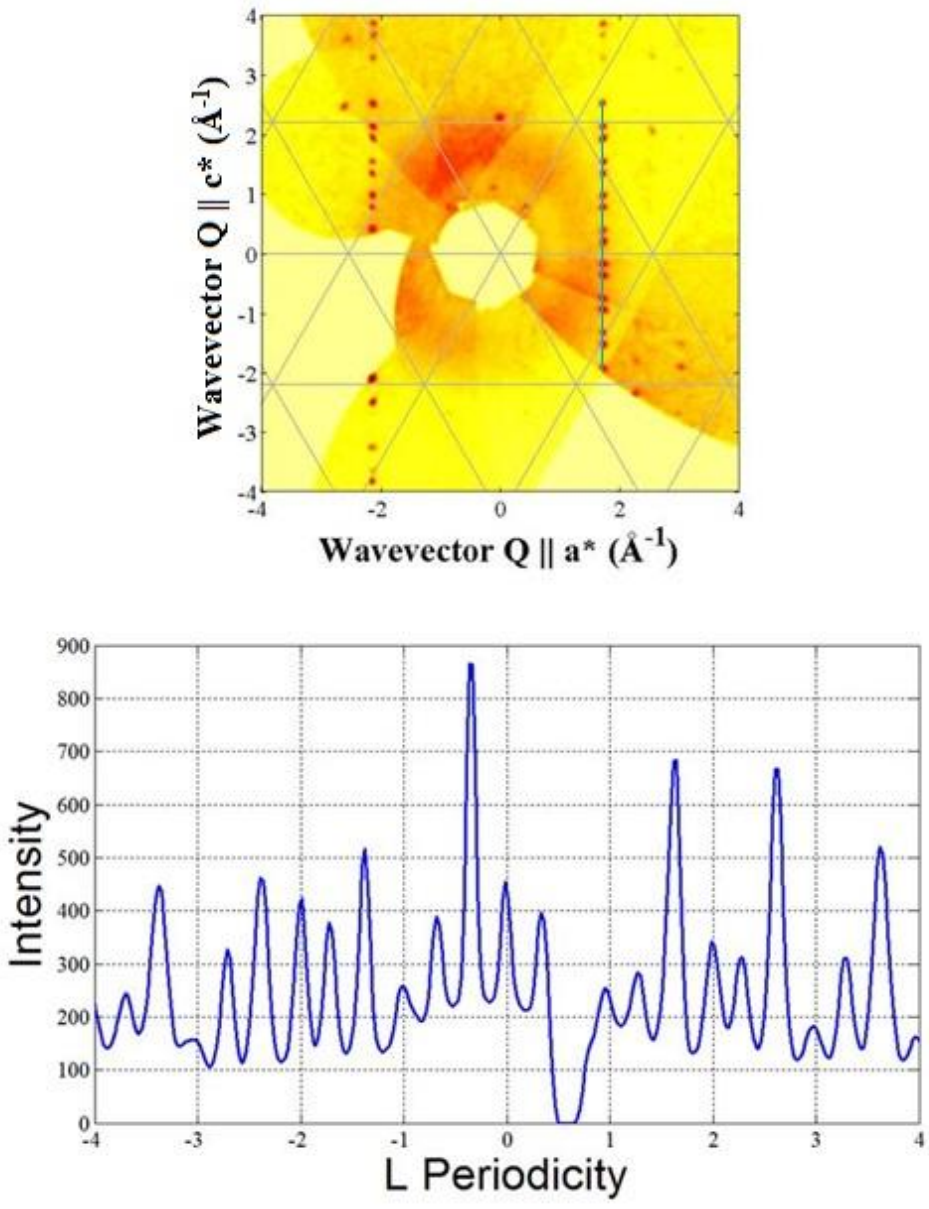

Figure 3.27: X-ray pattern for $Na_{0.67}CoO_2$ at T=300K showing 1/6th peaks arranged in 1/3rd, 2/3rd and integer planes in L-direction in the reciprocal space as indicated in the green line.

3.4.2.5 Na_xCoO_2 (x ~ 0.61−0.54)

For values of x below those where the $Na_{0.67}CoO_2$ superstructure is observed, the superlattice reflections were found to move continuously with further bromine de-intercalation. On the basis of the observed c-lattice parameter, this incommensurate phase was found to be stable over the range $0.54 < x < 0.61$. Figure 3.28 shows incommensurate peaks at several compositions and defines two modulation wave vectors. These modulation wave vectors are seen to vary monotonically within experimental uncertainty as a function of de-intercalation time, see Fig 3.29. The L dependence of the scattering is predominantly peaked at even integers (see Figure 3.30), indicating that the periodicity in the c-direction is only one sodium layer (half the hexagonal unit cell). Similar incommensurate superlattice reflections have previously been reported for Na_xCoO_2 for x ~ 0.53 [55].

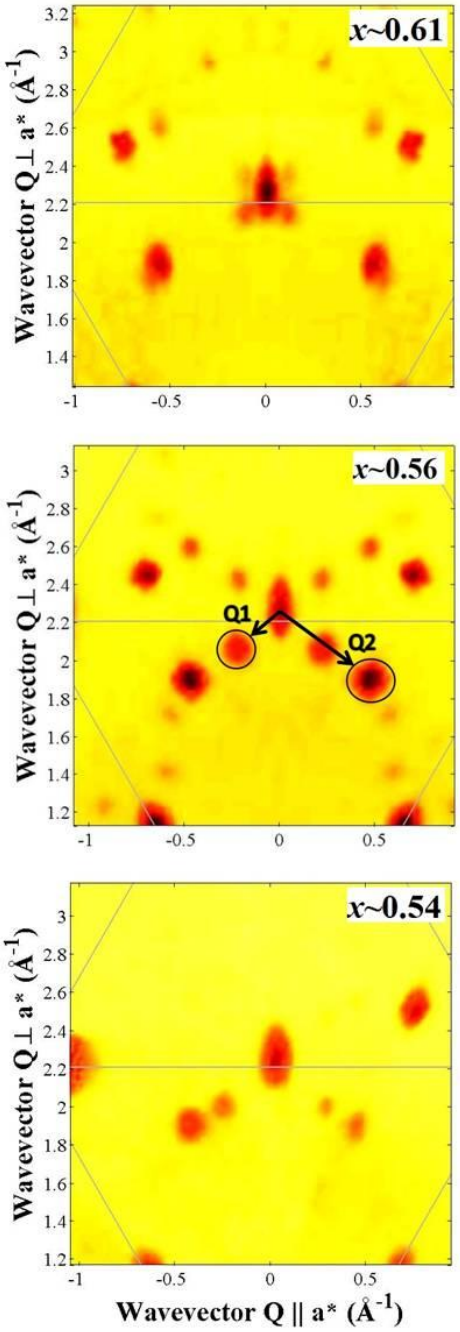

Figure 3.28: Movement of incommensurate superlattice peaks indicated in circles from x = 0.61 to 0.54, where Q1 and Q2 are the magnitude of two peaks at (*h, k, 0*).

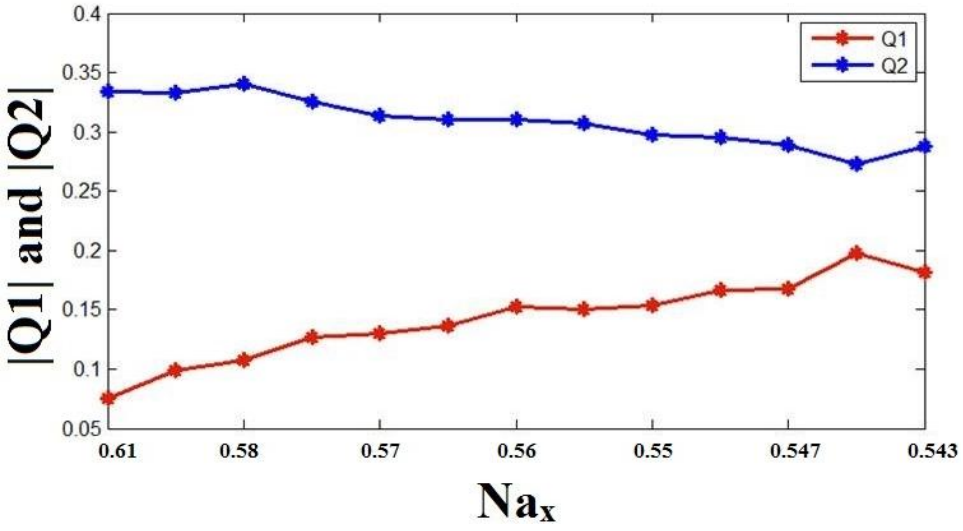

Figure 3.29: Movement of two different incommensurate peaks Q1 and Q2 of Na_xCoO_2, $0.61>x<0.54$.

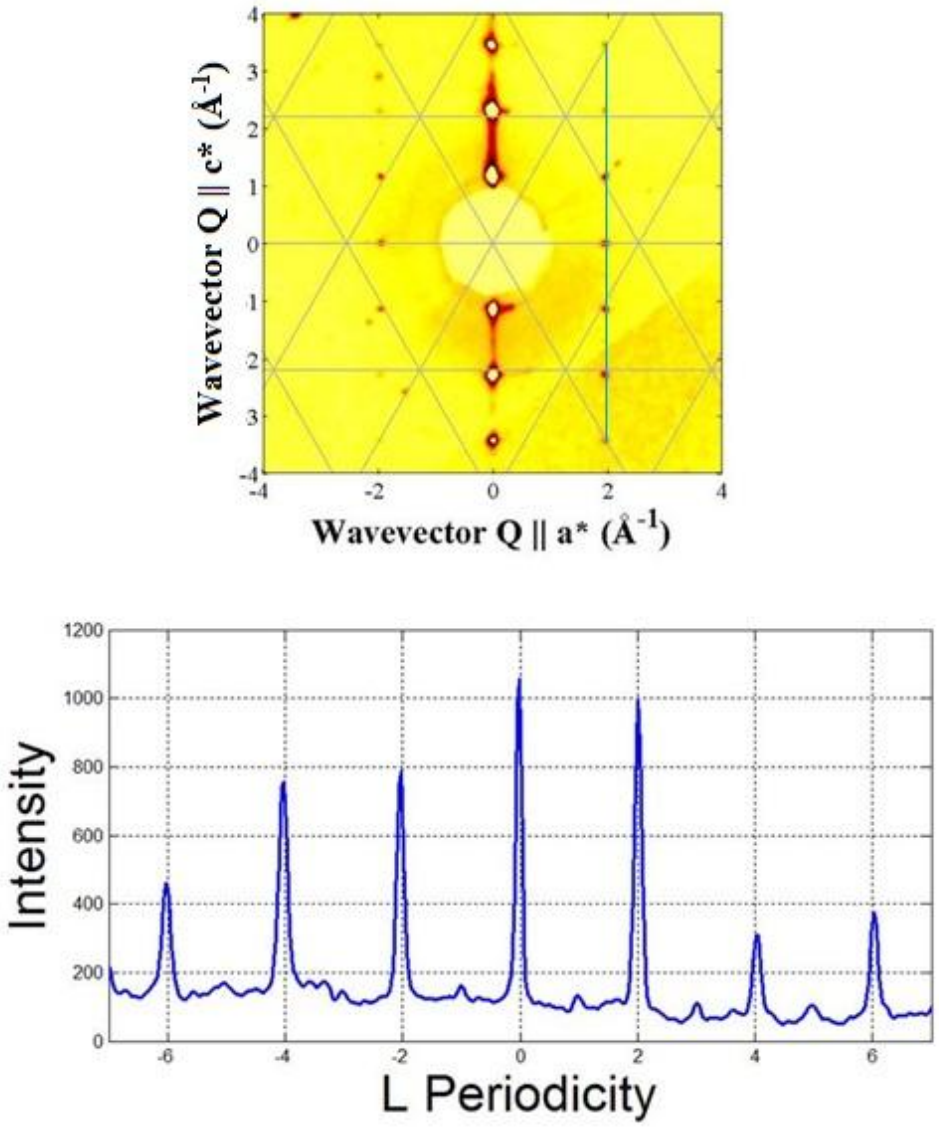

Figure 3.30: X-ray pattern for $Na_{0.56}CoO2$ at T=300K showing Q2 peaks only in even planes and a tiny leakage in odd planes of L-direction of the reciprocal space as indicated in the green line.

3.4.2.6 $Na_{0.5}CoO_2$

The XRD pattern observed at room temperature lies on a grid 1/4th the size of the hexagonal reciprocal lattice, see Fig 3.31. The L dependence of this scattering shown in Fig 3.33 is peaked at integer values. Hence the supercell agrees with that reported previously for $Na_{0.5}CoO_2$

$$\boldsymbol{a}' = 2\boldsymbol{a}$$

$$\boldsymbol{b}' = \boldsymbol{a} + 2\boldsymbol{b}$$

$$\boldsymbol{c}' = \boldsymbol{c}$$

RMC simulations were performed for these reflections and this cell and the results are presented in Fig 3.32. The agreement between the calculated intensities and the experimental data in Fig 3.31 is excellent. The alternating stripes of Na1 and Na2 ions can be interpreted as stripes of di-vacancy clusters.

At temperatures below T ~ 262K additional superlattice reflections appear. These new peaks lay on a commensurate grid 1/12th the size of the hexagonal reciprocal lattice, see Fig 3.31. These reflections are also peaked at integer L. Similar extra diffraction spots were observed by electron diffraction at low temperature [50]. These peaks could be from an additional modulation of the $Na_{0.5}CoO_2$ superstructure, or they could also be due to a coexistence of phases.

$Na_{0.5}CoO_2$ is a special composition, since it forms a charge ordered insulating phase at low temperature [35]. The electronic ordering will be investigated further in Chapter 5.

.

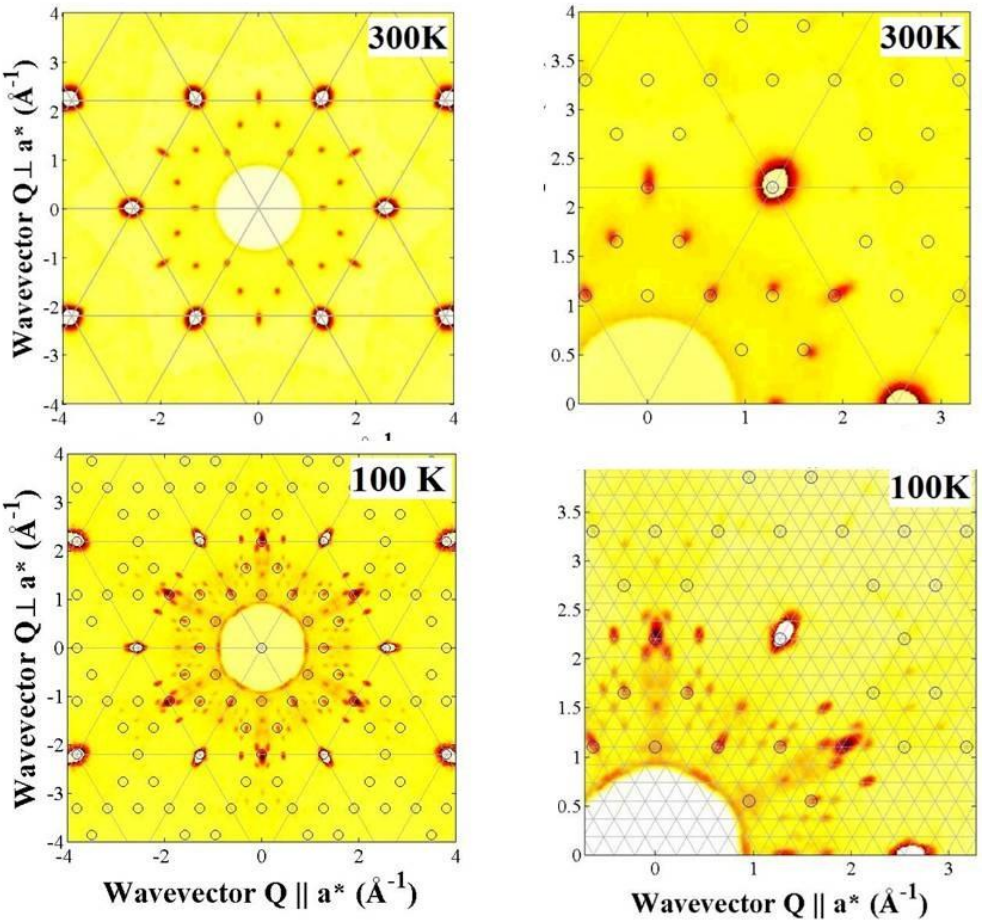

Figure 3.31: X-ray diffraction pattern of $Na_{0.5}CoO_2$ showing 2D cut through reciprocal space in (*h, k, 0*) plane. Circles indicate the peaks at 1/4th positions and extra superlattice reflections are the 1/12th peaks.

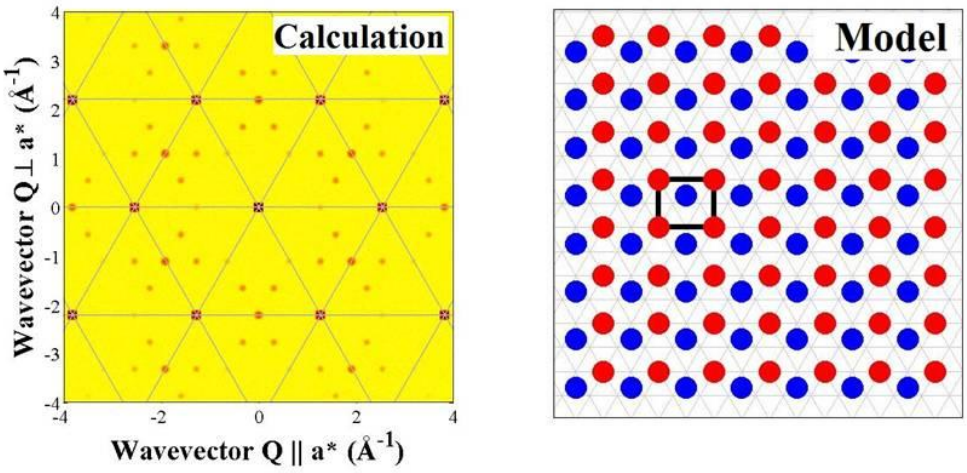

Figure 3.32: RMC intensity calculation and Structure model showing 1/4th superlattice phase for $Na_{0.5}CoO_2$ at (*h, k, 0*) at 300K. Red spheres are Na1 atoms of di-vacancy clusters and blue are the Na2.

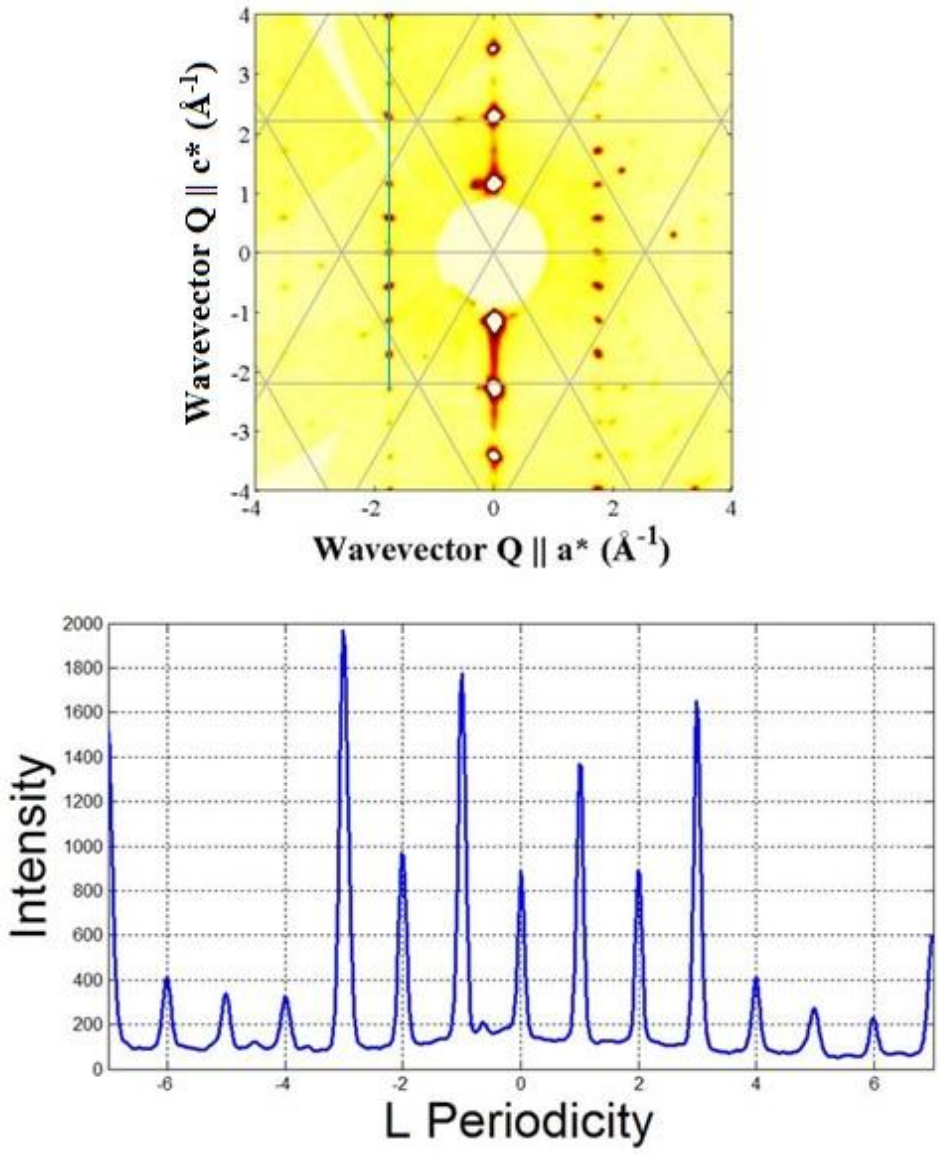

Figure 3.33: XRD pattern for $Na_{0.50}CoO2$ at T=300K showing 1/4th peaks arranged in integer position as indicated in the green line in L-direction of the reciprocal space.

3.4.3. Temperature dependence

The temperature dependence of the superlattice reflections of Na_xCoO_2, (x = 0.8, 0.77, 0.71, 0.67 and 0.5) was used to determine the reordering and disordering temperatures. These temperature dependencies were measured by XRD using a cryojet device to control the temperature of the sample precisely. The transformations of superlattice peaks were precisely observed with an X-ray exposure of 10 sec to cover the full reciprocal space over the temperature ranges 90K to 500K.

3.4.3.1. $Na_{0.8}CoO_2$

For x ~ 0.8, the 1/15th superlattice reflections were observed from 90K to 250K with temperature increased in 50K/min steps. Then, to study the disappearance of the strongest 1/15th superlattice peaks, 2K/min steps were maintained from 250 to 260K and 1K/min steps from 261K to 290K. The X-ray diffraction measurements were performed at each temperature step and a careful analysis has been made to obtain the reordering and disordering of the superlattice phases as a function of temperature. The temperature dependence of the ratio of superlattice to Bragg reflection is presented in Fig 3.34.

For T~286K, the intensity ratio of the 1/15th peaks starts to diminish and completely disappears by T~294K. The 1/5th superlattice reflections start rising at T~292K, and the co-existence of two superlattice peaks (1/15th and 15th peaks) is observed between 292K and 294K (indicated by the yellow region). The 1/5th peaks infer the presence of the disordered striped phase. These phase drop sharply in intensity at T~375K, and they broaden in wave-vector transfer to become diffuse at T~400K.

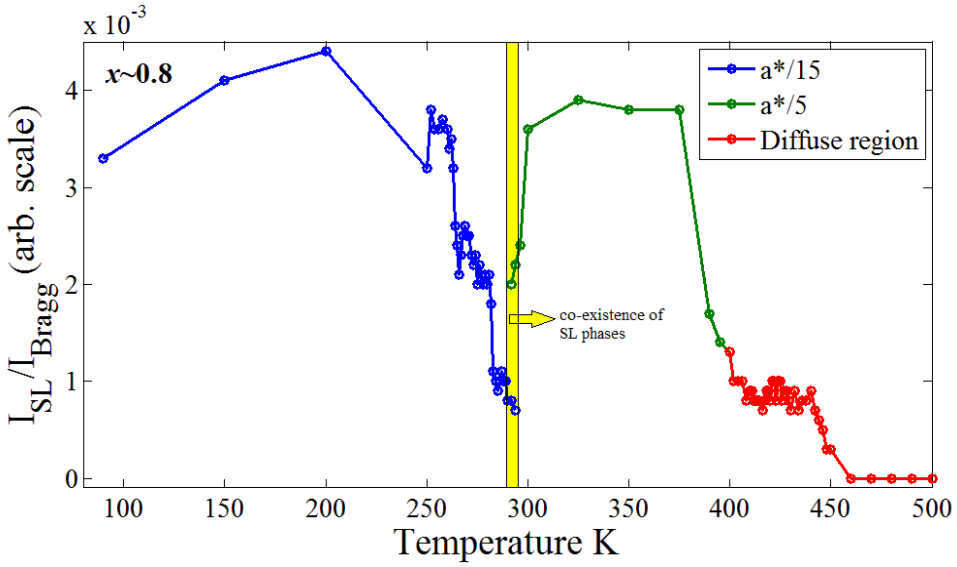

Figure 3.34: Temperature dependence plot for $Na_{0.8}CoO_2$.Blue line showing ***a****/15 peaks, green the ***a****/5 and red the diffuse region. The co-existence of ***a****/15 and ***a****/5 superlattice phase is indicated in the yellow region between T=292K and 294K.

For the high temperature measurements, 2K/min steps were maintained from 400K to 410K, and then 1K/min steps were maintained from 411K to 430K. At T~395K, both $1/5^{th}$ superlattice reflections and the rings of diffuse scattering were observed. By T~408K, the $1/5^{th}$ peaks had completely disappeared and only broadened diffuse peaks were observed. After that, 2K/min steps were maintained from 430 to 450K. A complete disappearance of the diffuse scattering was observed at T~460K. For the temperature range 460 to 500K, there was no evidence of superlattice reflections or diffuse scattering.

3.4.3.2. $Na_{0.77}CoO_2$

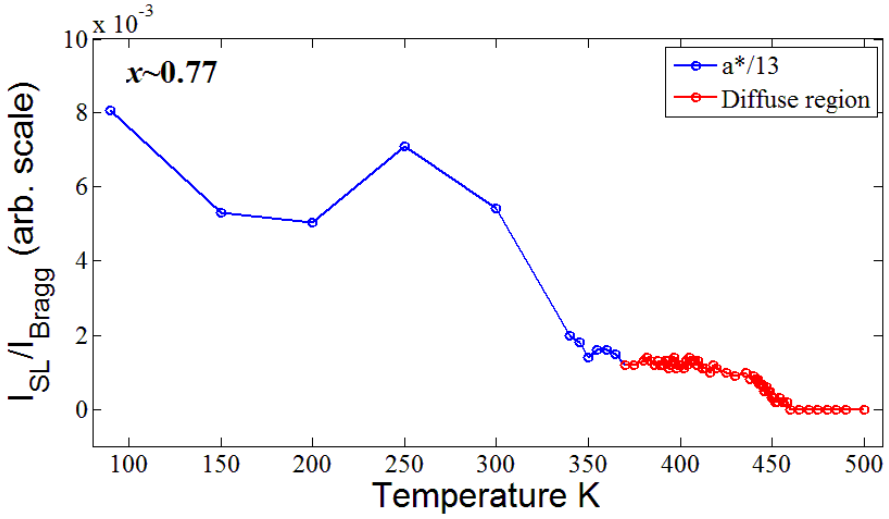

Figure 3.35: Temperature dependence plot for $Na_{0.77}CoO_2$. Blue line show ***a****/13 peaks and red the diffuse region.

For x~0.77, over the range between 90 and 340K the temperature was increased in 50K/min steps. To observe the disappearance of strong superlattice reflections and to observe the diffuse scattering, the temperature increased in 5K/min steps over the temperature range 340 to 380K. In this temperature range, sharp 1/13th superlattice reflections were observed up to T~370K. By T~375K, the 1/13th superlattice peaks disappeared and broadened diffuse rings around the principal Bragg reflections was observed (see Fig 3.35). Evidence for diffuse scattering above T~373K for this composition was previously reported on the basis of data obtained using synchrotron X-rays [52]. These diffuse rings are indistinguishable for those obtained from the $Na_{0.8}CoO_2$ system. However, the ordering temperatures for both the systems are different.

3.4.3.3. $Na_{0.71}CoO_2$

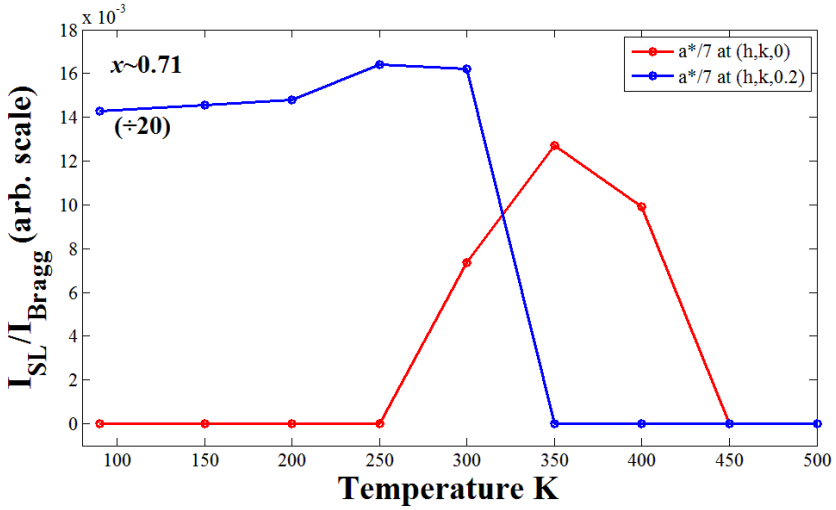

Figure 3.36: Temperature dependence plot of $Na_{0.71}CoO_2$ showing blue line corresponds to ***a****/7 peaks at L=0.2 plane and the red line corresponds to ***a****/7 peaks at integer L planes.

The temperature dependence of the superlattice reflections from $Na_{0.71}CoO_2$ is shown in Fig 3.36. The fact that the superlattice peaks lie on a $1/7^{th}$ grid does not change below T~450K, but the distribution of intensity along the L direction changes dramatically in the vicinity of room temperature. The dominant $1/7^{th}$ superlattice peaks were observed in the integer L planes over the temperature above 300K. These peaks disappeared at temperatures below 300K, where peaks on the same grid were observed intermediately between the integer L planes on each of the L = 0.2 and 0.8 positions (see figures 3.23 and 3.24). In the vicinity of room temperature, both types of superlattice reflections coexist. There is a change the periodicity from two to ten sodium layers below room temperature. At present we are unable to explain this unusual phase transition.

3.4.3.4. $Na_{0.67}CoO_2$

For x ~ 0.67, the intensity ratio of the 1/6th superlattice peaks were observed at 1/3rd and 2/3rd positions in L-direction relative to that of the Bragg reflections was measured from 90 to 450K with the temperature increased in 50K/min rate. The data in Fig 3.37 show that the intensities of the superlattice reflections increased above 200K and then decreased after 450K. The 1/6th superlattice reflections disappeared completely by 500K. The diffuse scattering was not observed over any temperature range for x ~ 0.67.

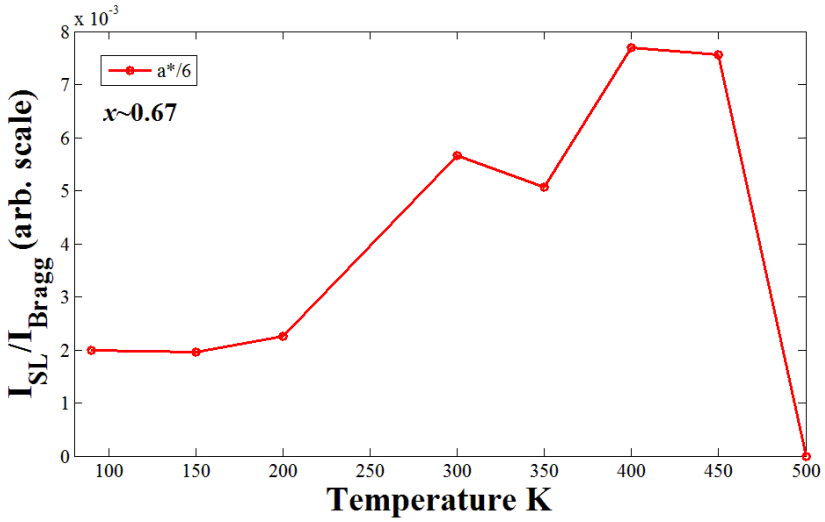

Figure 3.37: $Na_{0.67}CoO_2$ Temperature dependence plot showing 1/6th peaks and disappearance at 500K.

3.4.3.5. $Na_{0.5}CoO_2$

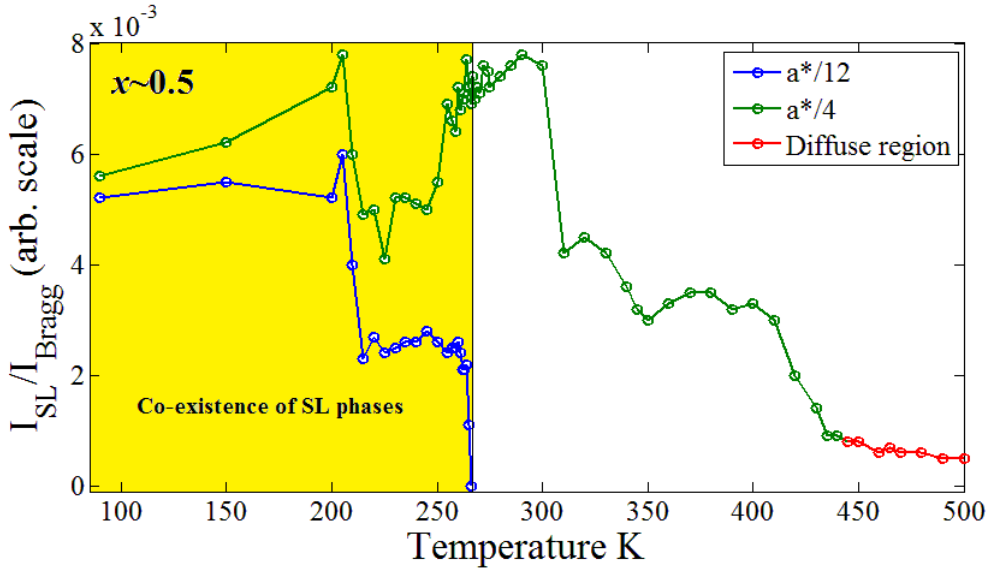

Figure 3.38: Temperature dependence plot for $Na_{0.5}CoO_2$. Blue line showing the ***a****/12 peaks, green the ***a****/4 peaks and red the diffuse region. The co-existence of superlattice phases is indicated in the yellow region.

Figure 3.38 shows the temperature dependence of the 1/4th and 1/12th superlattice reflections in $Na_{0.5}CoO_2$. The 1/12th reflections disappear at T = 265K. Below this temperature the 1/12th peaks coexist with 1/4th peaks, and the temperature dependence of the intensities appear to be correlated. Above T = 265K, only the 1/4th reflections observed, and these sharp superlattice peaks disappear at T = 435K. Above this temperature up to the highest temperature attainable, T = 500K, a different type of diffuse scattering is observed.

3.4.4 Diffuse scattering

A perfect, long range ordered superstructure gives rise to elastic, resolution-limited scattering at the superlattice and Bragg reflections. Any departures from the ideal superlattice will lead to diffuse scattering elsewhere in reciprocal space. This could be due to either static defects, or to thermal diffuse scattering. The width in $\boldsymbol{Q}$ of the diffuse scattering indicates the size of the defects of the short-range ordered regions.

3.4.4.1 $Na_{0.8}CoO_2$

Above T~400K there are no sharp superlattice reflections. Figure 3.39 shows the rings of diffuse scattering around hexagonal reciprocal lattice points. These are crescent shaped and the maximum of intensity are in <110> directions rather than the <100> directions of the precursor superstructure. Hence, they are not caused simply by the breakup of the superstructure into smaller domains, the different $\boldsymbol{Q}$ dependence reveals different correlations.

The L dependence of the diffuse scattering is shown in Fig 3.40. The broad scattering peaked at integer L shows that the short-range order is correlated over a few atomic planes of sodium.

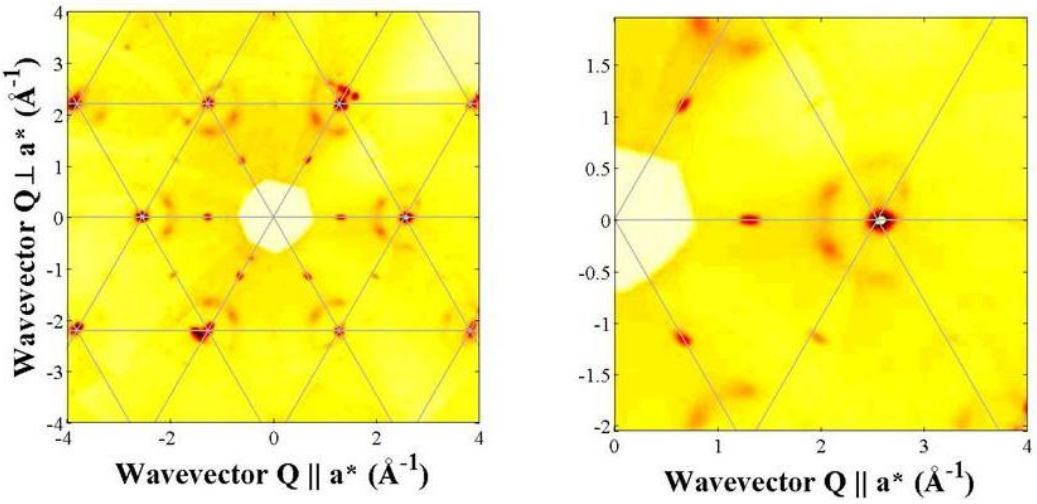

Figure 3.39: Rings of diffuse scattering around the main Bragg reflections for $Na_{0.8}CoO_2$ at (*h, k, 1*) at T=410K.

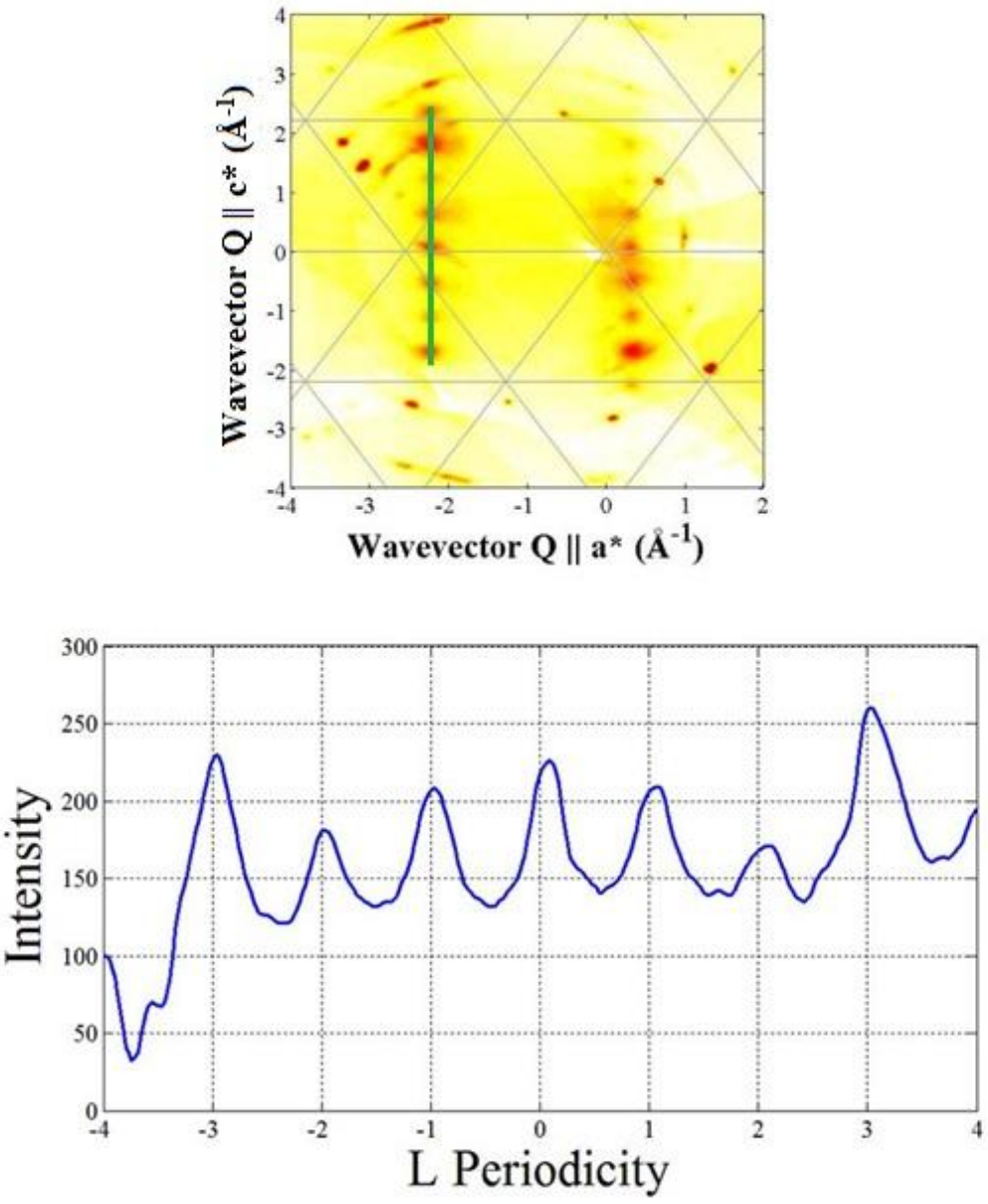

Figure 3.40: L dependence of the diffuse peaks for $Na_{0.8}CoO_2$ indicated in the green line, showing individual diffuse peaks in integer positions of L planes.

3.4.4.1.1 Monte Carlo calculations for $Na_{0.8}CoO_2$

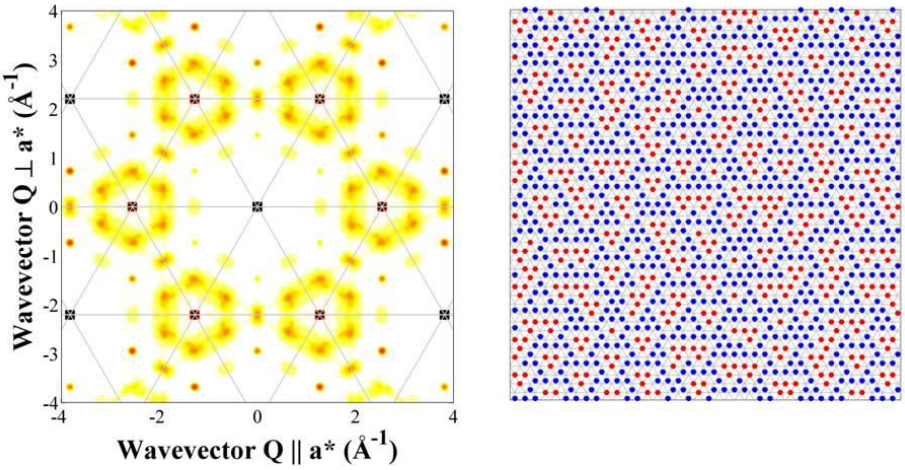

Figure 3.41: Monte Carlo calculations of diffuse rings in $Na_{0.8}CoO_2$ at (*h, k, 1*). [Ref: Michel Roger, Private Communication].

Previously, in this chapter, we have used the Reverse Monte Carlo method to solve the crystal structures of Na_xCoO_2 for the long range ordered sodium ions. However, we need a stochastic approach such as Monte Carlo methods, to obtain a solution for the short range ordered system. This provides an effective way to solve multi dimensional integrals to calculate the electrostatic energy of the system. Temperature sweeps give long range ordering of identical clusters at simple fractional fillings. However, at T~400K, above the ordering temperature, the calculation gives a mixture of di-, tri- and quadric- vacancy clusters that only order short-range [10].

Figure 3.41 shows the calculated intensity cut off at (*h, k, 1*) showing the diffuse scattering around the Bragg reflections and their corresponding structure model consists of multi-vacancy clusters (di-, tri-, and quadri-vacancies) with only short range order. This calculated result is in excellent agreement with the experimental diffuse scattering in Fig 3.39.

Furthermore, one might expect multi-vacancy clusters in the adjacent sodium layers to avoid occupation of the same regions due to Coulomb repulsion, and this will lead to some coherence over a few sodium layers. Hence, the diffuse scattering for $Na_{0.8}CoO_2$ solved using Monte Carlo calculations by Prof. M. Roger, CEA Saclay, France, agrees remarkably well with the experimental data. [Private Communication]

3.4.4.2 $Na_{0.77}CoO_2$

Quantitatively similar diffuse scattering was measured for $Na_{0.77}CoO_2$ as $Na_{0.8}CoO_2$ at high temperatures. However, the diffuse scattering appears at the lower temperature T~375K. The diffuse scattering measured for $x \sim 0.77$ in-plane and out-of-plane were indistinguishable to $Na_{0.8}CoO_2$. This seems reasonable since short-range ordering of the different multi-vacancy clusters is unlikely to be very sensitive to composition x. The diffuse scattering had completely disappeared at 460K.

3.4.4.3 $Na_{0.5}CoO_2$

The diffuse scattering for $Na_{0.5}CoO_2$ measured at T = 450K is very different from the diffuse scattering measured at high x, see Fig 3.42. The diffuse scattering is centred on the same $1/4^{th}$ positions as the superlattice peaks, indicating that the scattering arises from departures from the ideal striped superstructure in Fig 3.32. The L dependence of the diffuse scattering is also completely different, see Fig 3.43. The rods of diffuse scattering along the L direction show that the correlations are confined to single sodium layer.

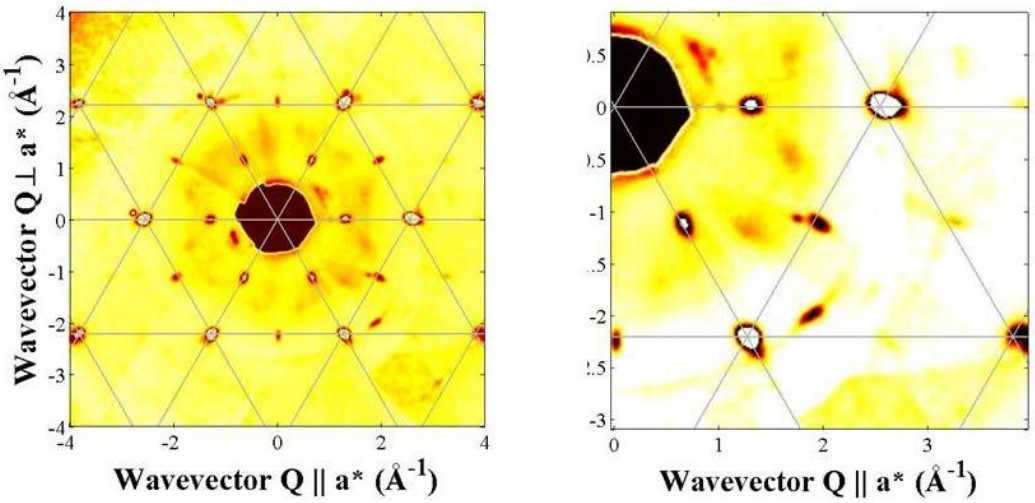

Figure 3.42: Diffuse scattering for $Na_{0.5}CoO_2$ showing weak and broadened diffuse peaks at (*h, k, 0*) plane at 450K

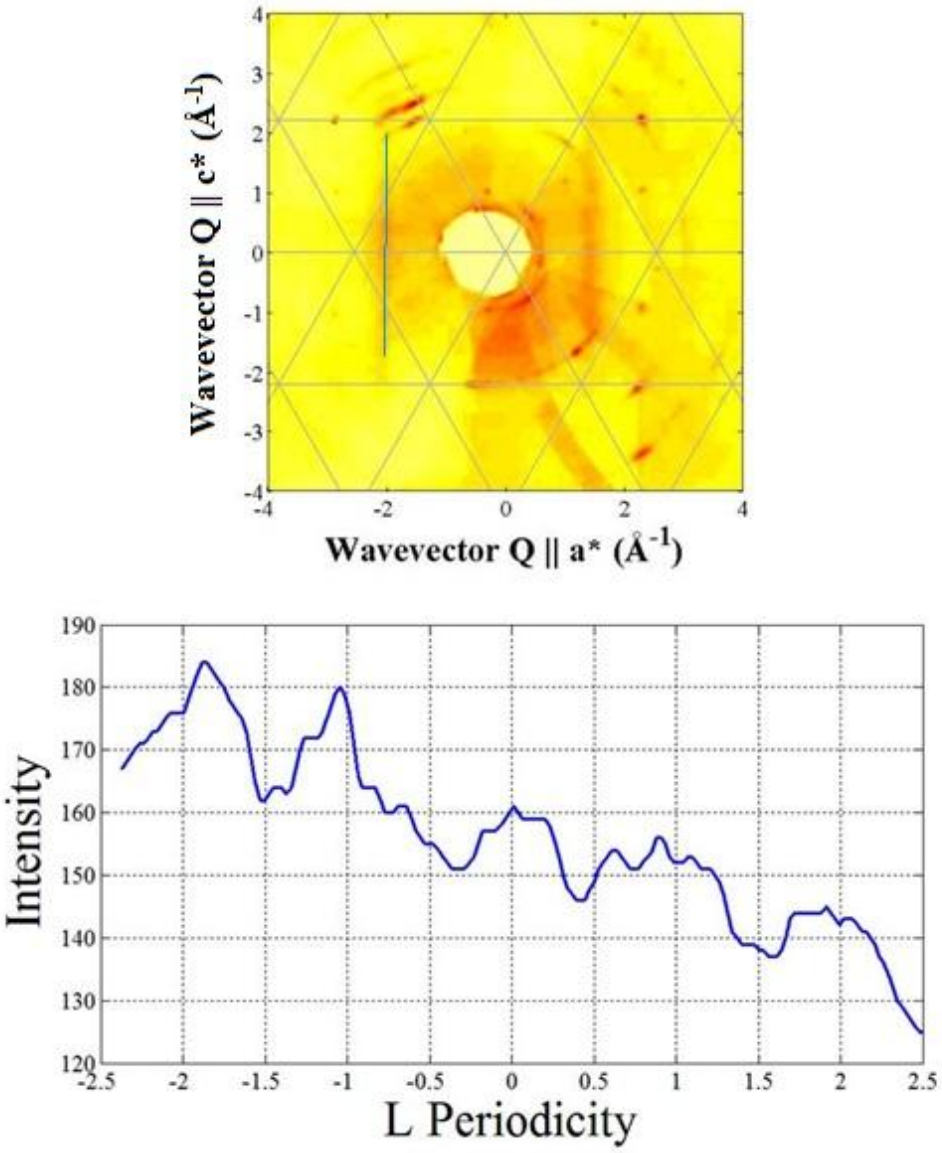

Figure 3.43: L dependence of the diffuse scattering for $Na_{0.5}CoO_2$ showing diffuse rod like appearance in the plane perpendicular to L direction in the reciprocal space as indicated in the green line.

3.4.5 Surface structure

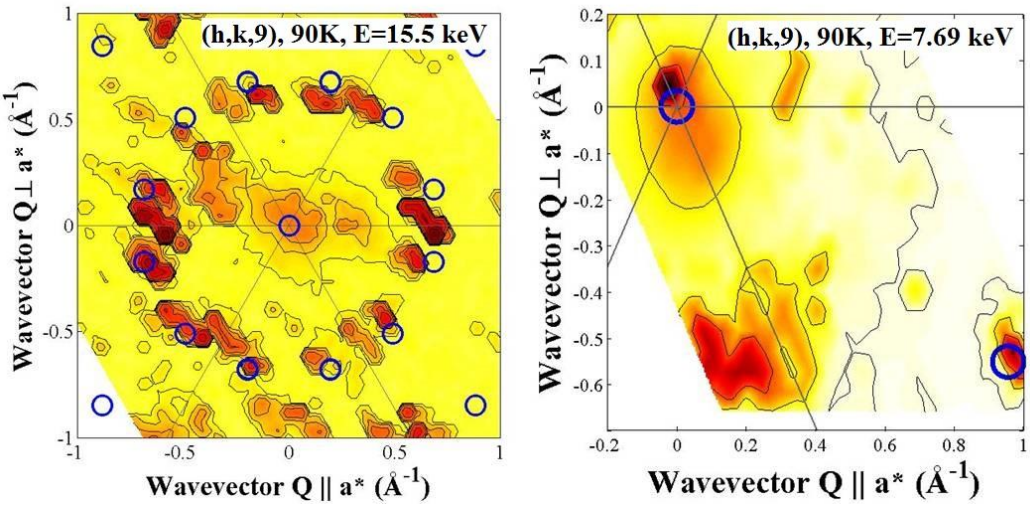

Figure 3.44: Existence of 1/15th superlattice peaks in the bulk phase with E=15.5KeV and 1/4th peaks in surface with E=7.69KeV for $Na_{0.8}CoO_2$ at (*h, k, 9*). Superlattice peak positions are indicated in blue circles.

To compare the surface and bulk phase structure of sodium cobaltate, the single crystal of $Na_{0.8}CoO_2$ was measured using synchrotron X-ray diffraction measurements on the I-16 beam line at Diamond Light Source. The diffraction patterns were scanned for two different energies at T = 90K. The superlattice reflections were indexed on a commensurate grid of size 1/15th of the reciprocal unit length with X-ray energy E = 15.5 keV, as shown in figure 3.44. Then the energy was changed to E = 7.69 keV to measure the superlattice reflections in the same sample, and it shows only the 1/4th peaks. Hence, the superlattice reflections observed at higher energy were not observed when low energy X-rays were used. The lower energy X-rays are less penetrating, and it was concluded that the data showing 1/4th superlattice reflections corresponds to a surface phase and are not from the bulk. All of the X-ray patterns reported previously in this

chapter were obtained with X-ray energy E = 17.5 keV and, therefore, they constitute bulk measurements.

3.5 Conclusion

By gradually removing sodium through bromine de-intercalation, the superlattice phase diagram was determined as a function of sodium concentration over the range $0.32 < x < 0.85$. In cases where the supercell comprises two sodium layers, it was possible to solve the superstructures using Reverse Monte Carlo methods. The in-plane sodium superstructures are consistent with the predictions of first principles calculations using DFT. In some cases we determined superstructures comprising more than two sodium layers.

For each phase the temperature dependence was measured over the range $90 < T < 500K$. In the case of $Na_{0.8}CoO_2$, the superstructure at base temperature was found to depend upon cooling rate. Quenching lead to a striped array of tri-vacancy clusters, whereas slow cooling lead to what is presumably the ground state – a square array of tri-vacancy clusters. A disordered stripe phase is observed at intermediate temperatures, and the ordered stripe phase is presumably a meta-stable state. For $Na_{0.71}CoO_2$ there is a change in the stacking of sodium layers in the vicinity of room temperature, and for $Na_{0.5}CoO_2$ additional superlattice reflections are observed at low temperature. Over the composition range $0.54 < x < 0.61$ incommensurate superstructures were found.

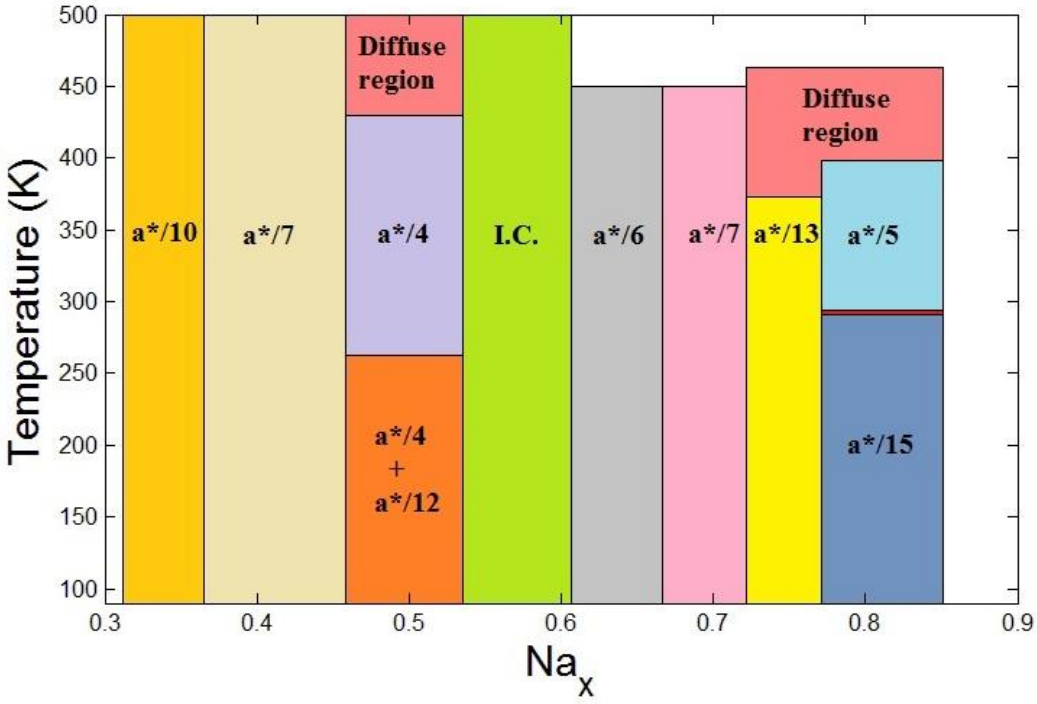

Figure 3.45: Phase diagram of Na_xCoO_2, (x ~ 0.85−0.319), showing a variety of superlattice phases and diffuse regions as a function of sodium content

In some cases diffuse scattering was observed above the ordering temperature. For high x, Monte Carlo simulations show that the scattering arises from short-range ordering of different multi-vacancy clusters. There is some coherence between planes, since multi-vacancy clusters try to avoid each other in successive sodium layers, in order to minimise the Coulomb energy. A different type of diffuse scattering is observed for x = 0.5, arising from small regions of the in-plane superstructure for this composition, with no correlations between planes. The temperature - concentration phase diagram is summarised in Fig 3.45. Using X-rays of lower energy, it was possible to focus on the near - surface region. For a sample with the bulk x = 0.8 superstructure, de-intercalation of sodium was found to lead the x = 0.5 superstructure at the surface.

Chapter 4

Physical Properties

4.1 Abstract

The aim of this chapter is to relate the thermoelectric and magnetic properties of Na_xCoO_2 to their superstructures. The samples were prepared using the de-intercalation techniques described in the previous chapter, and their superstructures were determined using X-ray diffraction at Royal Holloway. Thermoelectric properties were measured using the Physical Property Measurement System (PPMS) at Royal Holloway and the magnetic properties were measured using the Superconducting Quantum Interference Device/Vibrating Sample Magnetometer (SQUID/VSM) at the Diamond Light Source. The observed thermoelectric properties were comparable to the best reported previously in the literature and a high figure-of-merit was obtained at high x. Significant improvements in all of the thermoelectric properties coincided with the change from di-vacancy to tri-vacancy clusters. All samples with tri-vacancy clusters order antiferromagnetically at T_N~20K, whereas those comprising di-vacancy clusters do not order down to 2K.

4.2 Background

The patterning of sodium ions in sodium is expected to affect the thermoelectric properties and magnetic properties via its effect on the electronic state of the CoO_2 layers and the lattice vibrations [37].

An enhanced thermopower was obtained for different *x,* as reported previously by many authors [56-58], (see figures 4.1 and 4.2). Terasaki *et al*. reported that the thermopower for the polycrystalline $Na_{0.5}CoO_2$ increases monotonically towards the room temperature with no intermediate peaks between 5 and 300K [1], as shown in figure 4.1 (a). The Seebeck coefficients for single crystals of $x \approx 0.71$, 0.75, 0.80, 0.85, 0.88, 0.89, 0.96, 0.97 and 0.99, were reported by Lee et al [56], as shown in figure 4.1 (b). The in-plane thermopower rises steeply in the low temperature region, but in this case it peaks near 130K. A maximum room temperature thermopower was observed for high $x \geq 0.80$ lying between 150 and 250μVK^{-1}.

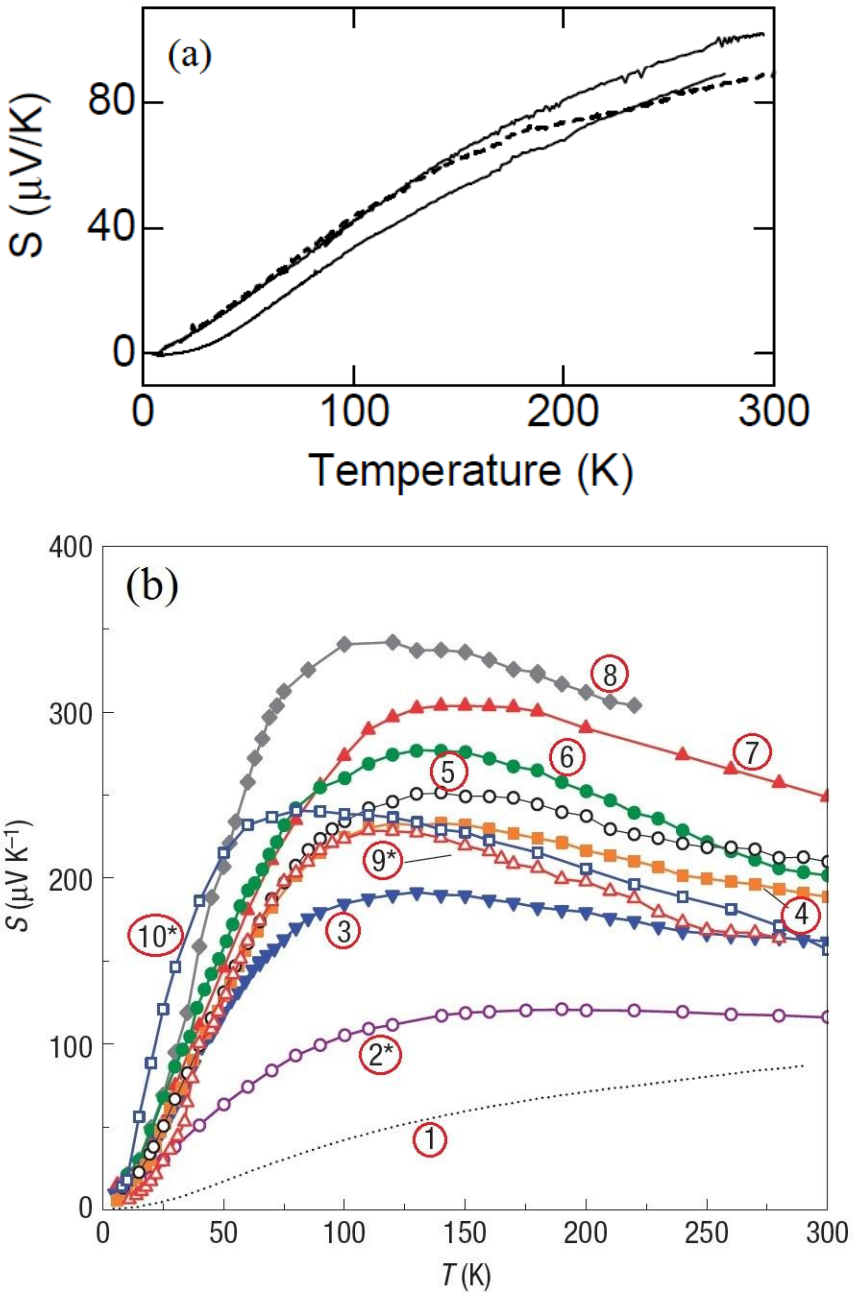

Figure 4.1: (a) Seebeck coefficient of $Na_{0.5}CoO_2$ by Terasaki *et al.* Ref.: [1]. (b) Seebeck coefficient of $0.75 < x < 1.0$, arranged in ordered of increasing x. The numbers 1-9* in red circles corresponds to 1 (x=0.71), 2 (x=0.75), 3 (x=0.80), 4 (x =0.85), 5 (x =0.88), 6 (x=0.89), 7 (x =0.96), 8 (x =0.97) and 9* (x=0.99), respectively, the asterisks indicate the three layer system by Lee *et al.* Ref.: [56].

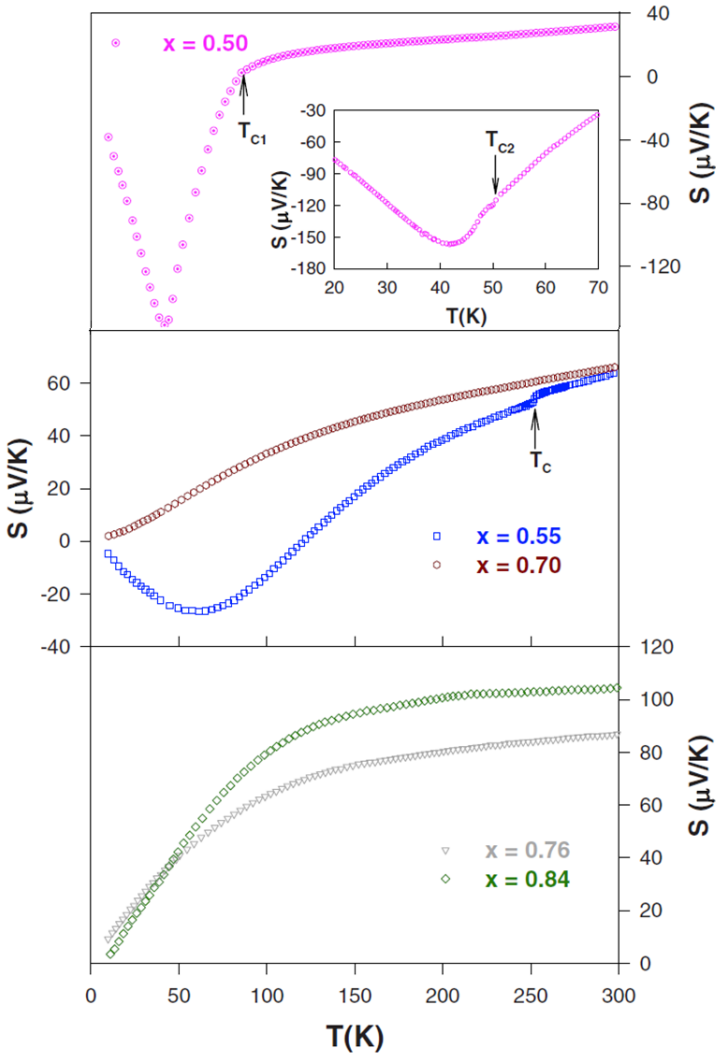

Figure 4.2: Seebeck coefficient as a function of temperature with x = 0.50, 0.55, 0.70, 0.75 and 0.84, Ref.[58].

Kaurav *et al.* described the thermopower for single crystals over a wide range of x = 0.5, 0.55, 0.70, 0.76 and 0.84, as shown in figure 4.2, where the Seebeck coefficient '*S*' lies in the range 30-100 μV/K, increasing with increasing x. However, there is a sign change in the temperature dependent Seebeck coefficient for x = 0.5 and 0.55, where S starts with negative value

in the low temperature region and crosses over to a positive regime at higher temperatures. This kind of reversal in sign is attributed to a substantial change in the band structure or the conduction mechanism of the dominant charge carriers [58].

For $x = 0.5$, a distinct negative peak appears around 50K at the temperature where charge ordering occurs and it becomes positive around 85K where antiferromagnetic ordering is observed. For higher concentrations $x \geq 0.7$, the thermopower increases monotonically with increasing temperature to the room temperature. It is noted that the magnitude of thermopower at 300K is smaller when compared to the previous results reported by Lee *et al*.

The systematic measurements of thermal conductivity for the single crystals of Na_xCoO_2, ($x \approx 0.80$, 0.85, 0.88, 0.96 and 0.97) are reported by Lee *et al.* (see figure 4.3 (a)) and ($x \approx 0.31$, 0.50 and 0.71) are reported by Foo *et al.* (see figure 4.3 (b)). Lee *et al.* reported, at high *x,* the in-plane thermal conductivity show the values lies between 7 and 12 W/mK. At low temperature 'κ' increases steeply and is peaked around 75 to 100K, and starts decreasing slowly with increasing temperature.

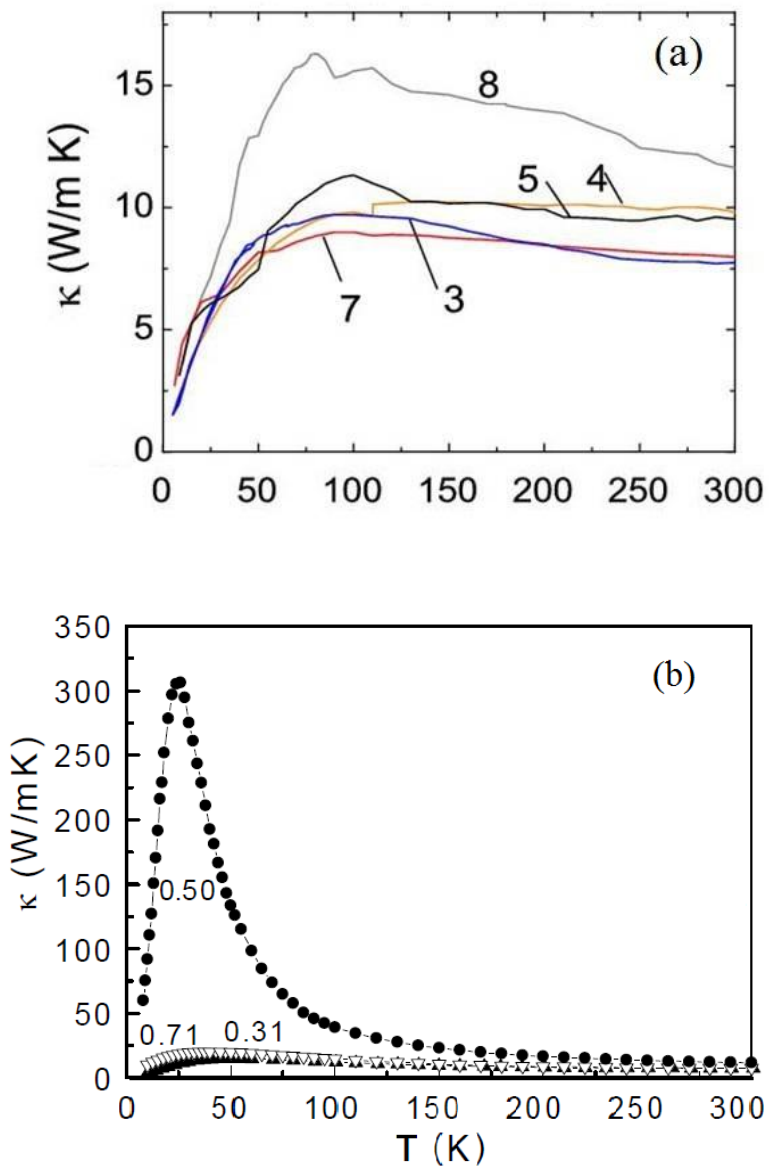

Figure 4.3: In-plane thermal conductivity of Na_xCoO_2 (a) 3 (x=0.80), 4 (x =0.85), 5 (x =0.88), 7 (x =0.96) and 8 (x =0.97) respectively [56], shows increasing trend in conductivity as a function of x and (b) x = 0.32, 0.50 and 0.71, shows abrupt change at x=0.50 at low temperature, Ref.: [47].

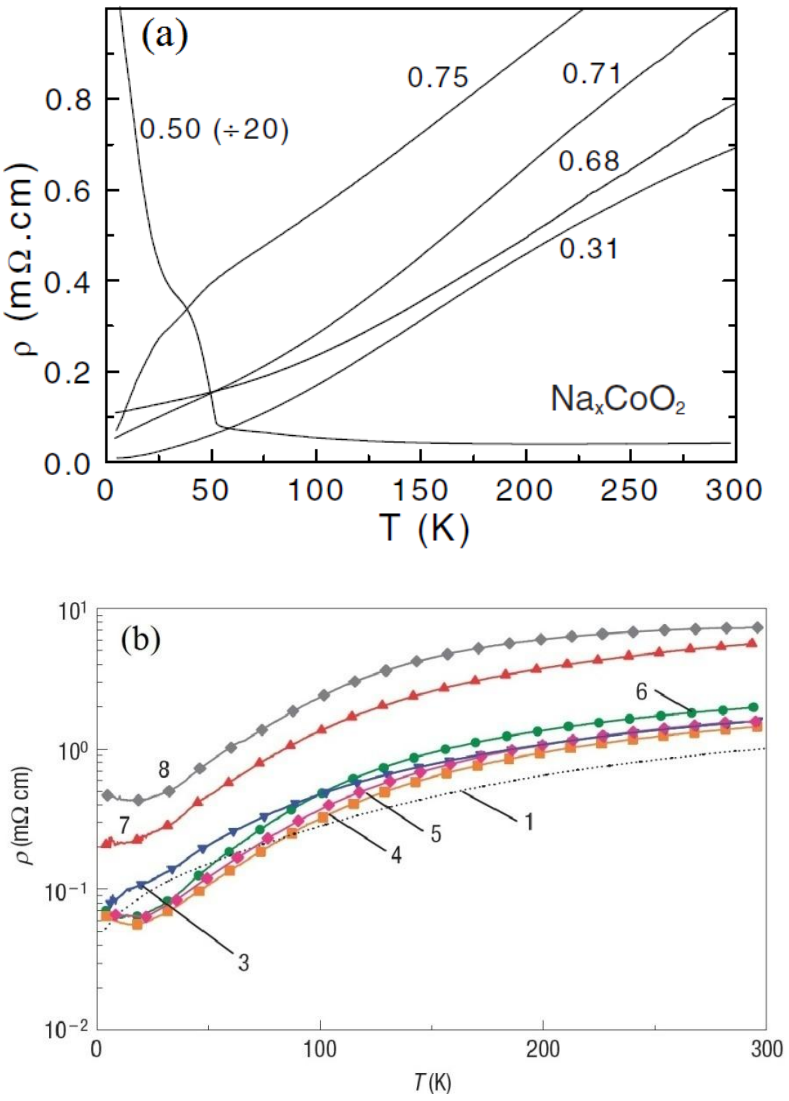

Figure 4.4: In-plane resistivity of Na_xCoO_2, (a) x=0.31, 0.68, 0.71 and 0.75 showing increasing trend in resistivity at 300K, while x=0.50 shows abrupt change around 50K infers the charge order insulating behaviour, Ref.: [59], (b) 1 (x=0.71), 3 (x=0.80), 4 (x =0.85), 5 (x =0.88), 6 (x=0.89), 7 (x =0.96) and 8 (x =0.97), shows increasing trend in resistivity towards 300K as a function of x, Ref.: [56].

The in-plane electrical resistivity measured for Na_xCoO_2 single crystals with different x by Foo *et al.* [47], is shown in figure 4.4 (a). There is an abrupt change in resistivity observed around 50K that is attributed to the insulating behaviour of $x = 0.5$, where ρ rises rapidly and reaches 20 mΩ cm at 4K. For high value of $x = 0.68$, 0.71 and 0.75, ρ has a distinctive linear profile to temperature. Lee *et al.* reported the lowest in-plane resistivity so far for Na_xCoO_2, $x \approx 0.71$, 0.80, 0.85, 0.88, 0.89, 0.96 and 0.97, as shown in figure 4.4 (b). The resistivity ρ increases linearly as a function of temperature and at room temperature, ρ as a function of x lies between 1 and 2mΩ cm.

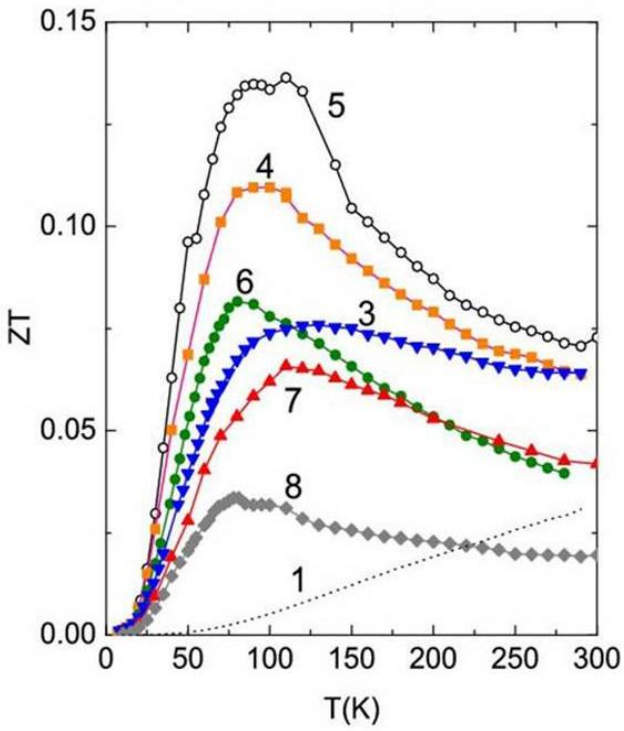

Figure 4.5: Dimensionless figure of merit, ZT of Na_xCoO_2, 1 (x=0.71), 3 (x=0.80), 4 (x =0.85), 5 (x =0.88), 6 (x=0.89), 7 (x =0.96) and 8 (x =0.97), Ref.: [57].

The dimensionless figure-of-merit (ZT) for Na_xCoO_2 with different x is shown in figure 4.5. The figure-of-merit has a maximum near 100K and the maximum value is about 0.13 at high x.

The magnetic ordering in the sodium cobaltate system has been studied using different techniques, and the long range ordering apparently shows the ordering temperature between 19K and 22K for x = 0.75 – 0.9, as reported by several authors [60-62]. Mukhamedshin et al. reported Nuclear Magnetic Resonance (NMR) studies that show a similar kind of transition but the change in the magnetic state from x=0.7 to 0.75 with T_N=22K was attributed to cobalt charge ordering[63]. A transition at 27K was observed for x=0.85 with a large anisotropy of magnetic behaviour. For field direction parallel to the c-axis, the susceptibility drops down suddenly, whereas for a field perpendicular to the c-axis it increases significantly [64], as shown in figure 4.6.

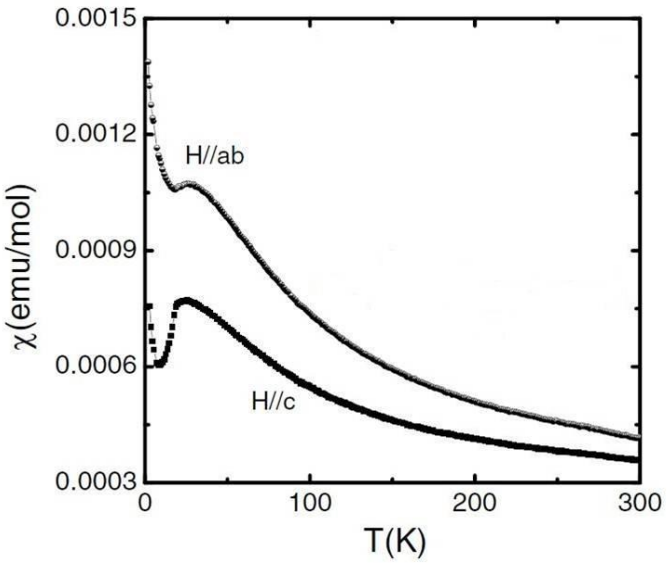

Figure 4.6: Magnetic susceptibility χ vs T for x=0.85 with B= 1T applied along and perpendicular to the c-axis. Ref.: [64].

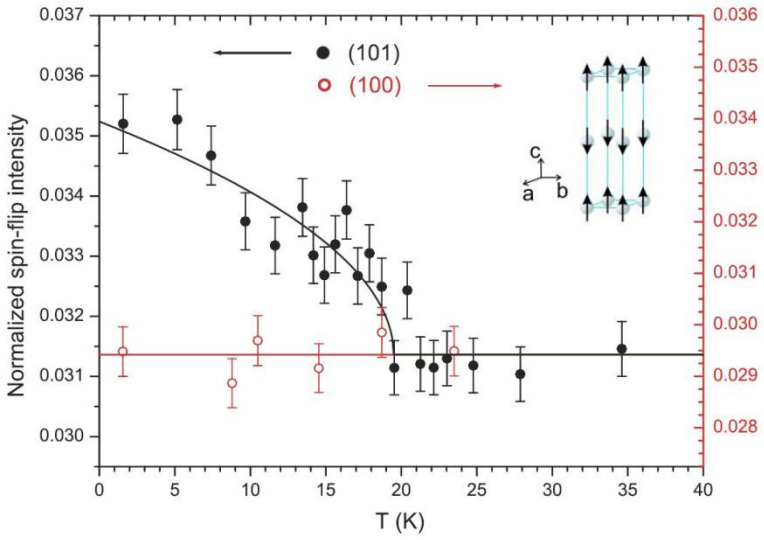

Figure 4.7: Polarised neutron measurements of $Na_{0.82}CoO_2$. Ref.: [65].

The magnetic structure determined using polarised neutron diffraction is an A-type antiferromagnetic ordering with ferromagnetic ordering in Co layers and the magnitude of the moment in the c-direction is 0.13 μB [65].

In this chapter, we are able to measure the thermoelectric and magnetic properties of Na_xCoO_2 single crystals with different x and known superstructures. Our data are consistent with the previously reported literature and we are able to relate changes in physical properties directly to the superstructures.

4.3 Experimental procedure

4.3.1 Thermal transport measurements

Figure 4.8: Thermal transport puck with $Na_{0.5}CoO_2$ sample mounted and the bar shaped copper leads are connected to the sample using the silver epoxy.

The thermal transport measurements were performed on Na_xCoO_2 single crystals using the Quantum Design - PPMS at Royal Holloway. As mentioned earlier in chapter 3, a variety of single crystals with different x have been obtained through bromine de-intercalation experiments. The thermal transport option (TTO) puck that follows the two probe method was used, as shown in figure 4.8. Prior to beginning measurements, two leads of gold plated bar-shaped copper contacts were connected to the single crystal of typical size 12x4x2mm^3 using silver epoxy mixed in a 1:1 ratio (silver loaded adhesive : hardening resin) and kept inside a vacuum controlled desiccator for a day to dry out the glue, so that the connecting leads would not detach from the sample. The leads were carefully connected due to the

fragility of the sample. The TTO puck was allowed to measure from 5K to 300K and vice-versa under high vacuum conditions. This system can measure thermal properties such as the Seebeck coefficient, the thermal conductivity, the electrical resistivity and combining these three together to calculate the figure of merit. The figure-of-merit is the quantity of practical significance, where it measures the efficiency of a material's ability to transport heat by the application of an electric current (Peltier effect), or conversely a material's ability to generate an electric field by passing a thermal current (Seebeck effect) [29]. The thermal conductivity and the Seebeck coefficient measurements give considerable information about the electronic as well as the ionic lattice structure of the material. The electrical resistivity measured using this technique was not found to be reliable. Hence it was measured separately using the four point probe technique using the resistivity puck which will be explained in detail in the next section.

4.3.2 Four probe resistivity measurements

The sample preparation for the four probe resistance measurement is highly delicate because of the smaller sample size. Single crystals of sodium cobaltate are cleaved from a large boule and broken down further into much smaller pieces that are large enough to attach the four gold wires having 25μm diameter. The typical size of the sample was around 600μm in length. Samples taken from freshly grown large crystals give better results compared to the very old samples. The samples were cut down into tiny *ab* plates, from one of those crumbs of the sample. It was necessary to choose the best bit showing a flat, smooth and shiny surface, where there were not any visible steps over the surface. The contacts sit on the *ab* plane/the shiny flat surface so, if any steps occurred, that would reduce the quality of the resistivity measurements.

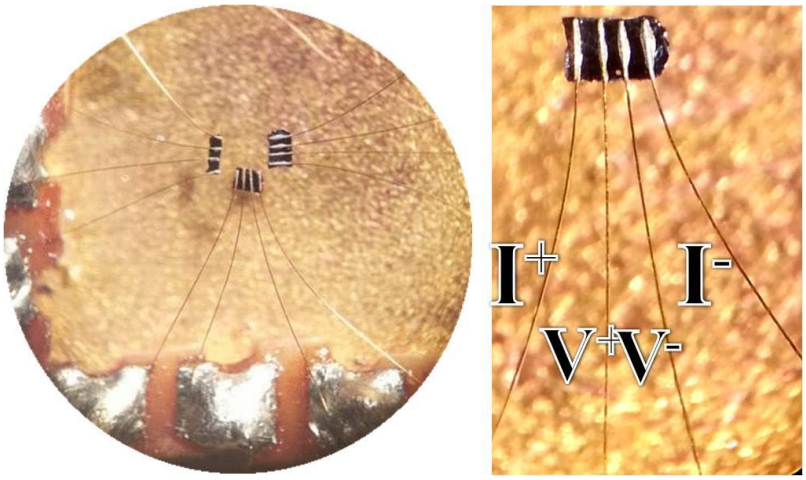

Figure 4.9: Flat sample of $Na_{0.8}CoO_2$ mounted over the resistivity puck. Four wires indicating four probes showing I^+, I^-, V^+ and V^- connected to the flat sample using silver glue.

After this stage, the samples were ready for connecting the gold wires. Before connecting the wires to the sample, a very small amount of vacuum gel was placed over a glass slide using the tip of a needle and the sample was stuck on it. Care was taken not to contaminate the surface of the sample by the gel. Once the sample was in place, silver epoxy was mixed in 1:1 ratio (silver loaded adhesive : hardening resin) and mixed gently for a minute. 25μm diameter gold wire of length around 1.5cm was poked into the silver glue mixed already. A silver glue blob was then at the end of wire. If the blob is too large to apply to the sample, it was removed by touching the wire over on slide again before applying onto the sample. At this crucial stage, the wire was placed onto the sample very carefully using rigid tweezers and then the tweezers were removed from the wire. Once all the contacts were fixed onto the sample, it is advisable to pass a current through the wires to confirm the contacts are properly fixed and it is believe that it aligns the conducting atoms in the silver glue making reliable

contacts, but due to the fragility and delicacy of the sample and the wires, it is not necessary to follow this process at this stage.

Figure 4.10: Resistivity puck with three samples mounted and connected with four gold wires using silver glue.

The single crystals of Na_xCoO_2 easily absorb moisture from the air leading to white patches on the surface of the sample. Hence samples should be preserved inside desiccators under vacuum for all periods other than the sample preparation time. The samples are very small and too unstable to undergo baking after the sample preparation, and then must be kept inside the desiccators for 24 hours to dry out the silver glue.

Using a scalpel, the sample was removed carefully from the glass slide and placed on the resistivity puck by attaching the wires to the desired channel in the puck. Separating the wires using the needle and tweezers, the wires were soldered onto the puck. The outside current wires I^+ and I^- were soldered first, and the sample was raised slightly upwards, as shown in figure 4.9. Because of the small size of sample it can easily float in mid air using the wires attached to it. In such a way the shortage of other wires can be eliminated. Then the other two inner wires of V^+ and V^- were soldered

and no wires were allowed to touch the base of the puck, excess wires poking out the back of the contact pads were removed. At this stage the sample is ready for resistivity measurement using the PPMS system (see figure 4.10).

4.3.3 SQUID/VSM

The magnetic properties of Na_xCoO_2 were measured using the Quantum Design - SQUID/VSM on the I10 beam line at Diamond Light Source. A series of samples with different *x* were measured with the field parallel and perpendicular to the c-axis and for each orientation field cooled (FC) and zero-field cooled (ZFC) measurements were performed with an external magnetic field B = 1 Tesla.

4.4 Results

4.4.1 Seebeck Coefficient

The Seebeck coefficient measurements for Na_xCoO_2 single crystals with different x are shown in figure 4.11 (a). The samples with high Na content demonstrate high thermopower behaviour. The results measured are reproducible and they were found to be comparable to the values achieved by previous authors [1, 58]. In general, the Seebeck coefficient increases with temperature, and if the sodium content is reduced, the thermopower decreases.

For the high doping region x = 0.8 and 0.77, an antiferromagnetic phase transition is observed at 21K and this is indicated by the line in figure 4.11 (b). For these concentrations, the thermopower drops dramatically near to zero at the Néel temperature which is reproducible and considered to be a remarkable feature. For x = 0.8, a high thermopower is observed showing S=124.5 μV/K at 300K. Here the spin entropy is believed to be carried by the holes and it is associated with the channelling of holes leading to strong correlations, and this enhances a high thermopower in the striped phase sodium ordering region [3, 35, 66]. The thermopower values at high doping region are reproducible and consistent with the increasing trend towards the room temperature values obtained by Terasaki *et al.* [1] and Kaurav *et al.*, [58] as shown in figure 4.1 (a) and 4.2 respectively.

At x = 0.5 and in the incommensurate region (x = 0.54−0.61), the Seebeck coefficient starts with a negative regime at low temperatures and cross over to a positive regime occurs as the temperature increases towards room temperature. This is consistent with the previously published results by Kaurav *et al.* This sign change of thermopower suggests that there may be a

substantial change in the band structure or the conduction mechanism of the charge carriers at these particular *x* concentrations [58].

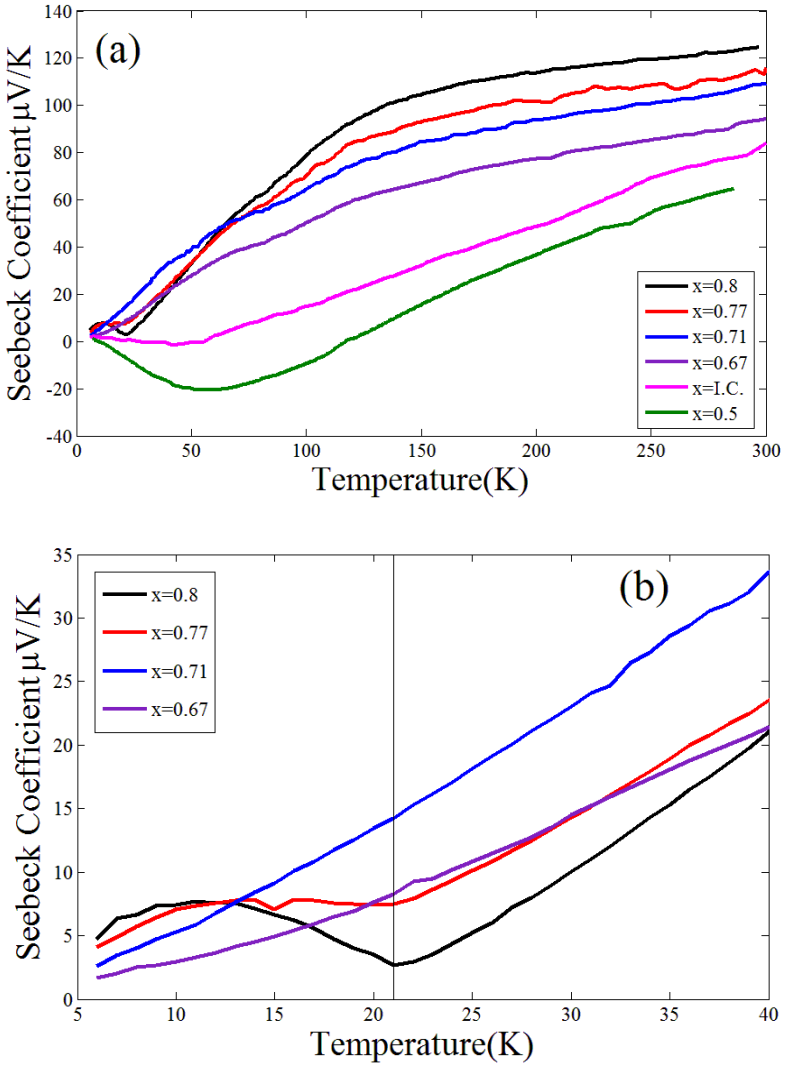

Figure 4.11: (a) Seebeck coefficient measurements for Na_xCoO_2. (b) Close up plot of Seebeck coefficient with magnetic transitions T_N ~21K at x = 0.8 and 0.77 indicated by a line.

4.4.2 Electrical resistivity

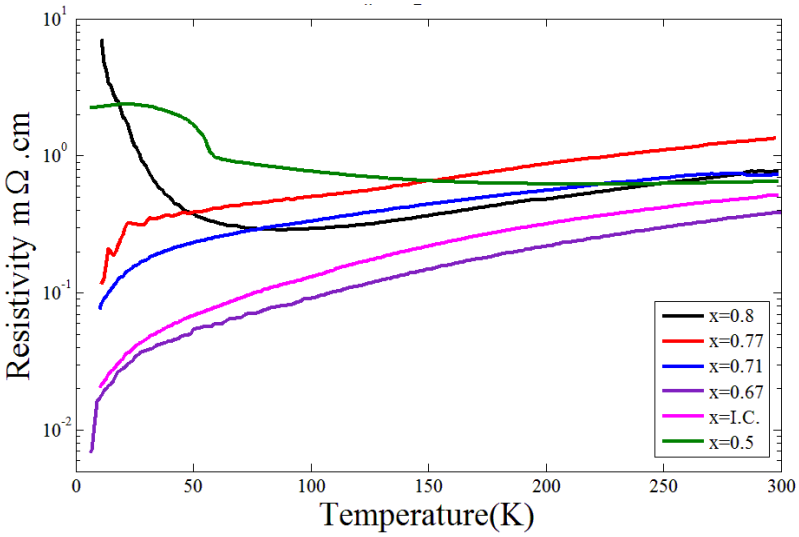

Figure 4.12: Resistivity measurements for Na_xCoO_2 with varying x.

The in-plane resistivity measurements for Na_xCoO_2 are shown in figure 4.12. The single crystals of Na_xCoO_2 of varying x were measured between 5 and 300K, and all those measurements were performed with the AC (Alternating Current) mode using the resistivity puck in the PPMS. Due to the fragility and size of the samples and the connecting wires, many attempts were made with several samples to obtain a clear picture of the resistivity for a particular composition.

The values of the electrical resistivity are comparable and even better than those values reported previously for Na_xCoO_2 by Lee *et al.* [56]. High quality as-grown single crystals of size ~400μm were used to study the in-plane electrical resistivity of Na_xCoO_2, which is comparable in size to that reported by Lee *et al.* At room temperature, the resistivity for Na_xCoO_2 lies between ρ = 0.3−1.5 mΩ cm. The in-plane resistivity for x = 0.5, 0.71 and 0.85 lies in the region ρ = 0.6−0.8 mΩ cm, as shown in figure 4.12. In a

narrow region of x = 0.5, the electronic phase represents a charge ordered insulating behaviour and this is observed in an abrupt jump in the resistivity near ~50K. This is found to be reproducible, and it is consistent with the results previously reported by Foo *et al.* [35]. A Curie–Weiss metallic state is found for sodium contents x > 0.5. In this metallic phase, the resistivity shows a linear dependence on temperature [35, 56].

For x = 0.71, there is an occurrence of a small step at 285K [37], and this coincides with the structural change in the stacking of sodium planes described in Chapter 3. For x = 0.8, the resistivity ρ = 0.78 mΩ cm is obtained at T = 300K. The increase in resistivity at low temperatures is reproducible, but it is not presently understood.

For x = 0.77, the resistivity increases, showing ρ = 1.34 mΩ cm at 300K. The lowest resistivity is obtained for x = 0.67 at 300K with ρ = 0.38 mΩcm. For the incommensurate phase region x = 0.61–0.54, ρ=0.51 mΩ cm at 300K. The resistivity is dependent on superstructure and the low values reported here enhance the figure-of-merit.

4.4.3 Thermal conductivity

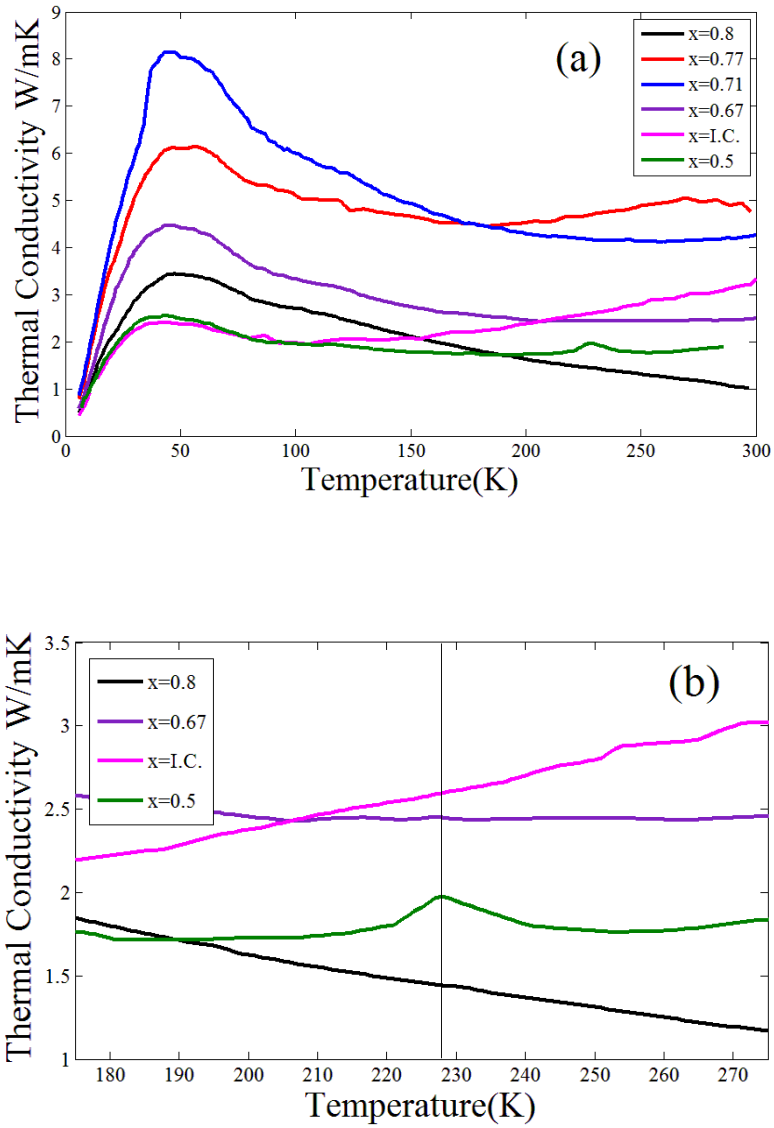

Figure 4.13: (a) Thermal conductivity measurements for Na_xCoO_2. (b) Close up plot of thermal conductivity for $x = 0.5$ showing a peak near 230K.

The thermal conductivity was measured concurrently with the Seebeck coefficient for the same samples using the TTO puck in PPMS. However, the data obtained for the thermal conductivity are less reproducible and lower than the previously reported values [56-57]. They are therefore considered to be less reliable. In contrast to the temperature dependencies in Fig 4.3, the thermal conductivity in Fig 4.13 (a) are peaked at T ~ 50K. The lineshape suggests that the scattering is dominated by phonon scattering, whereas the previous results were dominated by defect scattering. This is due to the suppression of the lattice contribution to the thermal conductivity from the electronic contribution and also the strong-correlation fluctuations help to suppress the phonon contribution to the thermal conductivity to attain a high thermoelectric power.

At $x = 0.5$, there is a small peak at 228K, as indicated by the line (see figure 4.13 (b)). This coincides with the transition to the $1/12^{th}$ superlattice peaks described in chapter 3 and in RXS experiment in chapter 5. The $1/12^{th}$ superlattice peaks for $x = 0.5$ observed from the low temperature phase disappear at 230K as temperature increases and reappear at 220K when it is cooled. Hence this observed anomaly in the thermal conductivity appears to be connected to the formation of the $1/12^{th}$ phase.

4.4.4 Figure-of-merit

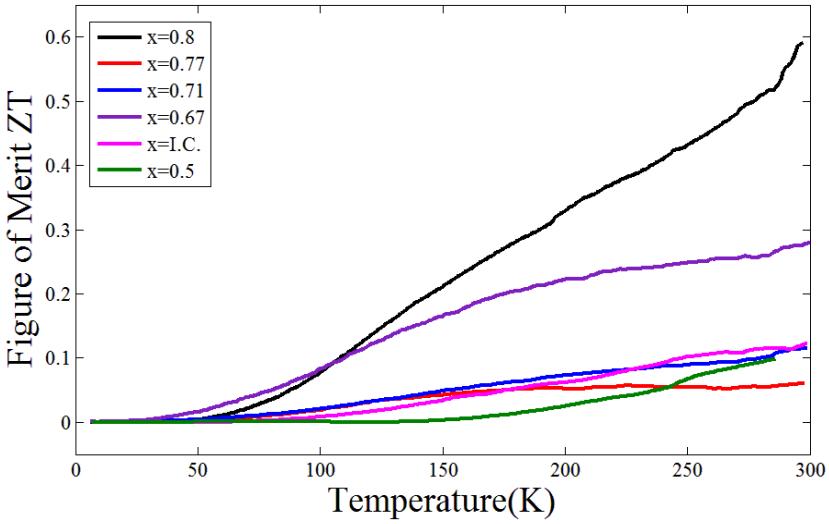

Figure 4.14: Dimensionless figure merit for Na_xCoO_2

The dimensionless figure of merit, $ZT = S^2T/\rho\kappa$, determined using the results obtained from the thermopower 'S', the thermal conductivity 'κ' and the electrical resistivity 'ρ' for Na_xCoO_2 single crystals is shown in figure 4.14. Partly as a result of the low thermal conductivity observed for $x = 0.8$, the highest figure-of-merit ZT = 0.6, is obtained for this composition. It is higher than the previously reported values by Lee *et al.* [56]. The figure-of-merit ZT lies at 0.27 for $x = 0.67$ at 300K. The ZT for other concentrations $x = 0.5$, 0.61−0.54, 0.71 and 0.77 lies between 0.06 and 0.12.

4.4.5 Magnetic properties

Magnetic property measurements were performed for the Na_xCoO_2 single crystals using SQUID/VSM in the I10 beamline at Diamond Light Source. The measurements were done for field directions parallel and perpendicular to the *c*-axis with the external applied field B = 1 Tesla, as shown in figure 4.15. The Néel temperature (see figure 4.15, indicated by a line), T_N is observed exactly at 20.6K for x = 0.8 and 21K for x = 0.77, and no other transitions were observed at these concentrations and these transitions were observed only for the H | | C orientation.

For the samples at a high doping Na, x = 0.8 and 0.77, antiferromagnetic ordering occurs below T ≈ 21K. The peak in the curve for fields in the *c*-direction indicates an antiferromagnetic transition with ordered moments along the *c*-direction. These transitions are consistent with the data previously reported for $Na_{0.82}CoO_2$ by Bayrakci *et al.* [61]. Interestingly, in the antiferromagnetic phase at a high doping region of x, the cobalt spins are ferromagnetically aligned in the plane and these ferromagnetic planes are stacked antiferromagnetically along the *c*-axis, giving rise to a spin-flop transition of the A-type antiferromagnetic structure [60, 65]. This result is clearly observed by magnetic structure studies using neutron diffraction, which reveal the A-type antiferromagnetic ordering with ferromagnetic ordering in layers of CoO_2 and moments along *c*-direction for $Na_{0.8}CoO_2$ with a Néel temperature $T_N \approx$ 22K, as reported by Dr. D. G. Porter [3].

For metallic samples with x = 0.71 and below, we find no evidence for magnetic transitions down to T ~ 2K. This is consistent with previous authors.

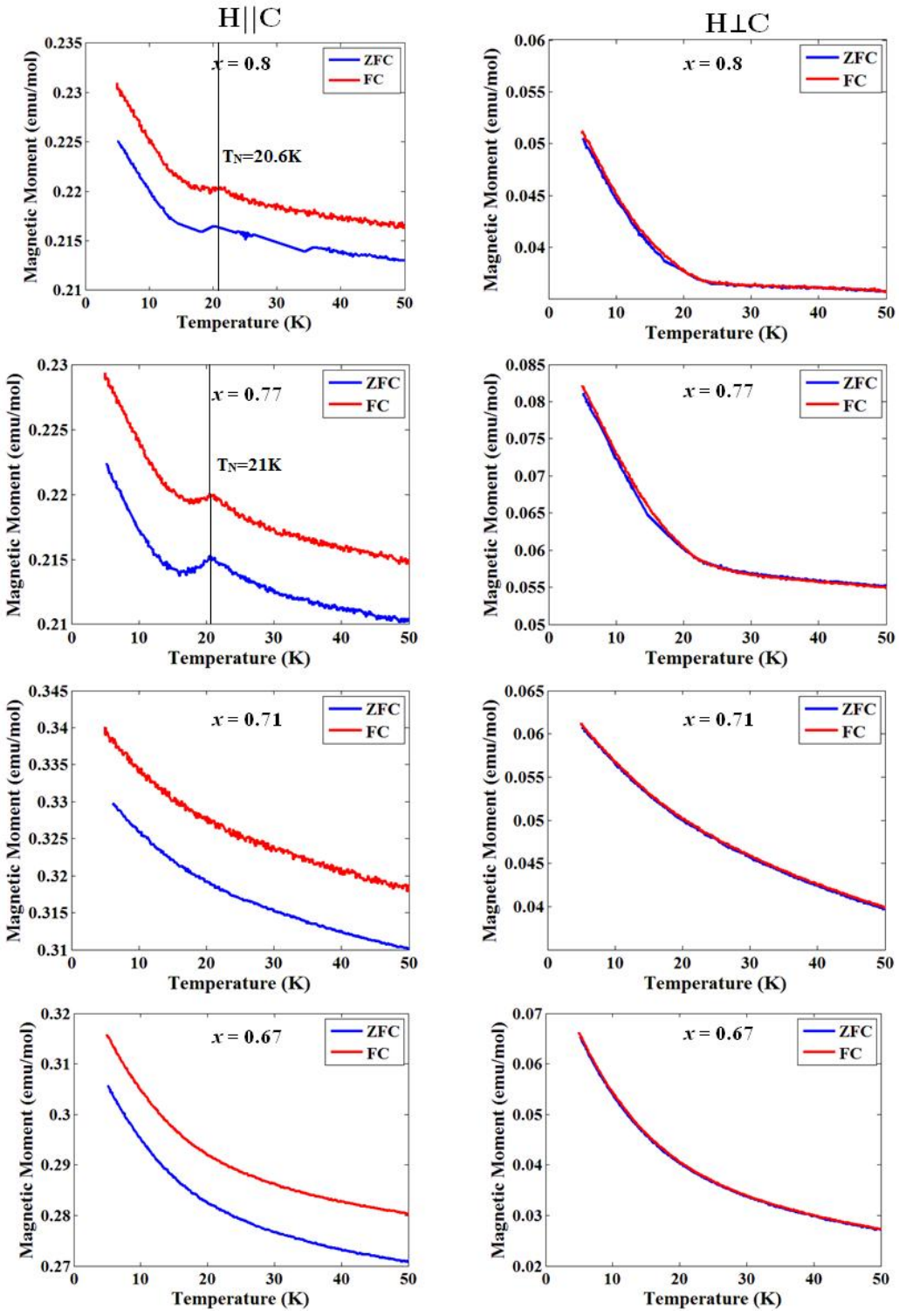

Figure 4.15: Magnetic moments of Na_xCoO_2, with H||C and H⊥C showing FC and ZFC plots. Néel temperature is observed for $x = 0.8$ and 0.77 is indicated by a line.

4.5 Discussion

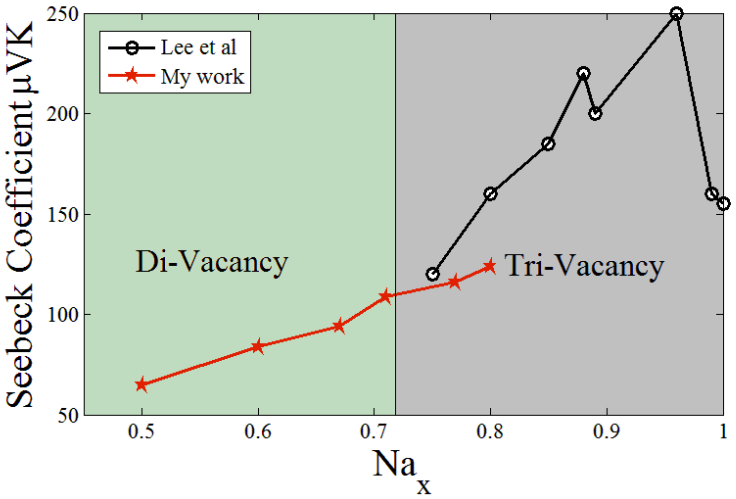

Figure 4.16: Optimum values of the Seebeck coefficient as a function of concentration *x* at room temperature.

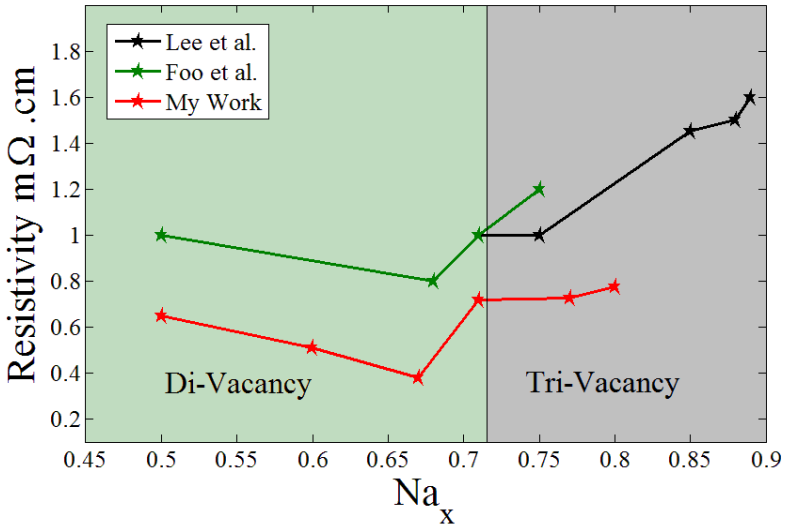

Figure 4.17: Optimum values of the in-plane electrical resistivity as a function of concentration *x* at room temperature.

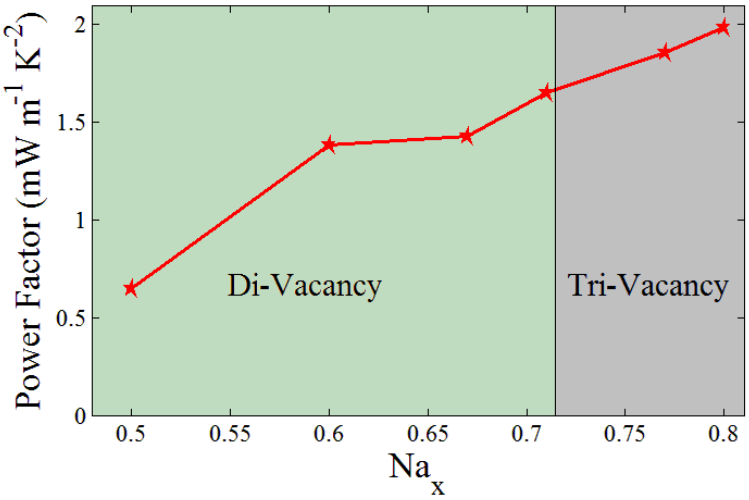

Figure 4.18: Power Factor as a function of concentration x at room temperature with a transition of di–vacancy to tri–vacancy of Na^+ ordering.

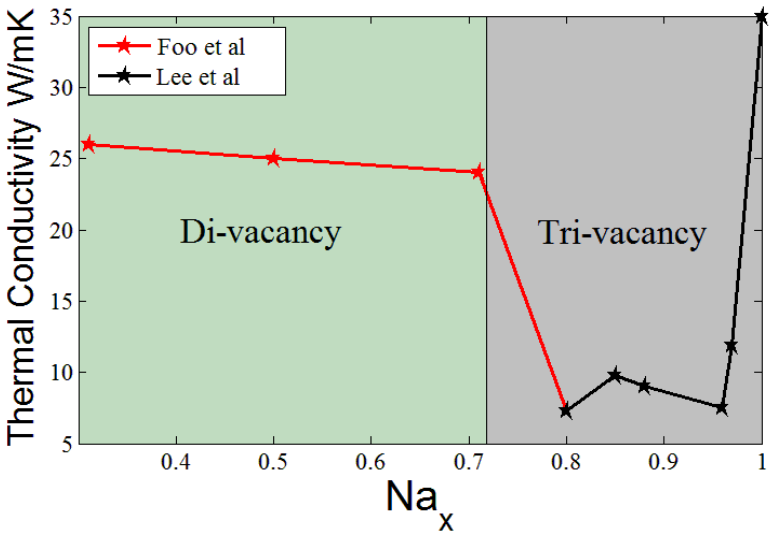

Figure 4.19: Optimum values of the Thermal conductivity as a function of concentration x at room temperature.

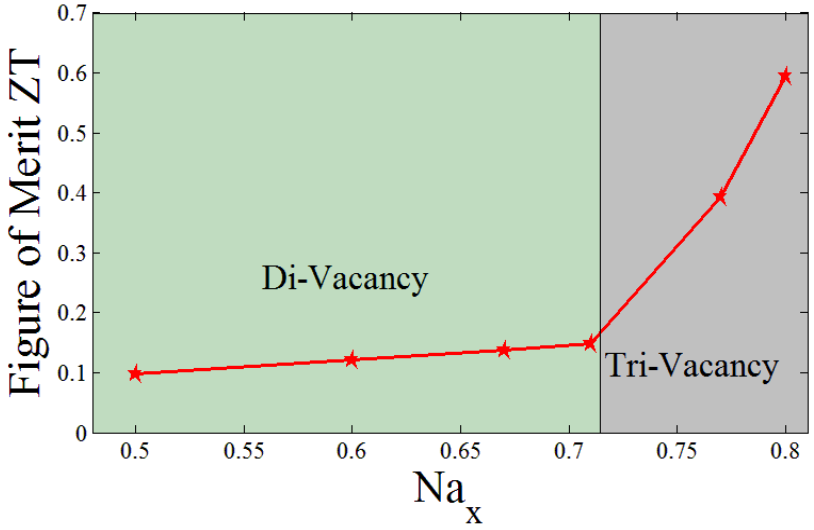

Figure 4.20: Figure-of-merit with a transition of di–vacancy to tri–vacancy of Na^+ ordering. (Thermal conductivity data were obtained from Foo *et al.* [59] and Lee *et al.* [56], and not from the experimental data of this thesis)

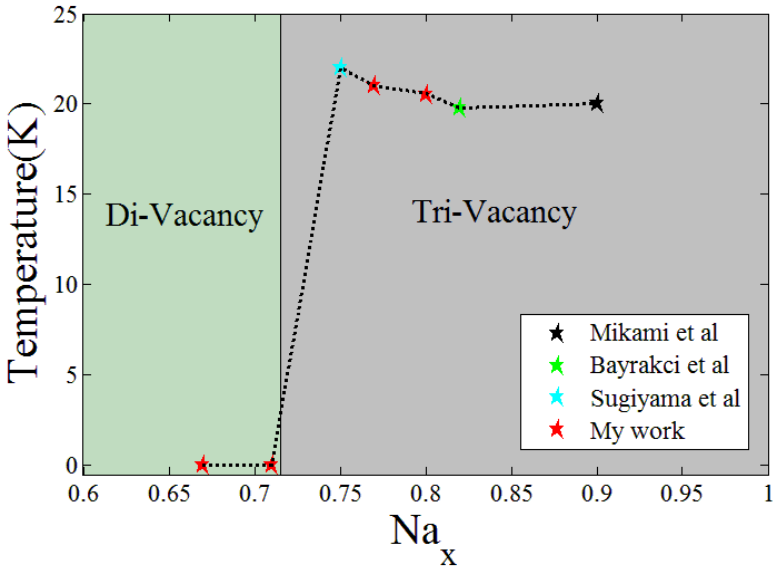

Figure 4.21: Néel temperatures for di–vacancy to tri–vacancy transition.

In figure 4.16 – 4.20 the best available values of the thermoelectric parameters are presented over the composition range $0.5 < x < 1$. The compositions where the superstructures are based on di-vacancy clusters are shaded in green, and the region of tri-vacancy clusters is shown in grey. There are clear changes in all three thermoelectric variables between the di-vacancy and tri-vacancy phases. In Fig 4.16, the Seebeck coefficient is seen to rise substantially as concentration increases for tri-vacancy clusters. This is beneficial for the thermopower and figure-of-merit. The power factor obtained for different x concentration at room temperature substantially increases for tri-vacancy superstructures, see Fig 4.18. The thermal conductivity decreases for tri-vacancy superstructures, see Fig 4.19. Again this is beneficial for the figure-of-merit. Although there is an increase in the resistivity for tri-vacancies (Fig 4.17), overall there is an improvement of the figure-of-merit for tri-vacancy superstructures, where the figure-of-merit is obtained using the thermal conductivity data from Foo *et al.* [59] and Lee *et al.* [56], and not from the data obtained from this thesis, see Fig 4.20.

Figure 4.21 plots the observed Néel temperatures in the same way. Again there is a dramatic correlation with the type of defect cluster. For superstructures with tri-vacancy clusters, antiferromagnetic ordering is observed below $T_N \sim 21$K. For superstructures based on di-vacancy clusters, no magnetic ordering is observed down to $T \sim 2$K.

4.6 Conclusion

There are dramatic changes in the physical properties when the superstructures change from di-vacancy to tri-vacancy clusters. The improvements in Seebeck coefficient and thermal conductivity, combined with a deterioration of the electrical resistivity lead to a large enhancement

of the figure-of-merit for tri-vacancy clusters. The overall thermoelectric performance is better than has previously been reported.

The effect of the cluster type is even more drastic for the magnetic properties. When the superstructures are based on tri-vacancies, antiferromagnetic ordering occurs below T_N ~ 21K. However, for superstructures based on di-vacancies, the magnetic ordering is completely suppressed. Furthermore, there appears to be a link between the magnetic and thermoelectric properties, since the Seebeck coefficient is suppressed at precisely the Néel temperature.

Chapter 5

Electronic ordering in $Na_{0.5}CoO_2$

5.1 Abstract

The electronic ordering in $Na_{0.5}CoO_2$ was studied using Resonant X-ray Scattering (RXS) measurements on the I16 beamline at the Diamond Light Source. Large resonant signals were detected in the rotated polarisation channel. The resonant signal was compared with density-functional calculations from the striped di-vacancy superstructures using the FDMNES code. Additional superlattice reflections were observed below T~220K.

5.2 Background

An electronic ordering model for an octahedral coordination with the oxygen and the cobalt atoms in the octahedral symmetry is reported by Baskaran *et al.*, where the *3d* levels are split into the higher two-fold degenerate e_g levels and the lower three fold t_{2g} levels. The trigonal distortion of the oxygen octahedra causes further splitting of the *3d* levels, where it splits the t_{2g} orbital into a non-degenerate d_z^2 with a doublet below denoted by $e_g(t_{2g})$[67]. In general, the nominal valence of the Co atom is Co^{4+}, at this stage the $e_g(t_{2g})$ is full and the d_z^2 is half filled, as shown in figure 5.1. The electrostatic potential of the Na ions play a major role to provide the charge carriers in the CoO_2 layers, because of the valence of Co ions is either 4+ or 3+. In such a way, each sodium ion contributes one electron that decreases the valence of cobalt ion to 3+, corresponding to a full d_z^2 orbital. Multiple valance states such as Co^{3+}, $Co^{3.44+}$ and $Co^{3.7+}$ have been observed in NMR experiments that differentiate the Co charge, as reported by Mukhamedshin *et al.* [63, 68]

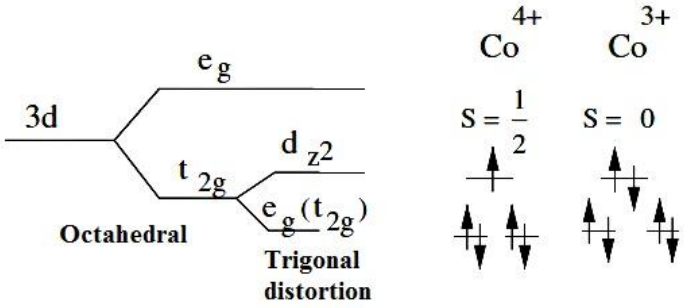

Figure 5.1: Crystal field of the Co^+ ion splits 3d orbital [67].

XANES experimental studies for different x compositions for the O-K and Co-L absorption edges show an increase in the valence state of cobalt and oxygen as x decreases, as shown in figure 5.2 [69].

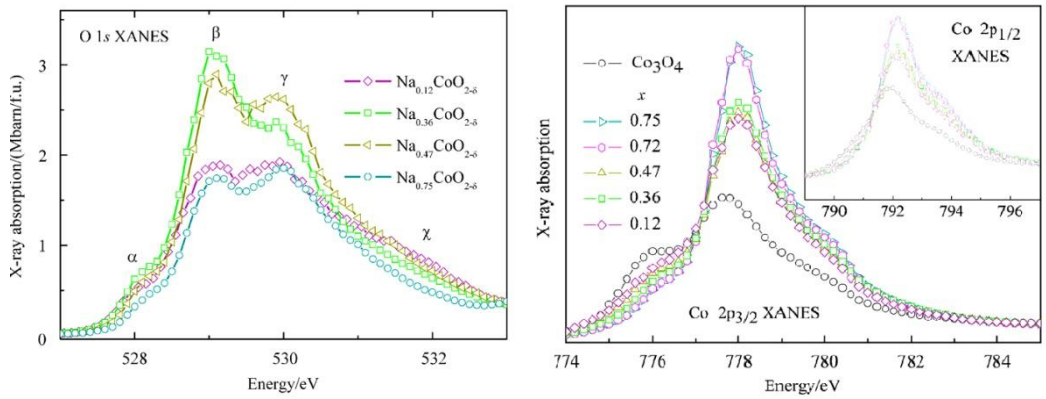

Figure 5.2: O *1s* and Co *2p* absorption spectra of Na_xCoO_2 Ref.: [69].

It is also indicated that the oxygen layers bound to the sodium ions have more electron density available for charge compensation to the cobalt ions that also expected from the electro-negativity of sodium ion. The ordering of the lattice, charge and spin has previously been studied by neutron diffraction [50, 70]. The sodium superstructure comprises alternating stripes of Na1 and Na2 sites, which can also be described as stripes of di-vacancy clusters below $x \leq 0.71$. Two inequivalent Co sites are identified with different local oxygen environment, and these are attributed to different valence states. The magnetic structure comprises stripes of large-moment and small-moment Co, consistent with stripes of Co^{3+} and Co^{3+x} following the sodium superstructure [37].

In this chapter, we are able to measure the electronic ordering of $Na_{0.5}CoO_2$, by combining the spatial sensitivity of diffraction with the sensitivity to the electronic states involved in the ordering using the resonant x-ray scattering technique.

5.3 Experimental Procedure

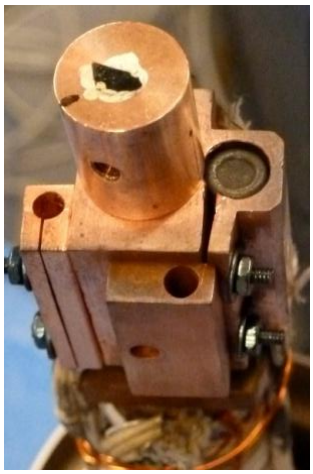

Figure 5.3: I16 sample on the goniometer facing *c*-direction

Resonant X-ray Scattering measurements were performed on the de-intercalated $Na_{0.5}CoO_2$ single crystal using the I16 beamline at Diamond Light Source. The details of the I16 instrument and the resonant X-ray scattering technique are explained in detail in chapter 2. Before the I16 experiment, the large single crystal was screened using XRD at Royal Holloway to find the orientation of the sample. The sample was mounted in a cryofurnace with the temperature range $12 < T < 600K$ and fixed to the goniometer on the I16 diffractometer. A flat and shiny single crystal with *c*-direction normal to the surface was fixed on to the copper mount using silver paint to maintain the thermal contact and allow that to dry for a few minutes (see figure 5.3). At the start of the experiment, the sample was aligned at room temperature and scans of the beam position along the surface were performed to identify the best single grain and to find the orientation of the sample. The entire experiment was performed in reflection geometry. Vertical scattering geometry was employed and the structural superlattice reflections measured in the σ-σ channel and the

resonant scattering was detected in the σ-π channel [3, 26]. So, a series of measurements of resonant scattering were performed using different scanning methods such as transverse scan, energy scan, azimuthal scan were followed, as described in section 2.2.2. In the case of azimuthal scanning, the beam often moves along the surface of the sample and it is necessary to realign to the previous position. Normalising to the charge scattering is an important factor in order get reliable data. In this experiment, normalisation was achieved by normalising the σ-π (π-σ) channel by the structural scattering σ- σ (π-π). The temperature dependence of the sample for the specified known phase transition can be related to the order parameter. After the I16 experiment, the sample was taken for screening using X-rays at Royal Holloway to examine the difference in the sample quality due to the beam heat.

5.4 Computational Modelling

The experimental results of the resonant X-ray scattering and the XANES spectra can be explained through different calculation methods. However, I used the Finite Difference Method for Near Edge Spectroscopy (FDMNES) code by Yves Joly [71] in this thesis. This code was initially developed for the XANES spectra calculation and extended to the resonant scattering calculations. Using the FDMNES code, we are able to predict the resonant scattering and the XANES spectra for a given crystal structure using the atomic coordinates of the unit cell or the supercell [3, 71-72]. These calculations can help to explain the electronic ordering, the orbital bonds and the structural characteristics for the spectra. In principle, FDMNES uses Density Functional Theory (DFT), by applying the local density approximation to solve the Schrödinger equation in a spherical volume centred on the absorbing atom and extending over a sufficiently large cluster. The FDMNES calculations are based on a spherical approach

(cluster), and not in the reciprocal space. In addition, the calculations can also be done at a mass model (bulk) or a layer (planar section). Usually, the calculations can be considered a material mass (volume) for a cluster radius of up to about 2 to 10 Å.

The electronic properties of the system are determined by the electron density function and this density value determines the electron interactions in the complex system. The electronic potential should be chosen from the two options at this point in the FDMNES. The finite difference method or the multiple scattering (MS / a muffin-tin potential) may be used. FDM uses the electronic potential where the one-electron orbital is free and it does not use approximations, and so it is challenging for the complex system such as sodium cobaltate, hence we chose a muffin-tin potential. Here the multiple scattering uses the Green formalism on a muffin-tin potential, where it calculates the electron wave scattered around the resonant site [72]. Using this method, the calculations can be much faster than the other but less precise.

Specific options have been chosen to fill the input file for the FDMNES calculations. We used the atomic coordinates of the supercell from the literature [50, 54], for $Na_{0.5}CoO_2$. The distortions of the cobalt-oxygen bond lengths can also be the reason for the resonant behaviour, due to the Jahn-Teller effect [73]. However, the atomic coordinates we used here did not include any distortions in the cobalt-oxygen layers.

We used the cluster radius 4Å, which is an important parameter and the approximation for the calculation. Using a small radius and the additional memory-save approximation that limits the number of atoms used to calculate the electronic potential and reduces the amount of memory required in the processing computer. At this stage it is possible using a

dual-core laptop, which would generally take about 4 to 6 hours to complete a set of calculations.

The calculation uses a self consistent solution, where a calculation cycle is performed over the electronic states of each atom that are calculated and re-calculated in a loop until the calculation converges without any change between successive steps. The FDMNES code calculated the resonances in the rotated channel at the superlattice peaks, lineshape for energy spectra, azimuthal dependences and the XANES spectra, and these can be compared to the experimental data by applying an offset in energy and scale factor to rectify the calibration errors. These calculated data have the same definition of the azimuthal angle and the XANES spectra and they are directly comparable to the experimental data from the I16 instrument. An input file for one of these FDMNES calculations is given in appendix A.

5.5 Results and Discussion

5.5.1 Superstructures in $Na_{0.5}CoO_2$

The best single crystal grain was identified within $Na_{0.5}CoO_2$ and the sample was aligned to the beam for *hkl* mesh scans, where we were able to measure the superstructure reflections at base temperature. As we used the reflection geometry for the measurements in the I16 instrument, it is necessary to observe the peaks at large L. At room temperature, the 1/4th superlattice reflections were observed besides the main Bragg reflections. At low temperature, T = 15K, additional superlattice reflections were observed along with the 1/4th phase peaks. These additional superlattice peaks lie on the 1/12th grid of the hexagonal lattice (see figure 5.4). These new superlattice peaks have a slightly different lattice parameter, as they are peaked at L ~ 7.04. Therefore, there appeared to be a coexistence of phases at low temperature. The existence of these two different superlattice phases were appeared from the bulk measurements using XRD with E=17.7 keV that suppose they are the bulk phases rather than the surface one, as discussed in Chapter 3.

We have chosen *(h, k,* 7*)* and *(h, k,* 8*)* planes to see the superlattice positions where the structural peaks are present and performed scanning in the energy across the cobalt-K absorption edge (≈7.78 *keV*), and these planes were measured at two different temperatures to see the differences. At T~20K, the (*h, k,* 7) shows more 1/12th peaks when compared to (*h, k,* 8) (see figure 5.5), and at T ~ 300K, both the planes show only the dominant 1/4th superlattice peaks, without any appearance of the additional superlattice peaks in the 1/3rd and 2/3rd positions. Temperature dependence measurements were performed for the specific superlattice reflections (0,

2/3, 7) and (1/2, 1/4, 7) in σ-σ and σ-π polarisations at the energy E = 7.72 *keV*.

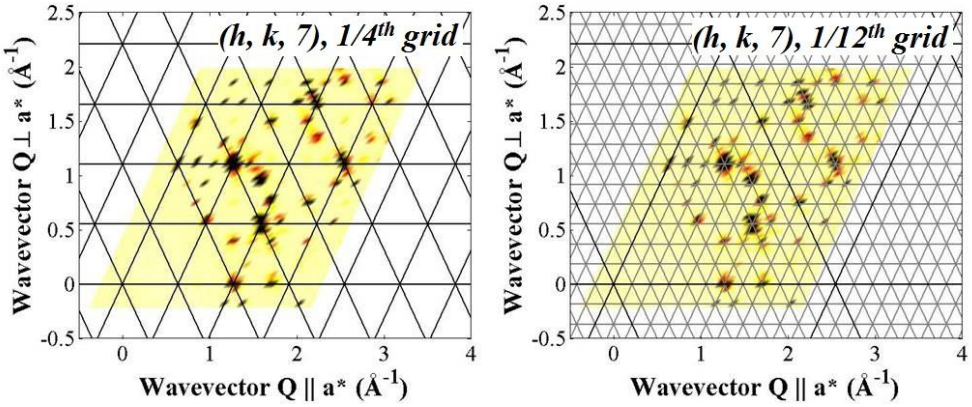

Figure 5.4: 1/12th superlattice peaks along with the 1/4th peaks in (*h, k,* 7) for $Na_{0.5}CoO_2$ at T~20K with incident energy E=7.69KeV

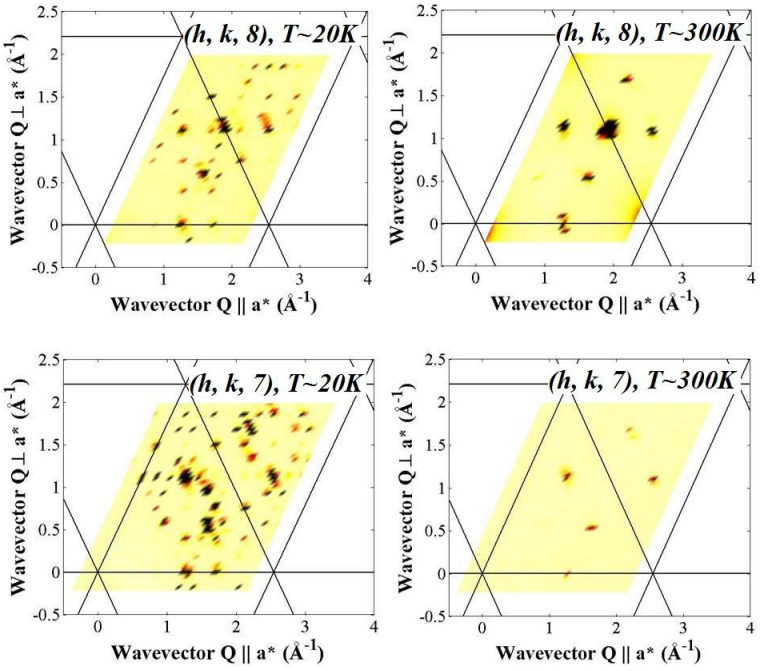

Figure 5.5: a*/12 and a*/4 superlattice peaks at T~20K and only a*/4 peaks at T=300K in (*h, k,* 7) and (*h, k,* 8) for $Na_{0.5}CoO_2$ with incident energy E=7.69KeV.

where, we found significant hysteresis behaviour of the superlattice reflections between cooling and heating cycles at the rate 1 K/scan. The intensity of the superlattice reflections increases monotonically for decreasing temperatures. The 1/12th phase disappear at 230K, as shown in figure 5.6. The cooling measurements show that there is substantial hysteresis when re-cooling the sample, where the 1/12th phase re-appears at 220K. The 1/4th superlattice reflections disappear at about 370K, with a similar trend in the hysteresis, reappearing when cooling at 340K. The hysteresis in the phase transitions demonstrate that the sodium reordering transition is a first order transition [10].

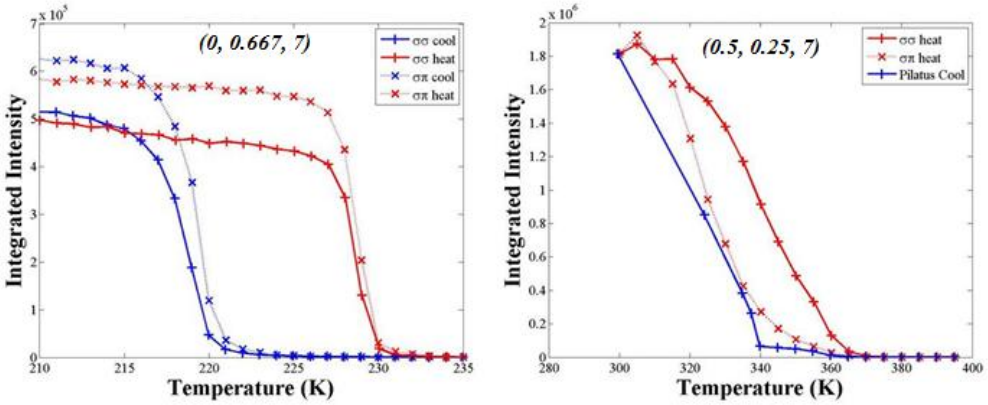

Figure 5.6: Temperature dependences of the superlattice peaks (0, 2/3, 7) and (1/2, 1/4, 7) at energy E=7.72KeV. The plots show θ scans at each temperature through σ-σ and σ-π channels. The integrated intensity of these superlattice reflections shows that the resonant and structural peaks disappear at 230K for (0, 2/3, 7) and at 370K for (1/2, 1/4, 7).

Further raising the sample temperature to 400K, we could not see the superlattice peaks, instead we observed the powder rings in (*h, k,* 7*)* and *(h, k,* 8*)* planes, as shown in figure 5.7 (a) & (b). These remained down to room temperature, indicating that the sample changed irreversibly above the

disorder temperature. Figure 5.7 (c) & (d) shows the lab X-ray diffraction images from before and after the experiment, indicating the appearance of rings consistent to the I16 experiment. The powder rings are much weaker with penetrating high energy X-rays, demonstrating that the changes occur at the surface.

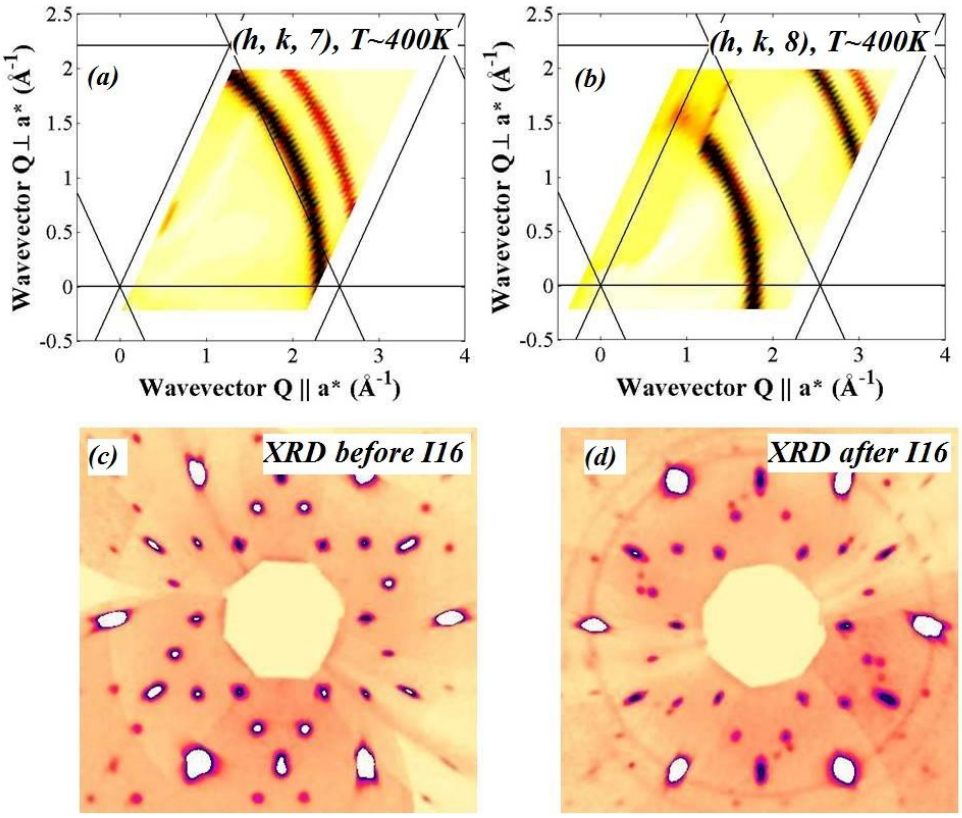

Figure 5.7: Appearance of powder rings in (*h, k,* 7) and (*h, k,* 8) at T=400K with incident energy E=7.69KeV and compared with X-ray measurement taken at RHUL before and after the I16 experiment.

5.5.2 Resonant X-ray Scattering

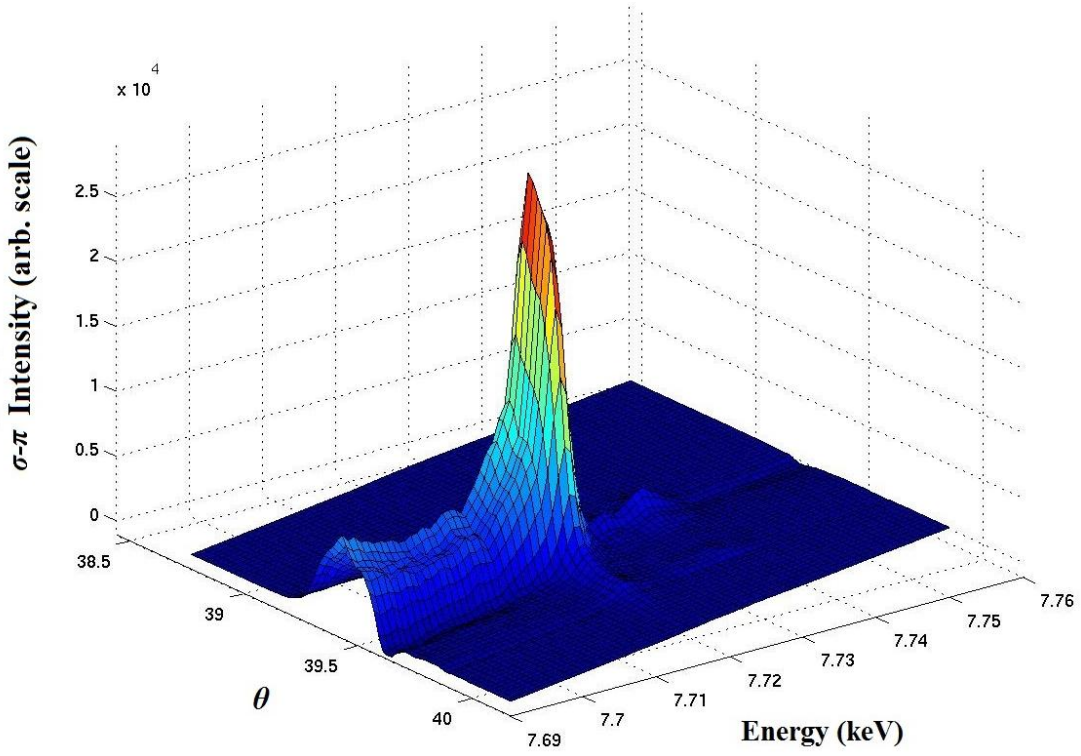

Figure 5.8: Energy Q-scan of (0, 0.5, 7), at each point in the energy, a θ-scan was performed and the resonance is peaked in both energy and reciprocal space.

To identify the specific superlattice reflections in reciprocal space, an L-direction scan was performed and then we decided to perform the polarisation dependence of the superlattice peaks using the analyser crystal, which performed the energy scans in the σ-σ (no polarisation rotation) and σ-π (rotated polarisation) channels. A mesh of θ scans with energy fixed at successive values in the area of the absorption edge for the superlattice reflection (0, 0.5, 7) is shown in figure 5.8. The peaks at the absorption edges in scans of X-ray energy with Q fixed at (0, 0.5, 7), (0.5, 0.25, 8) and (0, 0, 7) are shown in figure 5.10. These energy scans were performed in the σ-π

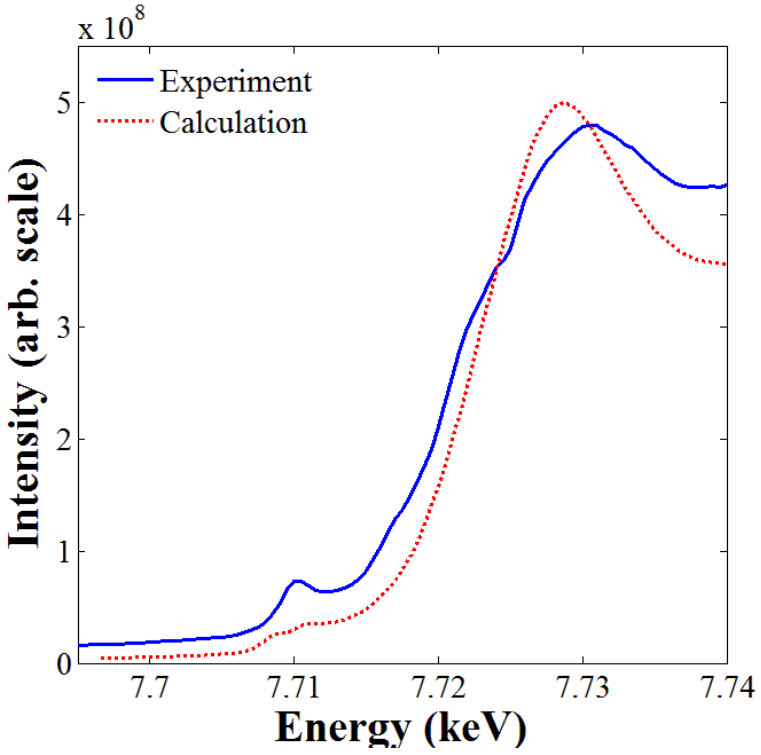

Figure 5.9: Comparison of experimental fluorescent background with XANES calculated using FDMNES.

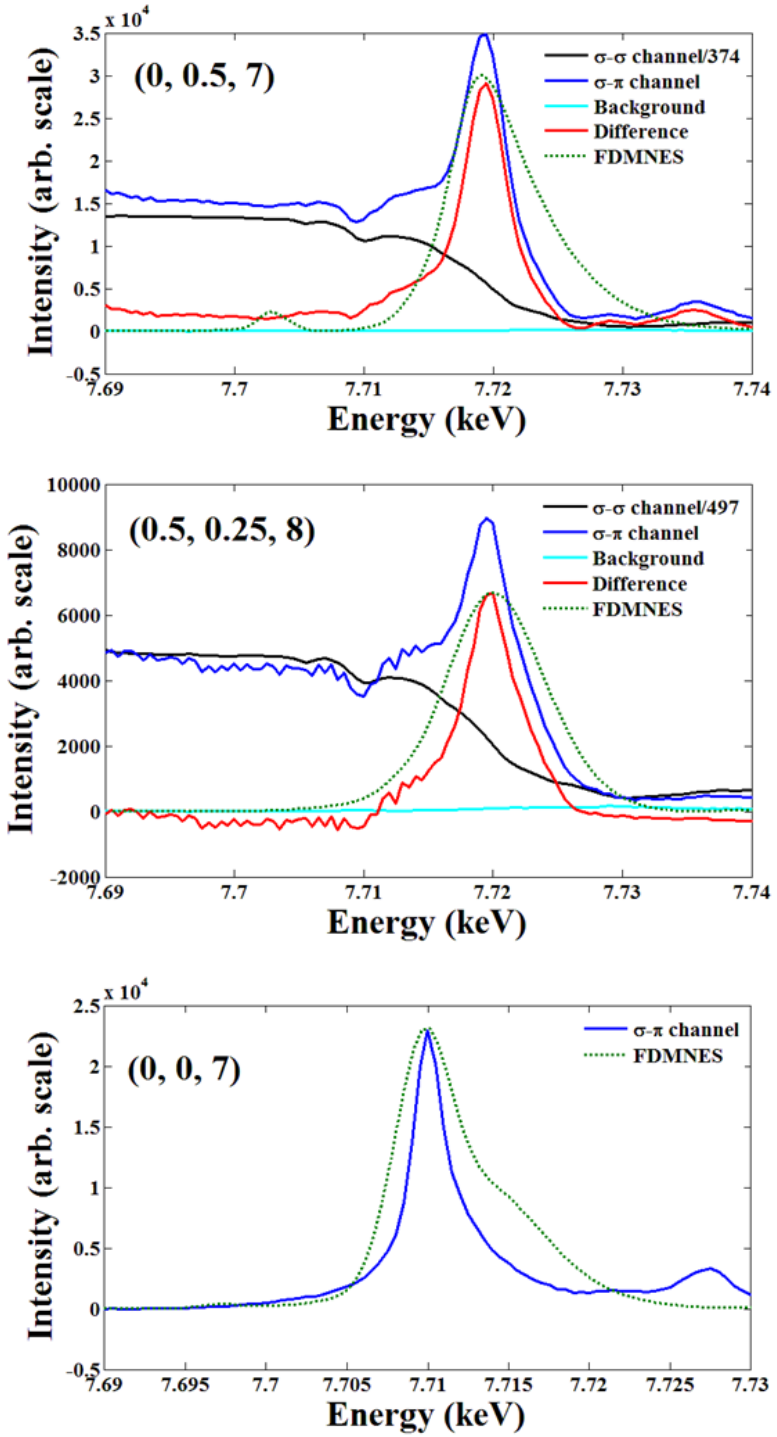

Figure 5.10: Energy scans at (0, 0.5, 7), (0.5, 0.25, 8) and (0, 0, 7) in σ-σ and σ-π channels at T=17K with energy E=7.72 keV. The calculated resonant scattering using FDMNES is shown in the dotted lines.

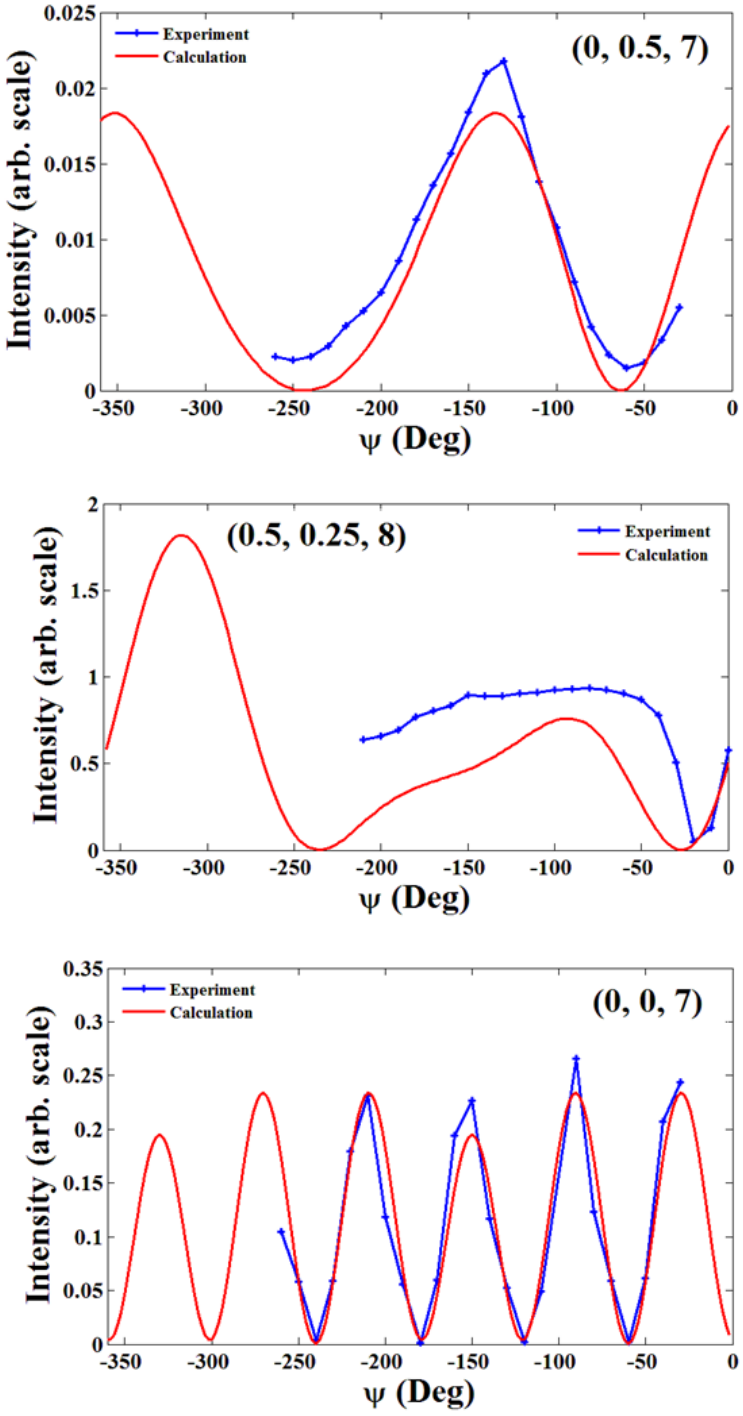

Figure 5.11: Azimuthal scans compared with the FDMNES calculations for the peaks (0, 0.5, 7), (0.5, 0.25, 8) and (0, 0, 7) with incident energy E=7.72 keV.

channel and the fluorescent background was measured away from the superlattice reflections. From the scattering at the Bragg reflection, the leakage from the σ-σ in σ-π channel was observed, and was estimated to be a factor of 374 for (0, 0.5, 7) and 497 for (0.5, 0.25, 8). In the case of a Bragg reflection (0, 0, 7), the background was very small and was neglected. Hence it was possible to estimate the leakage in σ-π channel by measuring the superlattice peak intensity in the σ-σ channel.

Azimuthal scans were performed on (0, 0.5, 7), (0.5, 0.25, 8) and (0, 0, 7) reflections as a function of azimuthal angle, in σ-σ and σ-π channels, as shown in figure 5.11. For that, normalisation of the intensities of the σ-π resonance divided by the structural intensity in the σ-σ channel was carried out, since the structural σ-σ scattering does not depend on the azimuthal angle. The FDMNES calculations were performed for these superlattice peaks using their respective atomic coordinates of the supercell for the cluster radius 4Å. These calculations show an azimuthal dependence that is consistent with the experimental data. In figure 5.10, the calculated scans were plotted after applying an offset in energy. The XANES calculation was compared with the experimental data in figure 5.9. The pre-edge feature and the main peak were reproduced. The pre-edge was considered as a main observance in the experiment, while FDMNES calculation energy has an arbitrary offset. However, we can determine this offset from the XANES. In the case of azimuthal scans, as earlier said, convergence achieved with a radius 4Å and these calculated scans agreed well with the experimental data, as shown in figure 5.11. In such a way, we are able to reproduce the energy scans and azimuthal dependencies of the resonant X-ray scattering using the FDMNES code.

5.6 Conclusion

The RXS scattering in the σ-π channel is due to electronic ordering, including charge and orbital ordering. The fact that the RXS scattering at the Co edge is peaked in **Q** at the same position as the structural superlattice peaks shows that the electronic ordering in the Co layers has the same periodicity as the Na superstructure, i.e. it is caused by the superstructure. We obtain promising agreement between the RXS from $Na_{0.5}CoO_2$ and the FDMNES calculations. Unfortunately, it is difficult to relate the FDMNES outputs simply to the charge and orbital ordering. Using more sophisticated DFT calculations using, for example, the ABINIT code, it should be possible to more easily determine the magnitude of the charge modulation and the details of the orbital ordering pattern. Since only small crystals are required for RXS, this approach could be applied to any of the superstructures in Chapter 3.

Chapter 6

Conclusions

In most of the literature on the physical properties of sodium cobaltate, the composition of the sample is only approximate and the superstructure is completely unknown. This thesis is an attempt to directly link physical properties to superstructure.

It is possible to control the sodium concentration systematically in small single crystals of sodium cobaltate using the bromine de-intercalation technique. Sodium cobaltate with different x exhibits a variety of new diffraction patterns owing to different sodium superstructures and their sodium ordering was determined using X-ray diffraction. In this way it is possible to fully map out the phase diagram over the range $0.32 < x < 0.8$ at $90 < T < 500K$.

A large number of superstructures were identified including commensurate and incommensurate structures with different types of sodium ordering as a function of x and temperature. In many cases the superstructures were solved using Reverse Monte Carlo simulations that agreed well with the experimental data.

The temperature dependences revealed sodium reordering transitions and changes in the stacking of planes. Diffuse scattering was observed above the order-disorder transition using high temperature XRD measurements, and

this was related to short-range ordering of multi-vacancy clusters. The diffuse scattering was reproduced using Monte Carlo simulations, and the diffuse rings agreed well with the experiment data.

The physical properties of Na_xCoO_2 with different x and the relationship with their sodium superstructures have been determined. The most dramatic change in magnetic and thermoelectric properties occurs when the superstructures change from a di-vacancy to tri-vacancy motif. In the case of the simple superstructure, x = 0.5, we are able to model the electronic ordering that gives rise to the observed resonant X-ray scattering.

The values of the Seebeck coefficient were comparable to the published literature. Extensive efforts to improve the measurement technique for the electrical conductivity led to better values than those reported previously. However, the values of the thermal conductivity were not as good as the best published values. Hence, it would be useful to improve the method of measurement for the thermal conductivity. This would be expected to lead to an even more reliable figure-of-merit.

The approach of using bromine de-intercalation to give a particular superstructure can now be applied for many other physical properties. For example, single crystal samples could be used in inelastic X-ray scattering studies of phonons, and these studies can be related to the thermal conductivity. Neutron scattering could be used to determine the magnetic structures, magnetic excitations and the diffusion of sodium ions.

One approach would be to use the same single crystal in a series of physical property measurements with different exposures to bromine. In the case of $Na_{0.8}CoO_2$, low temperature measurements could be performed after different cooling rates. The physical properties in the incommensurate and short-range ordered regimes are ripe for exploration.

Bibliography

1. Terasaki, I., Y. Sasago, and K. Uchinokura, Large Thermopower in a Layered Oxide $NaCo_2O_4$. Physical Review B 56, 12685-87 (1997).
2. Takada, K., et al., Superconductivity in two-dimensional CoO_2 layers. Nature, **422**(6927), 53-55, (2003).
3. Porter, D.G., Control of Electrons through Patterning of Superstructures in Sodium Cobaltate. Ph.D., Thesis, Royal Holloway University of London, (2012).
4. Kawata, T., et al., *Na-site substitution effects on the thermoelectric properties of* $Na_xCo_2O_4$ **60** 584-587, (1999).
5. Prabhakaran, D. and a.T. Boothroyd, *Floating-zone growth of* $Na_{0.8-y}A_yCoO_2$ *(A=Ca, Sr) single crystals.* Journal of Crystal Growth, **318,** 924-926, (2011).
6. Li, Y., G. Xu, and M. Jiang, *Thermoelectric characterization of* $(Na_{1-y}M_y)(1.6)\ Co_2O_4$ *(M= K, Ca, Sr).* Journal of Materials Science & Technology, **22**(4), 526-528, (2006).
7. Klein, Y., et al., *Thermoelectric power in misfit cobalties ceramics: optimization by chemical substitutions.* Boletín de la Sociedad Española de Cerámica y Vidrio, **45**(3), 122-125, (2006).
8. Ramirez, A., *Strongly geometrically frustrated magnets.* Annual Review of Materials Science, **24**(1), 453-480, (1994).
9. Berthelot, R., D. Carlier, and C. Delmas, Electrochemical investigation of the P2–Na_xCoO_2 phase diagram. Nature materials, **10**, 74-80, (2011).
10. Morris, D.J.P., Sodium ordering and control of properties in sodium cobaltate. Ph.D., Thesis, University of Liverpool, (2007).

11. Tritt, T.M. and M. Subramanian, Thermoelectric materials, phenomena, and applications: A bird's eye view. MRS bulletin, 2006. **31**, 188-198, (2006).
12. Rowe, D.M., *CRC Handbook of Thermoelectrics*. CRC press, (2010).
13. Snyder, G. and T. Ursell, Thermoelectric Efficiency and Compatibility. Physical Review Letters, **91,** 14, 148301, (2003).
14. Tritt, T.M., Thermoelectric phenomena, materials, and applications. Annual Review of Materials Research, **41,** 433-448, (2011).
15. Snyder, G.J. and E.S. Toberer, *Complex thermoelectric materials.* Nature materials, **7**, 105-14, (2008).
16. Sootsman, J.R., D.Y. Chung, and M.G. Kanatzidis, *New and old concepts in thermoelectric materials.* Angewandte Chemie (International ed. in English),**48,** 8616-39, (2009).
17. Geng, H., et al., *Thermoelectric Properties of Multifilled Skutterudites with La as the Main Filler.* Journal of Electronic Materials, **42**(7), 1999-2005, (2013).
18. Shi, X., et al., *Multiple-filled skutterudites: high thermoelectric figure of merit through separately optimizing electrical and thermal transports.* Journal of the American Chemical Society, **133**(20) 7837-7846, (2011).
19. Beekman, M. and G. Nolas, *Inorganic clathrate-II materials of group 14: synthetic routes and physical properties.* Journal of Materials Chemistry, **18**(8), 842-851, (2008).
20. Nolas, G., et al., *Semiconducting Ge clathrates: Promising candidates for thermoelectric applications.* Applied Physics Letters, **73**(2) 178-180, (1998).
21. Cullity, B.D. and S.R. Stock, Elements of X-ray Diffraction. Vol. 3, Prentice hall Upper Saddle River, NJ,(2001).

22. Cromer, D.T. and J.B. Mann, X-ray scattering factors computed from numerical Hartree-Fock wave functions. Acta Crystallographica Section A: Crystal Physics, Diffraction, Theoretical and General Crystallography, **24**(2), 321-324, (1968).
23. Brown, P., et al., Intensity of diffracted intensities, in International Tables for Crystallography Volume C: Mathematical, physical and chemical tables. Springer publications, 554-595, (2004).
24. Altarelli, M., Resonant X-ray scattering: a theoretical introduction, in Magnetism: A Synchrotron Radiation Approach. Springer publications, 201-242, (2006).
25. Takagi, H., et al., Developments in resonant x-ray scattering reveal the magnetic properties of the outer electrons of 5d transition-metal oxides. NPG Asia Materials research highlight, (2009).
26. Fink, J., et al., Resonant elastic soft x-ray scattering. Reports on Progress in Physics, **76**(5), 056502, (2013).
27. I16 - Materials and Magnetism, I16 beamline user manual, Diamond Light Source, (2010).
28. Prabhakaran, D. and A. Boothroyd, Progress in Na_xCoO_2 Single Crystal Growth, Frontiers in Superconducting Materials, Springer, 683-695, (2005).
29. Physical Property Measurement System: Thermal Transport Option User Manual, Second edition,(*Quantum Design, San Diego, 1999).*
30. Schroder, D.K., *Semiconductor material and device characterization*, Third edition, John Wiley & Sons, (2006).
31. Physical Property Measurement System: Resistivity Option User Manual, Second edition,(*Quantum Design, San Diego, 1999).*
32. Magnetic Property Measurement System: User Manual, Second edition,(*Quantum Design, San Diego, 1999).*

33. Déportes, C., *Sur la préparation anodique des ferrites, nickelites et cobaltites alcalins par électrolyse ignée et l'étude de leurs propriétés*. 131, 1 (1961).
34. Jansen, M. and R. Hoppe, *Neue Oxocobaltate.* Naturwissenschaften, **59**(5), 215-215, (1972).
35. Foo, M., et al., *Charge Ordering, Commensurability, and Metallicity in the Phase Diagram of the Layered Na_xCoO_2.* Physical Review Letters, **92**, 247001, (2004).
36. Zandbergen, H., et al., *Sodium ion ordering in Na_xCoO_2: Electron diffraction study.* Physical Review B, **70**, 024101,(2004).
37. Roger, M., et al., *Patterning of sodium ions and the control of electrons in sodium cobaltate.* Nature, **445,** 631-634, (2007).
38. Chen, X.Z, et al., *Preparation and transport properties of non-hydrated $Na_{0.5}CoO_2$ single crystals.* arXiv Cond-Mat/0412299, (2004).
39. Lin, C.T., et al., *Study of intercalation/deintercalation of Na_xCoO_2 single crystals.* Journal of Crystal Growth, **275**, 606-616, (2005).
40. Banobre-Lopez, M., et al., *Role of Doping and Dimensionality in the Superconductivity of Na_xCoO_2.* Chemistry of Materials, **17**(8), 1965-1968, (2005).
41. Park, S., et al., *Synthesis and high-pressure behavior of $Na_xCoO_2.3 H_2O$ and related phases.* Physical Review B, **68**(18), 180505, (2003).
42. Liu, C.-J., et al., *Preparation of Superconducting $Na_x(H_2O)_yCoO_2$ using $NaMnO_4$ as the Deintercalation and Oxidation Agent.* Journal of the American Chemical Society, **127**(3), 830-831, (2005).
43. Casolo, S., et al., *Theoretical analysis of oxygen vacancies in layered sodium cobaltate, $Na_xCoO_{2-\delta}$.* Journal of Physics: Condensed Matter, **24**(47), 475505, (2012).
44. McGreevy, R.L., *Reverse Monte Carlo modelling.* Journal of Physics: Condensed Matter, **13**(46), R877, (2001).

45. Keen, D. and R. McGreevy, *Structural modelling of glasses using reverse Monte Carlo simulation. Nature* **344**, 423 - 425, (1990).

46. Stewart, J. and R. Cywinski, *Magnetic short-range order in β-$Mn_{1-x}Co_x$.* Journal of Physics: Condensed Matter, **21**(12), 124216, (2009).

47. Krockenberger, Y., et al., *Superconductivity in epitaxial thin films of $Na_xCoO_2{\cdot}yD_2O$.* Applied Physics Letters, **88**(16), 162501-3, (2006).

48. Raveau, B. and M. Seikh, *Cobalt Oxides: From Crystal Chemistry to Physics*. Wiley publications (2012).

49. Venkatraman, S. and A. Manthiram, *Synthesis and characterization of P3-Type $CoO_{2-\delta}$.* Chemistry of Materials, **14**(9), 3907-3912, (2002).

50. Huang, Q., et al., *Low temperature phase transitions and crystal structure of $Na_{0.5}CoO_2$.* Journal of Physics: Condensed Matter, **16**, 5803-5814, (2004).

51. Alloul, H., et al., *Na ordering imprints a metallic kagomé lattice onto the Co planes of $Na_{2/3}CoO_2$.* EPL (Europhysics Letters), **85,** 47006, (2009).

52. Huang, F.-T., et al., *Sodium ion ordering of $Na_{0.77}CoO_2$ under competing multivacancy cluster, superlattice, and domain formation.* Physical Review B, **80,** 144113, (2009).

53. Hinuma, Y., Y. Meng, and G. Ceder, *Temperature-concentration phase diagram of P2-Na_xCoO_2 from first-principles calculations.* Physical Review B, **77,** 1-16, (2008).

54. Meng, Y.S., Y. Hinuma, and G. Ceder, *An investigation of the sodium patterning in Na_xCoO_2 ($0.5<x<1$) by density functional theory methods.* The Journal of chemical physics, **128,** 104708, (2008).

55. Feyerherm, R., et al., *Transition from a phase-segregated state to single-phase incommensurate sodium ordering in γ-Na, Physical Review B*, 82(2), 024103, (2010).

56. Lee, M., et al., *Large enhancement of the thermopower in Na_xCoO_2 at high Na doping.* Nature materials, **5**, 537-40 (2006).

57. Lee, M., et al., *Supplementary Information : Large enhancement of the thermopower in Na_xCoO_2 at high Na doping.* Nature materials, **5**, 537-40, (2006).

58. Kaurav, N., et al., *Seebeck coefficient of Na_xCoO_2: Measurements and a narrow-band model.* Physical Review B, **79**(7), 075105, (2009).

59. Foo, M.L., et al., *Charge-ordering, commensurability and metallicity in the phase diagram of layered $NaCoO_2$.* Physical Review Letters, **92**, 247001, (2004).

60. Helme, L., et al., *Spin gaps and magnetic structure of Na_xCoO_2.* Physical Review B, **73,** 054405, (2006).

61. Bayrakci, S., et al., *Bulk antiferromagnetism in $Na_{0.82}CoO_2$ single crystals.* Physical Review B, **69**, 2-5, (2004).

62. Bernhard, C., et al., *Charge Ordering and Magnetopolarons in $Na_{0.82}CoO_2$.* Physical Review Letters, **93**(16), 167003, (2004).

63. Mukhamedshin, I., et al., *Na^{23} NMR Evidence for Charge Order and Anomalous Magnetism in Na_xCoO_2.* Physical Review Letters, **93,** 167601, (2004).

64. Luo, J., et al., *Metamagnetic Transition in $Na_{0.85}CoO_2$ Single Crystals.* Physical Review Letters, **93**(18), 187203, (2004).

65. Bayrakci, S., et al., *Magnetic Ordering and Spin Waves in $Na_{0.82}CoO_2$.* Physical Review Letters, **94,** 20-23, (2005).

66. Wang, Y., *Spin entropy as the likely source of enhanced thermopower in Na_xCoO_2* . Nature **423**: p. 425-428, (2003).

67. Baskaran, G., *Electronic Model for CoO_2 Layer Based Systems: Chiral Resonating Valence Bond Metal and Superconductivity.* Physical Review Letters, **91**(9), 097003, (2003).

68. Mukhamedshin, I. R., et al. *^{59}Co NMR Study of the Co States in Superconducting and Anhydrous Cobaltates.* Physical review letters 94(24), 247602, (2005).

69. Valkeapää, M., et al., *Charge compensation and oxidation in $Na_xCoO_{2-\delta}$ and $Li_xCoO_{2-\delta}$ studied by XANES.* Journal of Solid State Chemistry, **180,** 1608-1615, (2007).

70. Yokoi, M., et al., *Magnetic Correlation of Na_xCoO_2 and Successive Phase Transitions of $Na_{0.5}CoO_2$ NMR and Neutron Diffraction Studies.* Journal of the Physics Society Japan, **74,** 3046-3056, (2005).

71. Joly, Y., *X-ray absorption near-edge structure calculations beyond the muffin-tin approximation.* Physical Review B, **63**(12), 125120, (2001).

72. Joly, Y., *FDMNES User's Guide.* Institut Néel, CNRS, 1-56, (2007).

73. Jahn, Hermann Arthur, and Edward Teller. *"Stability of polyatomic molecules in degenerate electronic states. I. Orbital degeneracy."* Proceedings of the Royal Society of London. Series A, Mathematical and Physical Sciences 161, 905, 220-235, (1937).

Appendix A

FDMNES Input File

```
! Fdmnes indata file

! Calculation for the Na0.5CoO2 Divacancy phase (50% Phase), without Co distortions

! For comparison with I16 Data

! 25 May 2012

 Filout

  Na5CoO2_EXP\Na50

 Range                    ! Energy range of calculation (eV). Energy of photoelectron relative to Fermi level.

 -19. 0.5 31.              ! 109 steps, same as Diamond

 Radius                   ! Radius of the cluster where final state calculation is performed

   4                     ! For a good calculation, this radius must be increased up to 6 or 7 Angstroems

 SCF                      ! Self Consistant solution

 Green                    ! Muffin tin potential - faster

 memory_save              ! Makes an approximation of the potential calculation to speed up the calculation

 Quadrupole               ! Allows quadrupolar E1E2 terms

 Zero_azim                ! Define basis vector for zero psi angle
```

```
 0.38678 0.25785 0.          ! Same as I16, Reciprocal hex (1 0 0) in units of real SL.

                    ! hkl([1 0 0]*RcSp(nacoo2),[2 0 0; 1 2 0; 0 0 1]*nacoo2)

 rxs                        ! Resonant x-ray scattering at various peaks, peak given by: h k
l sigma pi azimuth.

  0 2 7 1 1                 ! 1(0.5 0.5 7) sigma-sigma

  0 2 7 1 2                 ! 1(0.5 0.5 7) sigma-pi

  0 0 7 1 1                 ! 2(0 0 7) sigma-sigma

  0 0 7 1 2                 ! 2(0 0 7) sigma-pi

  0 1 7 1 1                 ! 5(0 0.5 7) sigma-sigma

  0 1 7 1 2                 ! 5(0 0.5 7) sigma-pi

  1 1 7 1 1                 ! 7(0.5 0.25 7) sigma-sigma

  1 1 7 1 2                 ! 7(0.5 0.25 7) sigma-pi

  1 0 7 1 1                 ! 10(0.25 0.25 7) sigma-sigma

  1 0 7 1 2                 ! 10(0.25 0.25 7) sigma-pi

  0 2 8 1 1                 ! 1(0.5 0.5 8) sigma-sigma

  0 2 8 1 2                 ! 1(0.5 0.5 8) sigma-pi

  0 0 8 1 1                 ! 2(0 0 8) sigma-sigma

  0 0 8 1 2                 ! 2(0 0 8) sigma-pi

  0 1 8 1 1                 ! 5(0 0.5 8) sigma-sigma

  0 1 8 1 2                 ! 5(0 0.5 8) sigma-pi

  1 1 8 1 1                 ! 7(0.5 0.25 8) sigma-sigma

  1 1 8 1 2                 ! 7(0.5 0.25 8) sigma-pi

  1 0 8 1 1                 ! 10(0.25 0.25 8) sigma-sigma

  1 0 8 1 2                 ! 10(0.25 0.25 8) sigma-pi

 Crystal                    ! Periodic material description (unit cell)
```

```
5.7 4.9363 10.8 90 90 90      ! a, b, c, (Angstrom) alpha, beta, gamma (degree)
27  0.0000 0.0000 0.0000      ! Atomic positions from basis2(6.4,'Na',2)
27  0.0000 0.0000 0.5000
27  0.2500 0.5000 0.0000
27  0.2500 0.5000 0.5000
27  0.5000 0.0000 0.0000
27  0.5000 0.0000 0.5000
27  0.7500 0.5000 0.0000
27  0.7500 0.5000 0.5000
 8  0.0000 0.3333 0.0908
 8  0.0000 0.3333 0.4092
 8  0.2500 0.1667 0.5908
 8  0.2500 0.1667 0.9092
 8  0.2500 0.8333 0.0908
 8  0.2500 0.8333 0.4092
 8  0.5000 0.6667 0.5908
 8  0.5000 0.6667 0.9092
 8  0.5000 0.3333 0.0908
 8  0.5000 0.3333 0.4092
 8  0.7500 0.1667 0.5908
 8  0.7500 0.1667 0.9092
 8  0.7500 0.8333 0.0908
 8  0.7500 0.8333 0.4092
 8  1.0000 0.6667 0.5908
 8  1.0000 0.6667 0.9092
```

Appendix A

11 0.5000 0.6666 0.2500

11 1.0000 0.3333 0.7500

11 0.0000 0.0000 0.2500

11 0.5000 0.0000 0.7500

Convolution

Scan

Na5CoO2_EXP\Na50_scan_1.txt

Na5CoO2_EXP\Na50_scan_2.txt

Na5CoO2_EXP\Na50_scan_3.txt

!Na5CoO2_EXP\Na50_scan_4.txt

Scan_conv

Na50_scan_conv.txt

End